THE UNIVERSITY *of* EDINBURGH

Enhanced Energy and Spectrum Efficiency in Visible Light Communications

TILAHUN ZERIHUN GUTEMA

A thesis submitted for the degree of Doctor of Philosophy

The University of Edinburgh

January 2023

To my mother,

Mulusew Yizengaw (*Emewa*)

1963 – 2017

Her love, support, and encouragement were always a source of strength for me.
I am forever grateful for the sacrifices she made and the endless love she showed me.
She believed in me, inspired me, saw the best in me, and pushed me to always do my best.
This achievement is as much hers as it is mine and I am honoured to dedicate it to her memory.

Lay Summary

Visible light communication (VLC) uses light-emitting diodes (LEDs) in the visible light spectrum to transmit data and has become increasingly popular for short-range wireless connections. The focus of this research is to create techniques that will increase the spectral and energy efficiency of VLC systems. This involves maximising the amount of data that can be transmitted within a given bandwidth and minimising the energy needed to transmit data, both of which are crucial for optimising performance and reducing costs in a VLC system.

One approach implemented in this thesis is to optimise the LED operating point at which the LED is driven to transmit data. This resulted in an increased modulation bandwidth and therefore the ability to transmit more data. This approach is then used in VLC with probabilistic shaping (PS). PS involves shaping the information bits into a distribution that is well-matched to the channel characteristics, such as a Gaussian distribution in the VLC channel. By shaping the information bits in this way, it is possible to increase the capacity of the channel and transmit more data efficiently. The thesis also introduces a new technique called frequency shift chirp modulation (FSCM). In FSCM, information is encoded using a continuous, sweep-like method across certain frequency ranges. This allows it to be robust in scenarios where there is limited bandwidth or channels that have varying responses at different frequencies. This has potential applications in areas where energy consumption is a major concern, such as the Internet of Things (IoT).

Abstract

In recent years, there has been a surge in data traffic, leading to the investigation of using optical frequencies in conjunction with radio frequency (RF) wireless communication systems. One such technology is visible light communication (VLC), which uses light-emitting diodes (LEDs) in the visible light spectrum to transmit data. VLC has gained popularity for short-range wireless connections due to its energy efficiency, low-cost, and wide availability of front-end devices. However, one of the main challenges in designing a VLC system is improving its energy and spectral efficiency. This thesis aims to investigate techniques and determine the most effective methods for enhancing the energy and spectral efficiency of VLC systems.

The thesis examined methods for optimising the bias point of an LED to benefit from increasing bandwidth at higher driving current while minimising the resulting signal distortion. The approaches are based on allowing for some nonlinear distortion or reducing signal swing/signal-to-noise ratio (SNR) while benefiting from higher bandwidth at higher driving currents. A framework is presented to estimate the attainable capacity under both conditions. Simulation results showed that the optimal bias point does not lie in the middle of the dynamic range. This was verified through a PAM-based VLC experiment, which showed that the transmission rate can be increased by choosing the optimal bias current instead of the midpoint of the linear range.

Subsequently, VLC with probabilistic shaping (PS) is studied to optimise the distribution of source symbols and improve system performance. In this study, the error performance of PS is analysed, and closed-form analytical expressions are provided. The results show that PS outperforms the conventional uniform distribution and significantly reduces the required SNR to achieve a certain error probability. To demonstrate the practical application of PS in VLC, it was implemented in conjunction with optical orthogonal frequency-division multiplexing (OFDM) modulation. This allowed for continuous and adaptive loading of information bits to the channel response, resulting in an efficient use of available modulation bandwidth and transmission rates close to the channel capacity limits. In the two experimental demonstrations, a single low-power LED and a wavelength-division multiplexing (WDM) system using three off-the-shelf LEDs were used to achieve bit rates of 1.13 Gbps and 10.81 Gbps, respectively, representing increases of 27.13% and 25.7% over the traditional bit-power loading technique.

Finally, an alternative approach towards enhancing the energy of VLC systems is introduced using frequency shift chirp modulation (FSCM). The error performance of FSCM was analysed in different types of channels, and a proof-of-concept experiment was conducted to demonstrate its potential use in VLC systems. FSCM offers improved robustness in band-limited, frequency-selective channels compared to other modulation techniques. This makes it a promising choice for integrating into VLC systems, particularly in low-power and low-rate application scenarios.

Declaration of Originality

I declare that this thesis has been composed solely by myself, that the work contained herein is my own except where explicitly stated otherwise by reference or acknowledgement, and that this work has not been submitted for any other degree or professional qualification except as specified.

Tilahun Zerihun Gutema
Edinburgh, The United Kingdom
June 08, 2023

Acknowledgements

This thesis was written during my postgraduate studies at the Institute for Digital Communications, School of Engineering, the University of Edinburgh. I would like to thank the University of Edinburgh for providing me with the resources and facilities necessary to conduct my research. This work was supported by the European Union's Horizon 2020 research and innovation programme under the Marie Skłodowska Curie grant agreement №. 814215 titled ENLIGHT'EM: European Training Network in Low-Energy Visible Light IoT Systems. I am grateful for this funding, as it has allowed me to pursue my PhD without financial burden.

I would like to express my heartfelt gratitude to my supervisor, Dr Wasiu Popoola. His support and encouragement throughout my PhD journey have been invaluable and unwavering. His guidance, expertise, and mentorship have helped shape my research and have been a constant source of inspiration.

I am grateful to all my colleagues, Callum Geldard, Hussien Alrakah, Ahmet Burak Özyurt, Egecan Guler, Jianhui Chen, Ryo Harada, Jian Shao, Minqing Yu, and Behnaz Majlesein for their valuable insights and assistance during this research. I have been fortunate to have their expertise and guidance, which have been helpful in my learning and development. I would also like to express my sincere gratitude to Iain Gold and his colleagues in the School of Engineering electrical support team who helped me design and manufacture various electronic circuits. Their assistance was invaluable in completing this project.

I am very grateful to my friends, Asemare Mengistie and Biniyam Yakob for providing such interesting discussions in both high and low times. I can always count on them for their wisdom and support, whether it's about research or just venting about life. I would like also to thank my friend, Samuel Admasie for proofreading this thesis. His constructive feedback was very helpful in improving this work.

I would also like to thank my girlfriend, Bemnet for her love and support which has meant everything to me. She has truly been an ever-present source of strength. Her understanding and encouragement have helped me through so much, and I am so grateful to have her by my side.

Finally, I am eternally thankful to God for giving me a supportive family: my father, Zerihun Gutema and my siblings and their family: Masresha, Martha, Birhanu, Gelanie, and Birtukan. Their love, support, and understanding have been a reliable source of encouragement as I work towards my aspirations. They have always believed in me and have encouraged me to pursue my passions. Their support has been a reliable motivation and has played a pivotal role in where I am today. Thank you for always standing behind me and supporting me.

Contents

List of Figures

List of Tables

List of Abbreviations

ACO-OFDM	asymmetrically clipped optical orthogonal frequency division multiplexing (OFDM)
ADC	analogue-to-digital converter
AFSK	asymmetric frequency shift keying
AIR	achievable information rate
APD	avalanche photodiode
APSK	asymmetric phase-shift keying
AWGN	additive white Gaussian noise
BER	bit error rate
BPSK	Binary phase shift-keying
CCDM	constant composition distribution matcher
CP	cyclic prefix
CSK	colour shift keying
CSS	chirp spread spectrum
DAC	digital-to-analogue converter
DC	direct current
DCO-OFDM	DC-biased optical OFDM
DD	direct detection
DFE	decision feedback equaliser
DMT	discrete multi-tone
DSP	digital signal processing
EMI	electromagnetic interference
ENOB	effective number of bits
EVM	error vector magnitude
FEC	forward error correction

FFT	fast Fourier transform
FPGA	field programmable gate arrays
FSCM	frequency shift chirp modulation
FSK	frequency shift keying
GMI	generalised mutual information
GPS	global positioning system
GS	Geometric shaping
HD-FEC	hard decision forward error correction
IEEE	Institute of Electrical and Electronics Engineers
IFFT	inverse fast Fourier transform
IM/DD	intensity modulation and direct detection
IM	intensity modulation
IoT	Internet of Things
IR	infrared
IrDA	Infrared Data Association
ISI	intersymbol interference
LASER	light amplification by stimulated emitted radiation
LED	light emitting diode
LLR	log-likelihood ratio
LoS	line-of-sight
LPF	low pass filter
MAP	maximum a-posteriori
MMSE	minimum mean square error
NGMI	normalised generalised mutual information
NLoS	non-line-of-sight
NRZ-OOK	non-return-to-zero on-off keying (OOK)
OFDM	orthogonal frequency division multiplexing
OOK	on-off keying

OWC	Optical wireless communication
PAM	pulse amplitude modulation
PAM-DMT	pulse amplitude modulated-discrete multitone modulation
PAPR	peak-to-average power ratio
PDF	probability density function
PIN	p-type intrinsic n-type
PMF	probability mass function
PPM	pulse position modulation
PS	probabilistic shaping
PSD	power spectral density
PSK	phase shift-keying
QAM	quadrature amplitude modulation
QPSK	quadrature phase shift keying
RF	radio frequency
RMS	root-mean-square
RRC	root-raised cosine
RZ-OOK	return-to-zero OOK
SD-FEC	soft-decision forward error correction
SER	symbol error rate
SNR	signal-to-noise ratio
TIA	transimpedance amplifier
U-OFDM	unipolar OFDM
UWOC	Underwater optical wireless communication
VLC	visible light communication
WDM	wavelength division multiplexing

List of Mathematical Symbols

α	offset bias current
γ	instantaneous SNR per symbol
$\overline{\gamma}$	average SNR per symbol
γ_{EM}	Euler–Mascheroni constant 0.57722
$\Delta\left(i_{\mathrm{bias}}\right)$	distortion factor in terms of bias current
ϵ	inverse average symbol energy
$\zeta\left(i_{\mathrm{bias}}\right)$	signal scaling factor
η	spectral efficiency in bit/s/Hz
κ	LED electrical-to-optical conversion factor
$\Lambda_{n,\,i}$	log-likelihood ratios
λ	PS rate parameter
μ	mean of log-normal fading irradiance
ν_k^2	power loading factor
ξ_{av}	average symbol energy
σ_I	mean and standard deviation of log-normal fading irradiance
σ_{n}^2	noise variance of additive white Gaussian noise
σ_{shot}^2	shot noise variance
$\sigma_{\mathrm{thermal}}^2$	thermal noise variance
τ_{c}	minority carriers lifetime
$\phi_{1/2}$	semi-angle at half power
Ψ_c	concentrator field-of-view (FoV)
ψ	angle of incidence of light with respect to the receiver axis
A	photodetector active detection area
$A_{\mathrm{eff}}\left(\psi\right)$	effective optical signal detecting area
B	transmission bandwidth
B_{max}	maximum bandwidth within the dynamic ranges
C	theoretical channel capacity limit (in bit/s)
c	chirp rate
D_m	decision region

d	receiver distance from transmitter
E_{b}	energy per bit
E_{b}/N_0	SNR per bit
E_{s}	average symbol energy
E_{s}/N_0	SNR per symbol
$\mathbb{E}[\cdot]$	statistical expectation
$\exp(\cdot)$ or $\mathrm{e}^{\cdot}$	exponential function
$f_{3\ \mathrm{dB}}$	−3 dB modulation bandwidth of an LED
$f(x)$	probability density function
G	shaping gain
$g_s(\psi)$	concentrator gain
$\mathcal{H}$	Hermitian symmetry
H	entropy
$H(f)$	channel frequency response
$h(t)$	channel impulse response
I	log-normal fading irradiance
$\mathbb{I}(X;Y)$	mutual information between X and Y
$I(\phi)$	radiant intensity of an LED at angle ϕ
i_{bias}	bias current of the LED
i_{max}	maximum allowable bias current of the LED
i_{mid}	mid-point bias current of the LED
$i_{\mathrm{max_B}}$	bias current at maximum bandwidth within the dynamic ranges
$i_{\mathrm{max_P}}$	bias current at maximum optical power within the dynamic ranges
$\mathrm{K_B}$	Boltzmann's constant, 1.380649×10^{-23} J/K
k	subcarrier index
$\ln(\cdot)$	natural logarithm
M	modulation order
m_B	bandwidth linear functions slope the dynamic ranges
m_O	optical power linear functions slope the dynamic ranges
$\mathrm{mod}(\cdot)$	modulo operator
N_{FFT}	the number of subcarriers (the order of FFT)
N_0	single-sided noise power spectral density (PSD)
$n(t)$	additive white Gaussian noise

P	probability distribution
P_{b}	bit error probability
P_b^{T}	target bit error probability
$P_{\max}$	maximum optical power within the dynamic ranges
P_{N}	noise power
P_{opt}	received average optical power at the photodetector
P_{s}	symbol error probability
$Q(\cdot)$	Gaussian Q-function
$Q^{-1}(\cdot)$	inverse Gaussian Q-function
q	elementary electron charge, $1.602176634 \times 10^{-19}$ C
R	photodetector responsivity in Ampere per Watt (A/W)
R_{b}	bit rate
R_{c}	code rate
R_{L}	Load resistance
$\mathrm{R}_{\mathrm{SYM}}$	lower bound to the mutual information
R_{s}	symbol rate
r_{th}	threshold points
s_i	constellation points
T	operating temperature in K
T_{s}	symbol duration
T_{sample}	sample duration
$T_s(\psi)$	transmission factor of the filter
$x[n]$	time domain digital signal
$x(t)$	electrical modulating signal
$y(t)$	output photodetector current

Chapter 1
Introduction

1.1 Background

The technological developments in wireless communication over the past few decades have greatly improved connectivity, allowing people and devices to easily access information. The technology has greatly improved since the introduction of the early generation wireless networks. This has led to the advancement of the 5G and upcoming beyond 5G and 6G networks, each of which is expected to offer enhanced performance and capacity to meet the growing demand for digital applications and services [2,3]. As the capacity of these networks improves, the network can be utilised by more people and devices, which in turn leads to a lot more data traffic at all levels of the network.

According to Cisco's Visual Networking Index, global internet usage was projected to increase at a rate of 26% per year between 2017 and 2022 and to reach a yearly rate of 4.8 zettabytes by 2022 [4]. This is supported by the November 2022 Ericsson mobility report [5], which shows that global mobile network data traffic is nearly doubling every two years. Specifically, it grew by 38% between the third quarter of 2021 and the third quarter of 2022 [5]. According to Ericsson's report, excluding traffic generated by fixed wireless access, total global mobile data traffic was projected to reach approximately 90 exabytes per month by the end of 2022. Furthermore, it is estimated to expand nearly fourfold, reaching 325 exabytes per month by 2028. However, when considering fixed wireless access, the report anticipated total mobile network traffic to reach approximately 115 exabytes per month by the end of 2022 and a staggering 453 exabytes per month by the end of 2028. In this era of high-definition video sharing and streaming, usage from popular social media platforms makes up the largest part of video traffic. Out of all global mobile network traffic in 2022, video constitutes around 70%, a share that is forecasted to increase to 80% in 2028. The continued growth in the number of Internet of Things (IoT) device models and chipsets with an ever-expanding set of supported features in extended reality (XR)-type services, including augmented reality (AR), virtual reality (VR), and mixed reality (MR) combined with machine-to-machine applications will continue to drive the scale and capacity of the network infrastructure.

As the demand for high-speed communication continues to grow, there is increasing pressure on the available spectrum to meet the needs of a wide range of applications and services. As more and more devices rely on wireless communication, the limited RF spectrum available is becoming congested, leading to slower data rates and reduced reliability. This has led to a scenario commonly known as a "spectrum crunch", as the demand for this resource outstrips the supply [6, 7]. Governments and regulatory bodies around the world are working to address this issue by allocating additional spectrum for use and finding ways to optimise the use of existing resources. This has spurred the search for alternative technologies that can provide the high data rates needed to meet the increasing demand.

One such technology that has gained attention in recent years is visible light communication (VLC) which uses the visible light spectrum to transmit data [8]. VLC has several advantages over traditional radio frequency (RF) communication technologies, including the availability of a large and unlicensed spectrum in the visible light domain, which is free from electromagnetic interference (EMI). In addition, VLC has inherent security, as the light waves used for communication cannot pass through solid objects and can only be received within line-of-sight. Advances in solid-state physics, such as the development of more efficient and compact light-emitting diodes (LEDs) and photodetectors, have also contributed to the feasibility of VLC as a communication technology. LEDs are widely used in modern lighting systems, making VLC a potentially cost-effective solution for communication in a variety of settings. This created an influx of research works which have proposed VLC as a plausible technology to supplement developments in RF-based networks.

One application of VLC that has garnered particular interest is LiFi, which is a high-speed bidirectional light-based networking solution that is proposed to work seamlessly with other RF access technologies [9, 10]. LiFi has the potential to provide high data rates in a variety of settings, including homes, offices, and public spaces. Advances in digital signal processing have also contributed to the feasibility of VLC as a communication technology. Modulation techniques, such as on-off keying (OOK), pulse-amplitude modulation (PAM), as well as optical orthogonal frequency-division multiplexing (OFDM) can be used to encode data onto the light signals used for communication, enabling high data rates to be achieved.

Despite the significant progress made in VLC and LiFi research, much of this work has focused on improving the data rate that can be achieved over a VLC network, without considering energy and spectral efficiency. In addition, these advancements are not specifically designed for

resource-constrained devices, such as IoT nodes with electrical and computing power limitations. On the contrary, there is a need for the development of energy-efficient signal processing techniques that can effectively transmit data while minimising energy consumption. However, there have been relatively few works that focus on the energy and spectral efficiency constraints of devices in VLC. Moreover, the energy consumption required to achieve high-speed VLC has not been thoroughly explored in the literature.

1.2 Research Motivation and Scope

One of the key challenges in designing and optimising a VLC system is to improve its energy and spectral efficiency. Energy efficiency is important as it can help to reduce the power consumption and operating costs of VLC systems, while spectral efficiency is crucial for supporting many users or applications in a given frequency band.

An important theoretical framework for understanding the relationship between signal-to-noise ratio (SNR), bandwidth, and the capacity of a communication channel is the ultimate capacity limit, which was formulated by Shannon in 1948 [11]. According to Shannon's theory, the capacity of a communication channel is directly proportional to the bandwidth of the channel and the logarithm of the SNR. The capacity is a linear function of the bandwidth, but a logarithmic function of the SNR. This means that increasing the bandwidth of a VLC system can significantly increase its capacity while increasing the SNR has a less pronounced effect. For instance, a $10\times$ increase in bandwidth will increase the capacity by $10\times$, but a $10\times$ increase in SNR will only increase the capacity by about $2\times$. As a result, it is important to optimise not only the SNR but also the bandwidth of a VLC system to maximise its capacity.

One approach to optimising the bandwidth of a VLC system is to investigate the interrelationship between the driving current of LEDs, the modulation bandwidth, the SNR, and the attainable capacity in VLC systems. This can help to optimise the performance of VLC systems by identifying the optimal operating conditions for different system parameters.

Another approach is to optimise the SNR term and maximise the available channel capacity for any given bandwidth that is available for use. This can be realised by adjusting the distribution of source symbols using signal shaping techniques. Conventional data transmission schemes transmit each symbol with equal probability, which is not optimal for the additive white Gaussian noise (AWGN) channel [12]. By using signal shaping techniques, it is possible

to optimise the distribution of source symbols and improve the spectral efficiency of a VLC system. This can help to close the gap between the spectral efficiency of a VLC system and Shannon's channel capacity.

An alternative approach towards enhancing the energy of VLC systems is to use orthogonal modulation schemes. These schemes have the potential to be energy-efficient and have applications in low-power and low-rate networks. However, orthogonal modulations may sacrifice spectral efficiency to approach Shannon's limit. As a result, it is important to carefully balance the trade-offs between energy efficiency and spectral efficiency when designing VLC systems using orthogonal modulations.

Hence, novel techniques are developed to optimise the spectral and energy efficiency of VLC systems. Figure 1.1 summarised the scope of this thesis showing the focus in each chapter. In Chapter 3, a framework identifying the optimal operating conditions for different system parameters is developed. This framework is then used in Chapter 4 to approach the ultimate capacity limit by optimising the distribution of source symbols using signal shaping techniques targeting a spectrally efficient system. In addition, the framework is combined with an energy-efficient orthogonal modulation scheme in Chapter 5 to approach the capacity limit targeting a sensitivity-constrained system. With these approaches, it is possible to improve the capacity and performance of VLC systems. Therefore, this thesis explores these techniques and identifies the most effective approaches towards enhancing the energy and spectral efficiency of VLC systems.

1.3 Research Objectives

The thesis aims to explore techniques and identify the most effective approaches towards enhancing the energy and spectral efficiency of VLC systems. Novel signal processing techniques to improve the energy and spectral efficiency of VLC systems will be developed and the effectiveness of these techniques will be assessed through a combination of theoretical analysis, simulations, and experimental demonstrations. The developed techniques will be compared to the state-of-the-art to determine the extent of their performance improvements. A variety of performance metrics, including achievable information rate (AIR), error performance measured by bit error rate (BER) and symbol error rate (SER), spectral and energy efficiency, will be used to evaluate the techniques. To accomplish these aims, the following specific objectives are set:

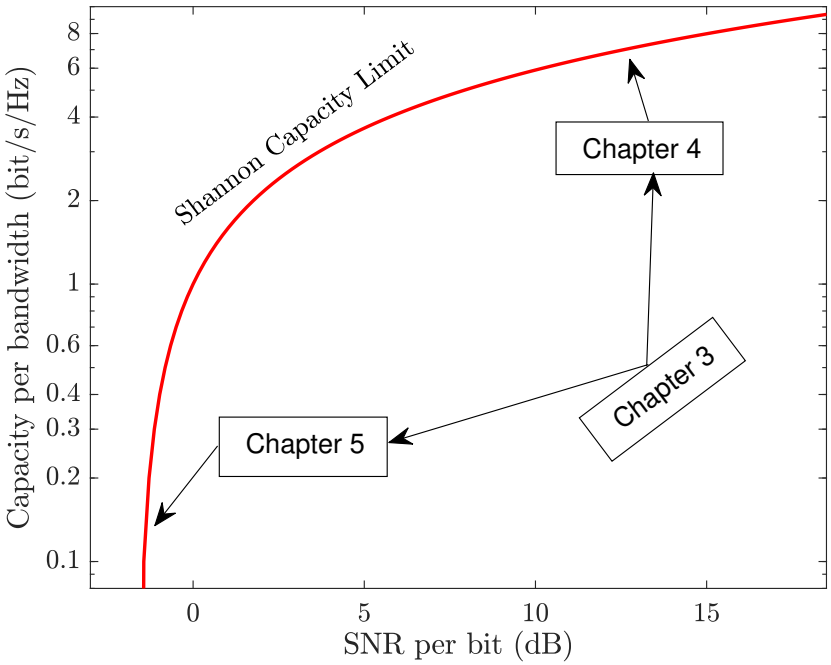

Figure 1.1: *Summary of the research scope*

- To thoroughly review the literature to understand the fundamental parameters of LED-based VLC that influence achievable information rate. These include studying the inter-relationship between driving current, the LED's modulation bandwidth, output optical power, channel amplitude and SNR responses.

- To investigate methods for optimising the DC bias of an LED to enhance the capacity by increasing the modulation bandwidth at higher driving currents while minimising signal distortion. This will involve developing and evaluating frameworks examining the impact of nonlinear distortion and SNR ratio.

- To investigate adaptive information bit and power loading as a means of utilising the channel frequency response of a VLC channel effectively and evaluate the challenges associated with it.

- To develop a signal processing technique to optimise the distribution of source symbols for a VLC channel using signal shaping and improve the spectral efficiency of a VLC system.

- To develop and evaluate performance of an alternative energy-efficient modulation technique for using VLC systems in low-power, low-rate networks, particularly in IoT.

- To implement the proposed techniques with minimum complexity as possible and validate them through a combination of theoretical analysis, simulations, and experimental demonstrations.

1.4 Thesis Contributions

This thesis has made original contributions by:

1. Developing an analytical framework to investigate the optimum direct current (DC) bias point in VLC systems. To achieve this, two different approaches were explored. The first method involved increasing the DC bias from the mid-point of the linear region, which allowed for modulation in the saturation region. The second method involved increasing the DC bias while keeping the modulating signal within the dynamic range. Through the analysis, the optimal DC bias point that provides maximum capacity by increasing the modulation bandwidth was determined. To validate these findings, a PAM-based VLC experiment was conducted, which confirmed the analytical results. This analytical framework and the experimental results contribute to the advancement of VLC technology, providing insights into the optimal DC bias point for improved system performance.

2. Analysing the error performance of probabilistically shaped quadrature amplitude modulation symbols under a Gaussian noise-limited condition and providing closed-form analytical expressions. The analysis is based on an optimum maximum a posteriori (MAP) detector derived for the probabilistic shaping scheme. This approach is then extended to transmission in optical channels with turbulence-induced fading, such as those encountered in underwater and free-space optical communication. In all channel conditions, PS improves the system performance compared to the conventional uniformly distributed symbols. The practicality of PS is validated through two proof-of-concept experiments demonstrating transmission rates close to channel capacity limits. The first experiment uses a single low-power LED to achieve a transmission rate of over 1 Gbps, a 27% improvement over the conventional method. The second experiment employs a wavelength division multiplexing (WDM)-based visible light communication (VLC) system with three off-the-shelf LEDs to achieve an aggregate transmission rate of nearly 11 Gbps, a 25% improvement over the conventional method. These contributions provide valuable insights into the potential of PS for improving the performance of VLC systems.

3. Introducing an alternative frequency shift chirp modulation (FSCM) technique that is energy-efficient and compatible with VLC systems. The theoretical framework of FSCM, including the modulation and demodulation processes and the error performance, is provided. A proof-of-concept experimental demonstration is also conducted. The FSCM technique is shown to be promising for improving energy efficiency in low-power and low-rate VLC applications.

1.5 List of Publications

The following publications have been contributed in journals and conference proceedings.

Journal Papers

[J1]. T. Z. Gutema, H. Haas and W. O. Popoola, "Bias Point Optimisation in LiFi for Capacity Enhancement," in Journal of Lightwave Technology, vol. 39, no. 15, pp. 5021-5027, Aug.1, 2021, doi: 10.1109/JLT.2021.3083510.

[J2]. T. Z. Gutema, H. Haas and W. O. Popoola, "WDM Based 10.8 Gbps Visible Light Communication With Probabilistic Shaping," in Journal of Lightwave Technology, vol. 40, no. 15, pp. 5062-5069, 1 Aug.1, 2022, doi: 10.1109/JLT.2022.3175575.

[J3]. T. Z. Gutema, H. Haas and W. O. Popoola, "On Symbol Error Performance of Probabilistic Shaping in Noise-Limited and Fading Channels," in IEEE Open Journal of the Communications Society, vol. 4, pp. 1218-1228, 2023, doi: 10.1109/OJCOMS.2023.3278972.

[J4]. H. T. Alrakah, T. Z. Gutema, S. Sinanovic and W. O. Popoola, "PAPR Reduction in DCO-OFDM Based WDM VLC," in Journal of Lightwave Technology, vol. 40, no. 19, pp. 6359-6365, 1 Oct.1, 2022, doi: 10.1109/JLT.2022.3196505.

Conference Papers

[C1]. T. Z. Gutema, H. Haas and W. O. Popoola, "OFDM based visible light communication with probabilistic shaping,", in Proceedings of the Workshop on Light Up the IoT (LIOT '20). Association for Computing Machinery, New York, NY, USA, 1–5, 2020, doi: 10.1145/3412449.3412548.

[C2]. T. Z. Gutema and W. O. Popoola, "Single LED Gbps Visible Light Communication with Probabilistic Shaping," 2021 IEEE Global Communications Conference (GLOBECOM), 2021, pp. 1-6, doi: 10.1109/GLOBECOM46510.2021.9685753.

[C3]. T. Z. Gutema and W. O. Popoola, "Energy Efficient Frequency Shift Chirp Modulation for Visible Light Communication," 2023 IEEE International Symposium on Personal, Indoor and Mobile Radio Communications (PIMRC), [under review].

[C4]. H. Alrakah, T. Z. Gutema, F. Offiong and W. Popoola, "PAPR Reduction in DCO-OFDM and PAM-DMT Based VLC Systems," 2022 Conference on Lasers and Electro-Optics (CLEO), 2022, pp. 1-2.

[C5]. H. T. Alrakah, T. Z. Gutema, S. Sinanovic and W. O. Popoola, "PAPR Reduction in PAM-DMT based WDM VLC," 2022 13th International Symposium on Communication Systems, Networks and Digital Signal Processing (CSNDSP), 2022, pp. 174-178, doi: 10.1109/CSNDSP54353.2022.9907952.

1.6 Thesis Outline

The thesis is organised into six chapters. The subsequent chapters are structured in the following way.

Chapter 2 provides a comprehensive overview of VLC technology, including its key features, benefits, and potential challenges. It also covers the various components of a VLC transmitter and receiver, as well as the optical channel link. The chapter discusses the different modulation techniques that are compatible with VLC and evaluates their performance in terms of energy and spectral efficiency. In addition, the chapter introduces an alternative probabilistic shaping technique, in which symbols are generated at varying probabilities. Finally, the chapter compares and discusses related literature on the topic of the thesis.

Chapter 3 presents a framework for studying the relationship between driving current and achievable information rates in VLC systems. Two different approaches for determining the optimal drive current (bias point) for intensity-modulated VLC systems are discussed. One approach allows for some nonlinear distortion, while the other aims to increase bandwidth at higher drive currents resulting in SNR reduction. The chapter also covers the characteristics of LEDs, including radiated optical power and modulation bandwidth, and how these are affected

by the drive current. Based on these discussions, the principles and methods of bias point optimisation are described, along with the VLC channel model assumptions and link capacity. Simulation results and experimental validation of one of the optimisation methods are also provided to illustrate these concepts.

Chapter 4 covers the concept of probabilistic shaping, including the generation of a Gaussian-like distribution and its implementation, is discussed. The chapter also formulates performance metrics for probabilistic shaping in terms of symbol-wise and bit-wise information rates. The error performance of probabilistic shaping-based uncoded QAM under Gaussian noise-limited conditions is analysed, and analytical expressions are provided. These results are compared with those for conventional uniformly distributed uncoded QAM symbols. In addition, probabilistic shaping is applied in conjunction with optical OFDM modulation as a proof-of-concept implementation, resulting in the efficient use of available modulation bandwidth and the demonstration of transmission rates close to channel capacity limits. Two experimental demonstrations are presented: one using a single low-power LED, and the other using a WDM-based visible light communication system with three off-the-shelf LEDs.

Chapter 5 examines the use of frequency shift chirp modulation in a VLC system for low-power and low-rate applications. The chapter introduces methods for generating and detecting FSCM signals and analyses the error performance of FSCM in noise-limited and frequency-selective channels with limited modulation bandwidth using Monte Carlo simulations. The chapter also presents a proof-of-concept experimental demonstration of an FSCM-based VLC system, along with a comparison of its performance to other conventional modulation schemes. This chapter differs from Chapter 4 in that it aims to enhance energy and targeting a sensitivity-constrained VLC system for IoT applications, rather than focusing on increasing the data rate.

Chapter 6 summarises the main findings of the research in this thesis, highlighting the key points that have been discovered. It also addresses the limitations of the study and identifies potential directions for further research. The purpose of this chapter is to give a comprehensive overview of the completed work and suggest areas that may be worthy of future exploration.

Chapter 2
An Overview of Visible Light Communication

2.1 Introduction

In the past few decades, there is an exponentially rising demand for wireless communication technology. To keep up with this need, different parts of the electromagnetic spectrum have been explored for use of communication. Optical wireless communication (OWC) is one of the prominent technologies that entails the transmission of information-carrying signal over optical radiation over the free-space channel. In OWC, the infrared (IR), ultraviolet, and visible light frequency ranges are commonly used. In VLC, information is transmitted by changing the intensity of the optical source according to a message signal. This is carried out at a rate faster than the human eye can detect the intensity variation.

Despite the recent increasing interest in VLC for short-reach wireless connectivity, light has been used as a communication means from ancient times by human beings. In ancient China, a smoke signal was used to communicate over long distances [13]. Meanwhile, torches were used to convey information in ancient Greece [14]. By the end of the eighteenth century, an optical telegraph in which information is encoded in the position of the paddles was used in France [15]. Using the optical telegraph, it was possible to send information much faster over long distances at a cheaper operating cost [15]. Perhaps the most prominent attempt towards wireless communication is the photophone by Alexander Graham Bell and his team. The photophone is the first wireless telephone which used sunlight and a vibrating mirror to transport voice signal. OWC gained attention in the 1970s when infrared communication was deployed for indoor applications [16]. Later, the formation of the Infrared Data Association (IrDA) promotes the research and development of IR-based short-range communications [17].

The use of light emitting diode (LED) for wireless indoor communication was first demonstrated in [18, 19]. These studies paved the way to further demonstration of LED-based VLC including the implementation of various optical digital modulation techniques and technologies

of LEDs. Global standards for short-range VLC were also provided by the Institute of Electrical and Electronics Engineers (IEEE) in 2011 at first [20], which is then revised in 2018 [21]. These standards cover the physical layer and medium access control layer design specifications.

Research works in recent years have proposed VLC as a plausible technology to supplement developments in the RF-based networks [22, 23]. That is mainly associated with the problem which is known as "spectrum crunch" in radio frequency (RF)-based communication. The continued rapid growth of data traffic is demanding high-capacity communication systems, which is causing spectrum shortage in the RF domain [24]. However, in the optical domain, a large and unlicensed spectrum, free from EMI, and with inherent security is available [23]. This has sparked tremendous interest in technologies involving VLC.

Moreover, the technological advances in solid-state physics enable to have energy-efficient LEDs which reduce energy consumption by more than 80% [25]. Besides, LEDs have a longer service lifetime than incandescent bulbs [26]. Due to that, LEDs are becoming market standards for illumination [26]. This is further shown by Haitz's law which is considered as the LED counterpart to Moore's law. Haitz's law states that "the cost per useful light emitted by an LED fall by a factor of 10, while the amount of light generated per LED package increase by a factor of 20, for a given wavelength" [27]. This is illustrated in Fig. 2.1 using data in [28]. This means that over time, LEDs have become more efficient at producing light and cheaper to

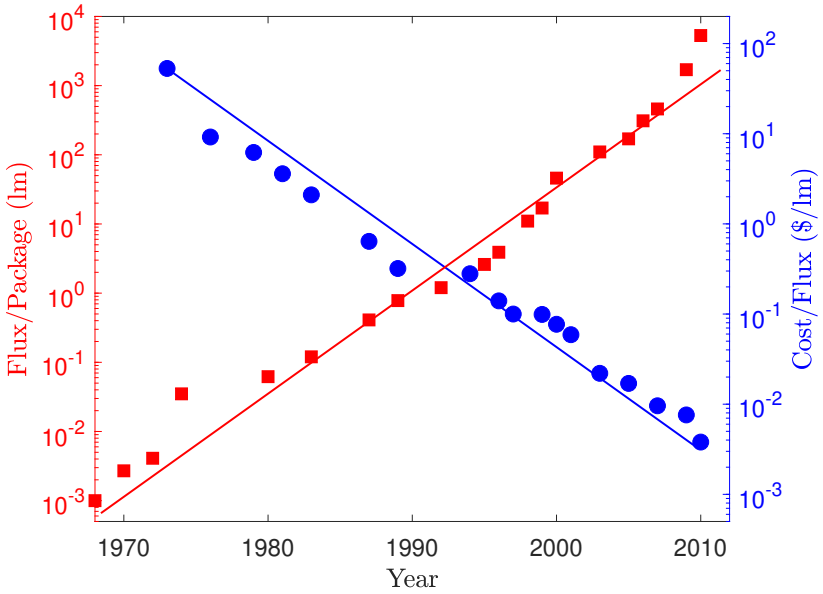

Figure 2.1: *Haitz's law illustrating the exponential increase of luminosity per package of LEDs over time, while the cost per lumen drops exponentially. The solid lines show these trend lines.*

use, making them an increasingly attractive option for lighting and other applications. Haitz's law has largely held true since it was first proposed in the late 1990s, with steady improvements in LED technology leading to significant increases in luminous efficacy and decreases in cost. This is important for VLC because it exploits this existing lighting infrastructure for communication. Moreover, LEDs can provide fast-switching capability which allows information to be encoded in radiating optical power without being perceived by the human eye [8, 23]. These exciting characteristics of LED enable VLC to draw increasing interest for indoor wireless communications [23].

In this chapter, an overview of VLC technology is presented starting with some basic features of VLC including its advantages, application areas and potential challenges in the technology. The chapter also describes system components in the transmitter, receiver as well as optical channel link. The modulation techniques which are compatible with VLC are also presented. The performance of these schemes is characterised in terms of energy and spectral efficiency. However, these conventional schemes use symbols generated with equal probability. An alternative probabilistic shaping technique in which symbols are generated at different probabilities is introduced in this chapter. The chapter also includes a comparative discussion of related literature to the theme of the thesis.

2.2 Features of VLC Systems

VLC has lots of advantages that make it suitable communication technology to be used in various application areas. There are also some limitations and challenges that need to be addressed to take the technology further. In the following, these benefits, possible application areas, and limitations of VLC are discussed.

2.2.1 Advantages of VLC

Some of the compelling benefits of VLC are listed below.

- *Large and unlicensed spectrum in the optical domain*:
  The amount of available spectrum in the visible light domain is vast covering from 400 THz to 800 THz (380 nm to 780 nm). Combined with the infrared spectrum, the visible light spectrum is about 2,600 times larger than a radio frequency covering from the

very low frequency (VLF) to extremely high frequency (EHF) (3 kHz to 300 GHz) [29], as shown in Fig. 2.2 [1, 30]. Most importantly, unlike the RF spectrum, the visible light spectrum is unregulated. This presents a wide range of academic and commercial possibilities for VLC [31].

- *Free from electromagnetic interference (EMI)*:
  VLC is naturally safe from any EMI including RF signals. This makes VLC suitable for communications in EMI-sensitive areas such as hospitals, military installations, aerospace applications, and petrochemical industries [32].

- *Inherent security and spatial reuse*:
  Optical radiations in VLC do not pass-through walls, rather communication is well-confined in a certain coverage area. Therefore, VLC is immune to potential snooping. This is an inherent property of light which also allows having co-existing of many links in closed areas interference-free. For example, a single room can be divided spatially for many transmission links to increase the data density [33, 34].

- *Easy implementation and low cost*:
  The signal processing techniques sought in VLC are simple to implement compared to coherent signal reception techniques in RF-based communication [35]. Furthermore, the front-end devices in VLC are widely available at low-cost. The energy consumption of LEDs is low compared to the other lighting technologies, which makes them part of the green technology [36]. Consequently, LEDs are being continuously integrated for lighting purposes. VLC can leverage this existing infrastructure for communication [9, 35]. However, when LEDs are used for communication purposes, signal processing techniques used for communication, such as modulation and DC bias optimisation, can have an impact on the amount of optical light required for lighting infrastructures. Thus, when LEDs are utilised for both lighting and communication, the requirements of both scenarios need to be taken into account during the development of the system to ensure sufficient illumination and reliable communication.

2.2.2 Application Areas of VLC

The advantages listed above make VLC an attractive communication technology to be used in a wide range of applications, from high-speed indoor internet access to vehicular communication.

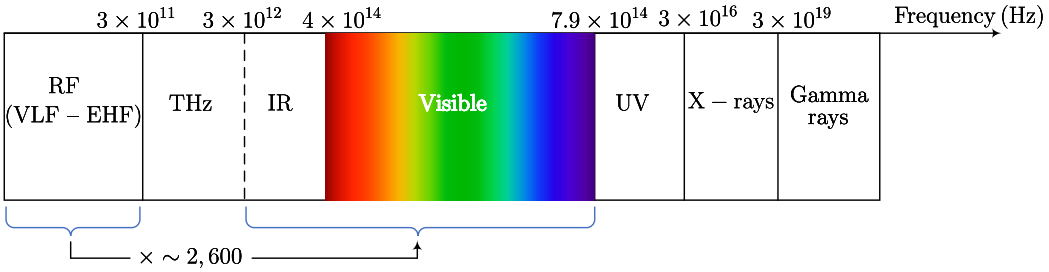

Figure 2.2: *The electromagnetic spectrum, comparing the bandwidth of visible light domain with RF spectrum (Picture adapted from [1]). Visible light and infrared spectrum are 2,600 times larger than the radio frequency spectrum (VLF to EHF).*

An overview of some of the application areas of VLC is outlined as follows.

- *Indoor wireless communication*:

  VLC can be used to provide internet access to homes and offices which are nowadays equipped with LED-based lighting fixtures. The light fixtures, besides illumination purposes, can be designed to provide internet as an access point to users in the room [23,37]. A fully connected wireless communication system of VLC forms LiFi which empowers high data rate and bidirectional multiuser communication [1]. There are numerous research activities in these regards demonstrating VLC in indoor environments and data rates have increased from a few megabits per second (Mbps) to gigabit per second (Gbps) transmission rates [38–42].

- *Underwater communication*:

  Acoustic communication is the most common underwater communication technology. However, the acoustic medium has a relatively low propagation speed, and therefore limited bandwidth and high energy consumption. Underwater optical wireless communication (UWOC), however, can provide high-speed transmission with low latency for short-reach underwater links [43]. The recent notable achievements demonstrating high-speed transmission include [44–48]. For long-reach underwater links, UWOC and acoustic communication can form a hybrid network to complement each other [49].

- *Indoor localisation*:

  In various indoor sectors, LEDs are being adopted and it is more likely to be omnipresent. In such environments, the unique identification of LEDs can provide flexible, accurate, and ubiquitous indoor navigation in areas where the global positioning system (GPS)

cannot be present [50]. VLC-based indoor positioning system has been demonstrated to deliver high accuracy and high resolution localisation [51–53].

- *Vehicular communication*:
  Vehicle lights can be used to establish vehicle-to-vehicle (V2V) communication. The V2V communication system enables transmitting of signal between two or more vehicles and sharing of vital information such as vehicle speed for platooning [54]. Communication can also be established between vehicles and traffic lights and/or signs creating infrastructure-to-vehicle (I2V) communication [55]. This has the potential to have an intelligent transportation system [56].

Other applications of VLC include in-flight connectivity where the LED lights inside the cabin can be used as VLC transmitter and illumination service [57]. Another application area is an integration of VLC with the power line in which the existing power line infrastructure is used to provide connectivity while exploiting energy-efficient LED illumination for wireless downlink [58].

2.2.3 Challenges

Despite the above compelling benefits and application of VLC, there are several basic system and network-level issues that need to be identified and addressed in the research and development of VLC. Some of these challenges are highlighted below.

- *Limited modulation bandwidth of LEDs*:
  Commercially available off-the-shelf LEDs are mainly manufactured for lighting purposes. Therefore, the modulation bandwidth of these LEDs is usually limited to only a few MHz [8, 59]. A typical blue LED has a -3 dB bandwidth of around 20 MHz [60], and if phosphor coating is applied to convert the blue light into white, the bandwidth is further reduced to 2 MHz [61]. There are some efforts to enhance the modulation bandwidth. Blue filtering is one of the common methods in which the slow phosphor spectral component is suppressed [62]. Using this method the modulation bandwidth of an LED can be improved up to ~ 20 MHz. Still, the overall frequency response of a VLC system is frequency-selective due to the limited modulation bandwidth of LEDs and front-end devices [63, 64]. This limits the data rate that can be achieved in VLC. For high-speed VLC, therefore, it is incumbent to operate beyond the -3 dB modulation bandwidth of

LEDs. This can be achieved by implementing appropriate signal processing techniques at the transmitter and/or the receiver such as pre-coding and equalisation [65, 66].

- *Nonlinear response of LEDs*:
  An LED has a nonlinear optical power response to the input electrical power. That is because the optical power increase linearly with the input current and saturates [67]. Modulation of LEDs in the nonlinear region leads to distortion [68, 69]. Consequently, it is common practice to use only the linear response region of the LEDs by applying proper direct current (DC) bias and signal swing. However, this will fundamentally limit the dynamic range. In order to minimise any nonlinear distortion associated with operating beyond the dynamic range of the LED, the bias point can be optimised. Alternatively, digital signal conditioning can be implemented on the transmitter and/or receiver side. A signal processing in a transmitter includes pre-distortion to linearise the dynamic range, apply clipping or scaling to limit the modulating signal in the linear region, while an equaliser can be employed to compensate for distortion at the receiver [70–72].

- *Modulation signal requirement*:
  VLC is based on modulating the intensity of the optical light source – intensity modulation (IM). The instantaneous output of modulated signal is real-valued. Moreover, an LED requires a non-negative modulating signal to radiate optical power as LEDs work in a forward bias. This means that the modulation techniques for VLC need to satisfy these requirements [35, 69]. This incurs additional restrictions not to use established digital modulation techniques from other communication technologies. Despite that, there are several efficient digital modulation techniques which satisfy the IM conditions.

- *Transmission link distance*:
  The link distance that can be achieved in VLC is relatively short due to the sharp decrease in the optical power of LEDs with distance. Using optical devices such as aspherical condenser lenses in the transmitter and receiver, a line-of-sight (LoS) and directional optical transmission can be established. However, this impacts the distribution of illumination and reduces coverage of non-line-of-sight (NLoS) communication. Also, it should be noted that the amount of radiation optical power is subjected to regulation. Other light sources, from lighting fixtures such as fluorescent, and incandescent, could introduce background noise and interference to the communication link. This could potentially have an impact on the signal quality at the receiver.

In addition to the above challenges in VLC, one needs to address network issues such as full-duplex communication, mobility and shadowing. A communication system should be built based on uplink and downlink capabilities. There are research works towards this. For example, LiFi is designed to provide this feature by realising fully networked wireless system [9]. Despite the confined nature of light is important to provide a secure and spatially dense network, it is also a challenge for mobility. That is because to provide reliable uninterrupted connectivity, a user device in a VLC network must be able to detect signals from a transmitter within the network coverage area [73].

2.3 System Components in VLC

In the following, the basic elements of VLC system are presented. Figure 2.3 shows the schematic of a typical VLC system. As any communication system, it consists of three main parts: transmitter, receiver, and channel. Each of these parts will be discussed below.

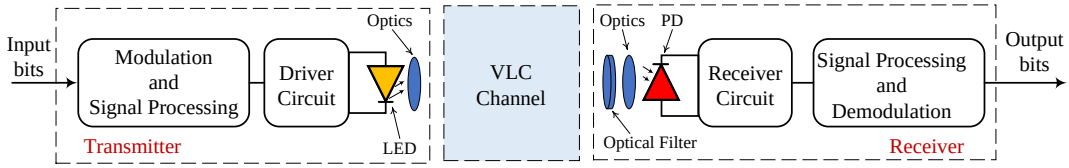

Figure 2.3: *System components of a typical VLC link, showing the transmitter, channel and receiver blocks*

2.3.1 Optical Transmitters

The transmitter comprises electrical and optical components that modulate the output signal of an optical source via IM. The digital information bits are usually mapped into digital symbol representations which are then mapped into a sequence of samples by employing an appropriate modulation technique. This is carried out in the digital domain and hence requires digital signal processing (DSP). Then a digital-to-analogue converter (DAC) transforms the digital signals into an equivalent analogue modulating signal.

A driver circuit is one of the important elements of an optical transmitter. It controls the amount of current flowing into the optical source in proportion to the modulating signal. The driver cir-

cuit is commonly used to convert the modulating signal into a unipolar signal, often by adding a DC bias. This is because the optical sources (such as LEDs) operate in forward-bias only. Having a negative amplitude leads to signal distortion. Therefore, DC bias is an offset to the modulation signal which makes sure that the signal has non-negative amplitudes. Moreover, the amount of optical power radiated from an optical source is proportional to the driving current. Also, the optical source modulation bandwidth increase as bias current increases [74, 75]. However, emitted optical power as a function of the driving current is not completely linear as it saturates at a higher bias current. Therefore, it is essential to determine the optimum bias point that provides maximum optical power and modulation bandwidth while minimising the nonlinear distortion that may arise from an increase in bias current. This will be the focus of Chapter 3 which presents bias point optimisation for capacity enhancement.

The optical source is used to convert the information-carrying electrical signal into optical intensity. The most commonly used light sources are LEDs and laser diodes. The choice of the source depends on the application area. LEDs are incoherent light sources as photons are emitted in the spontaneous emission process. The radiation pattern of LEDs is modelled by using a generalised Lambertian radiant intensity. It is mainly characterised by the semi-angle at half power, $\Phi_{1/2}$ which represents the field-of-view (FoV) of an LED. The LED's $\Phi_{1/2}$ is related to the Lambertian order, m by, $m = -\ln(2)/\ln\left(\cos\left(\Phi_{1/2}\right)\right)$ [35]. Generally, the radiant intensity of an LED at angle ϕ is given by [35]:

$$I_{\mathrm{LED}}(\phi) = \frac{m+1}{2\pi}\cos^{m}(\phi). \tag{2.1}$$

Most commercially available LEDs have a semi-angle at half power, $\Phi_{1/2} = 60^{\circ}$ which corresponds to Lambertian order $m = 1$. Generally, LEDs have wider radiation patterns compared to laser diodes, and thus are favourites for indoor and short-range VLC applications. The output radiation can be focused by using optics such as aspherical condenser lenses. These will collimate the light beam onto the receiver[1].

On the contrary, laser diodes are coherent optical sources as optical power output is generated by stimulated emission of photon radiation. Hence, the acronym light amplification by

[1]The collimation of the light reduces the FoV of the LED and influences the illumination intensity/coverage. However, in this thesis, the focus is on the communication side not on the illumination. Therefore, the illumination intensity/coverage loss due to collimation is not discussed here. However, the illumination requirements are defined by the considered application. As per the communication, the option is to collimate the LED lights to focus on the receiver (*i.e.* photodetector).

stimulated emitted radiation (LASER) [8]. Laser diodes are mostly used for long-range communication due to their high-power and directional optical radiation beam profile. They are also commonly used in underwater optical wireless communication [49, 76]. This is due to the relatively superior modulation bandwidth and the optical power that can be obtained from laser diodes compared to LEDs. However, the amount of optical power is still subjected to eye safety regulations [8].

2.3.2 Optical Receivers

The optical receiver of a VLC system detects an incident optical light and converts into electrical data to recover the transmitted information bit. Its main component is a photodetector that converts the received photons to electrons through the photoelectric effect [77]. The amount of electrical current is proportional to the impinging instantaneous optical power [35]. Hence, a direct detection (DD) of received optical signal. Combined with the IM at the transmitter, an intensity modulation and direct detection (IM/DD) system provides simple and low-cost transceiver implementation without the need for complex transceiver designs as in coherent systems. However, in IM/DD system only amplitude/intensity of signal is modulated losing the optical carrier's frequency and phase information [8].

Photodetectors have a very small detection active area. For example, the detection area of a commercially available PDA10A is $0.8\ \mathrm{mm}^2$ [78]. Therefore, to focus the incoming optical light onto the active areas of the photodetector, optical systems such as an aspheric condenser or concentrator lenses are commonly used. Furthermore, an optical filter can be applied before the photodetector to detect only the wavelength of interest. The optical filter can also reduce the unwanted noise from ambient light.

The most widely used photodetector types for VLC systems are the p-type intrinsic n-type (PIN) photodetector or avalanche photodiode (APD) [8]. The PIN photodetector has no internal gain and therefore has a smaller gain compared to APD photodetectors. However, PIN photodetectors are cheaper and offer a larger active detection area which makes it easier for implementation. These features make PIN photodetectors the favourite for indoor VLC applications. While APD photodetectors have higher sensitivity, they are susceptible to noise amplification due to the internal amplification process [8].

The sensitivity of a photodetector, which quantifies the amount of current the photodetector

can produce for a given instantaneous optical power in A/W, is usually small. This is usually below 1 A/W for PIN photodetectors, while it is higher than unity for APD photodetectors. The combination of a photodetector with a transimpedance amplifier (TIA) yields a better overall gain. Besides, the TIA converts the detected photocurrent into a voltage signal. Finally, an analogue-to-digital converter (ADC) is used to transform the signal from the analogue into a digital representation. In the digital form, the DSP unit carries out the demodulation process to recover the transmitted digital information bits.

The two primary sources of noise at the optical receiver are due to photon fluctuation (known as shot noise) and the resistive nature of receiver electronics (known as thermal noise) [8]. For a constant optical power impinging on a photodetector, the number of incoming photons per time fluctuates and the mean follows the Poisson distribution. This random nature of photons leads to shot noise (also known as Quantum noise). For a large number of photons detected at a photodetector, the shot noise can be modelled by a Gaussian distribution [8]. The variance of the shot noise can be estimated by [8]:

$$\sigma_{\text{shot}}^2 = 2qRP_{\text{opt}}B, \tag{2.2}$$

where the electron charge is denoted by q, and P_{opt} is the received average optical power at the photodetector. The transmission bandwidth is denoted by B. The thermal noise, meanwhile, is random electrical noise that is caused by the random motion of charge carriers in a conductor. It is present in all electrical circuits, and its impact increases with temperature. It has a constant power spectral independent of frequency and therefore can be considered white noise. Besides, the thermal noise follows a Gaussian distribution, and its noise variance is given as [8]:

$$\sigma_{\text{thermal}}^2 = \frac{4\text{K}_\text{B}TB}{R_\text{L}}, \tag{2.3}$$

where K_B is the Boltzmann's constant, T is the operating temperature in Kelvin. The load resistance is denoted by R_L. Other sources of noise in an optical receiver include the noise from the dark current which exists without any input optical power and noise from background radiation including ambient light and the Sun [8]. All in all, PIN-based receivers are usually regarded as thermal noise limited while APD-based receivers are shot noise limited [79].

2.3.3 VLC Channel Model

A VLC channel can be modelled as a baseband linear time-invariant system with impulse response, $h(t)$ [35]. Alternatively, the channel can be described by a frequency response, $H(f)$ as:

$$H(f) = \int_{-\infty}^{\infty} h(t)\, \mathrm{e}^{-\mathrm{j}2\pi f t} \mathrm{d}t, \tag{2.4}$$

which is the Fourier transform of $h(t)$. Figure 2.4 shows such a VLC channel model. In this

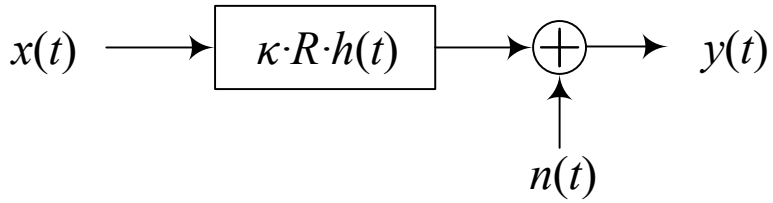

Figure 2.4: *Channel model with modulating signal $x(t)$, output photodetector current $y(t)$, additive noise $n(t)$, and an impulse response $h(t)$. R represents the responsivity of the photodetector while κ is LED's electrical-to-optical conversion factor.*

model, $x(t)$ denotes the input modulating electrical signal and the output photodetector current is represented by $y(t)$. Consequently, the equivalent received signal can be summarised by:

$$y(t) = \kappa R\left(h(t) \circledast x(t)\right) + n(t), \tag{2.5}$$

where " $\circledast$ " denotes the convolution operation, κ is the electrical-to-optical conversion factor of LED in W/A, and R is the responsivity of the photodetector. The noise is mainly due to shot noise and thermal noise, which is represented by $n(t)$. Both shot noise and thermal noise can be considered as white and Gaussian [8], and independent of transmitted optical power. Hence, it is acceptable to model $n(t)$ as additive white Gaussian noise (AWGN) with total noise variance written as:

$$\sigma_{\mathrm{n}}^2 = \sigma_{\mathrm{shot}}^2 + \sigma_{\mathrm{thermal}}^2, \tag{2.6}$$

where σ_{shot}^2 is shot noise variance given by (2.2) while $\sigma_{\mathrm{thermal}}^2$ is thermal noise variance given by (2.3).

For indoor VLC, the LoS link is dominant and the channel can be well-characterised by the

channel DC gain, $H(0) = \int_{-\infty}^{\infty} h(t)\,\mathrm{d}t$ [80, 81]. For an LoS channel model, as shown in Fig. 2.5, the channel DC gain can be estimated by considering only the direct propagation path. Suppose the LED emits a radiation pattern described by the radiation intensity $I_{\mathrm{LED}}(\phi)$ given by (2.1). The receiver located at distance d and angle ϕ with respect to the

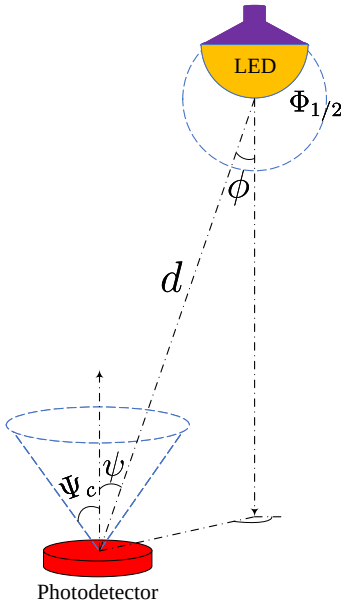

Figure 2.5: *Geometrical representation of a LoS VLC channel model*

transmitter detects irradiance of $I_{\mathrm{PD}}(\phi, d) = I_{\mathrm{LED}}(\phi)/d^2$. Thus, the received optical power is $P_{\mathrm{opt}} = I_{\mathrm{PD}}(\phi, d)\, A_{\mathrm{eff}}(\psi)$. Here, $A_{\mathrm{eff}}(\psi)$ denotes the effective optical signal detecting area given by [35]:

$$A_{\mathrm{eff}}(\psi) = \begin{cases} AT_s(\psi)\, g(\psi) \cos(\psi), & 0 \le \psi \le \Psi_c \\ 0, & \theta > \Psi_c \end{cases} \tag{2.7}$$

where A is the photodetector active detection area, ψ is the angle of incidence of light with respect to the receiver axis, $T_s(\psi)$ is the transmission factor of the filter, $g_s(\psi)$ is the concentrator gain, and Ψ_c is the concentrator FoV which is usually $\Psi_c \le \pi/2$. Therefore, using (2.1) and (2.7), the channel DC gain is obtained as:

$$H(0) = \begin{cases} \frac{(m+1)A}{2\pi d^2} \cos^m(\phi)\, T_s(\psi)\, g(\psi) \cos(\psi), & 0 \le \psi \le \Psi_c \\ 0, & \theta > \Psi_c. \end{cases} \tag{2.8}$$

It can be seen that the channel DC gain is proportional to d^{-2}. Besides, for a constant d and $I_{\mathrm{LED}}(\phi)$, the effective way to increase $H(0)$ is to increase the active area of the photodetector and/or increase the concentrator gain.

2.4 Modulation Techniques for VLC

One of the key challenges in VLC is the efficient encoding and transmission of information via visible light and the accurate extraction and decoding of the received signal by the receiver. This is where modulation and demodulation techniques come in. IM/DD is a type of modulation technique used in VLC systems. It is a simple and efficient way of encoding information onto a light wave by modulating the intensity of the light. That is, the information to be transmitted is represented by the variations in the intensity of the light wave. By rapidly switching between various intensity levels, the information can be transmitted to a receiver. The photodetector directly detects the intensity of the light and converts it into an electrical signal. This signal is then processed to extract the encoded information and decode it.

There are several modulation techniques that are commonly used in VLC, each with its own advantages and disadvantages. Some of the most common modulation techniques categorised as pulse modulation and optical OFDM are presented in this subsection.

2.4.1 Pulse Modulation Techniques

Pulse modulation techniques use discrete levels of signal amplitude to represent information bits/symbols. These modulation techniques are widely used in IM/DD systems. Some examples of pulse modulation techniques include OOK, pulse amplitude modulation (PAM), and pulse position modulation (PPM).

OOK is the classical and simplest modulation technique used for IM/DD in optical communication [8]. In OOK, a binary "1" is typically represented by a high-intensity light, while a binary "0" is represented by a low-intensity light. According to the standard outlined in IEEE 802.15.7-2018 [21], the reduction of radiant power due to modulation can be minimised by refining the intensity levels of both bit "1" and "0". Therefore, OOK is a binary modulation scheme which provides limited bandwidth efficiency. Depending on the duration of the intensity varies during a symbol duration, OOK can be designed to be in non-return-to-

zero OOK (NRZ-OOK) or return-to-zero OOK (RZ-OOK). In NRZ-OOK, the optical pulse is transmitted for the entire symbol duration, while in RZ-OOK pulse is transmitted to a certain duration of the symbol interval. RZ-OOK offers power efficiency over NRZ-OOK but comes at the cost of increased bandwidth requirements. Figure 2.6 illustrated a NRZ-OOK and 50% RZ-OOK signal with two levels of optical power outputs.

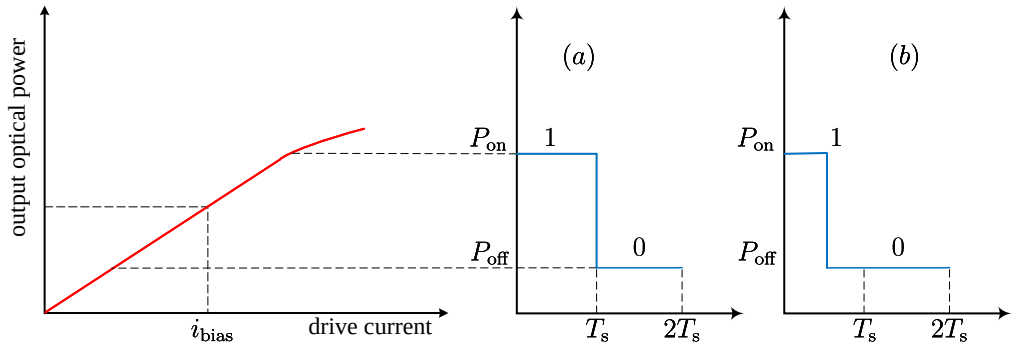

Figure 2.6: *OOK signalling showing NRZ-OOK optical output (a) and 50% duty cycle RZ-OOK (b)*

Improved bandwidth efficiency can be obtained by transmitting multiple intensity levels in a symbol duration using a M-ary PAM (M-PAM) scheme, where M denotes the modulation order which is also the number of optical power levels [82]. Therefore, unlike OOK which transmits 1 bit, in M-PAM, $\log_2 M$ bits are transmitted in a single symbol duration. For bipolar PAM, the signal amplitudes take discrete levels of $A_m = (2m - 1 - M)\, d$, where $m = 1, 2, \cdots, M$ and d is the Euclidean distance in which $2d$ is the distance between adjacent signal amplitudes. This kind of signal representation requires a suitable DC bias to ensure that all the pulses are positive. Figure 2.7 shows a 4-PAM optical signalling representation (after an appropriate DC bias is applied) which transmits 2 bit/symbol. A higher bit per symbol can be achieved using higher modulation order, hence improving bandwidth efficiency. However, the performance is affected by nonlinearity from LED as a larger dynamic range is required as M increases [83]. Moreover, the required signal-to-noise ratio (SNR) increases. In terms of system performance, M-PAM signalling is susceptible to intersymbol interference and requires complex equalisers at the receiver to mitigate [84].

A power efficient approach to circumvent limitations of PAM is to transmit a constant power over only a fraction of symbol duration [8]. PPM is an orthogonal modulation technique in

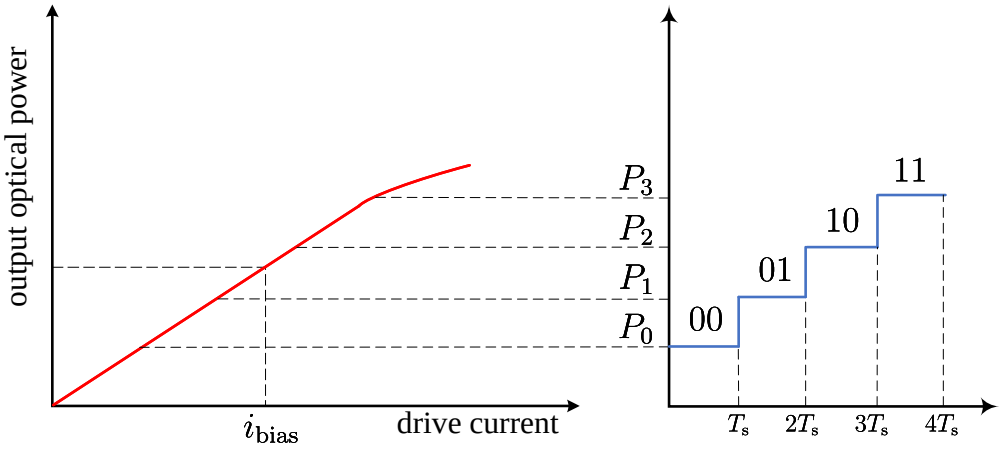

Figure 2.7: *4-PAM signalling showing the output optical power for the four amplitude levels*

which $\log_2 M$ information bit is transmitted by position of an optical pulse divided in M equidistance time slots of a symbol duration T_s, *i.e.* $T_c = T_s/M$. Figure 2.8 shows 4-PPM where different pulse positions are encoded inside a frame of a symbol duration. PPM waveform have low duty cycle $1/M$, only transmitting during T_c. This makes PPM suitable for power limited systems. Also, the power efficiency of PPM improves as M increases. However, at the expense of an increased bandwidth requirement and greater complexity [8]. Besides, PPM suffers a peak-to-average optical power ratio and is sensitive to receiver synchronisation which requires complex equalisation [85–87].

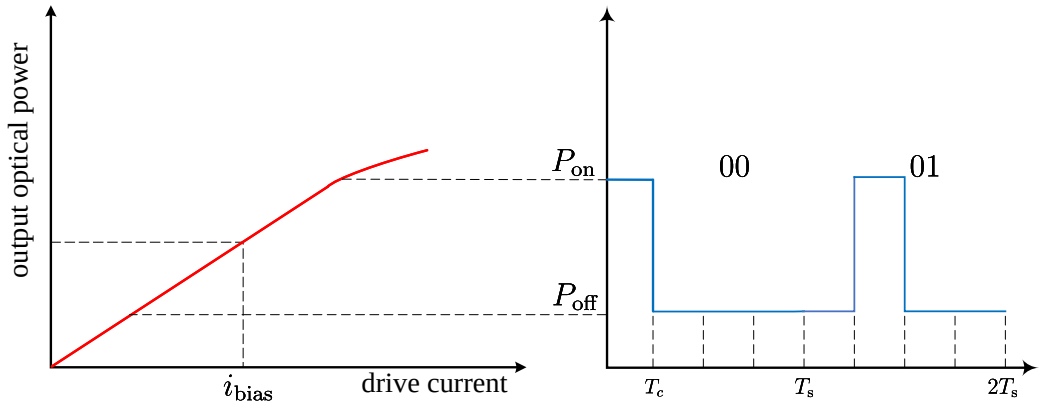

Figure 2.8: *4-PPM signalling showing the output optical power for the first two amplitude levels*

2.4.2 Optical OFDM

The required modulation bandwidth of pulse modulation schemes increases as the transmission rate increases. However, the modulation bandwidth of commercially available LEDs is limited to only a few MHz [8, 59]. Consequently, at a high data rate, pulse modulation schemes suffer from intersymbol interference (ISI). Moreover, the LED frequency response is usually modelled as a low-pass filter [63], which makes a VLC system frequency-selective [64]. It is incumbent to utilise all the available bandwidth including beyond the −3 dB modulation bandwidth of LEDs to realise a high-speed VLC system. Therefore, modulation techniques with higher spectral efficiencies are needed. In that regard, OFDM is a convenient modulation scheme. OFDM offers efficient use of the available spectrum and it is robust against channel frequency selectivity [84]. It also allows for low-complexity single-tap equalisers implementation in the frequency domain.

In optical OFDM, the available bandwidth is divided into multiple narrowband sub-channels, carrying a portion of the transmitted data. Each subchannel is called a subcarrier. The subcarriers are spaced apart at regular intervals and are orthogonal to each other. This allows the subcarriers to be transmitted simultaneously without interfering with each other. In each of the subcarriers information symbols generated by a conventional modulation scheme, usually M-ary QAM (M-QAM), is utilised. Figure 2.9 shows the system block diagram of an optical OFDM including the signal generation, transmission and detection. In the transmitter, information input bits are mapped into M-QAM constellations. Then the serial-to-parallel (S/P) block converts M-QAM symbol streams into parallel blocks of symbols which are then assigned to individual subcarriers. An inverse fast Fourier transform (IFFT) operation is applied to generate a time domain OFDM signal. However, to satisfy the IM/DD system requirement the modulating signal needs to be unipolar and real-valued.

A real-valued time domain signal is obtained by imposing Hermitian symmetry to parallel QAM symbols. This is realised by mapping the negative frequencies of subcarriers with the complex conjugate of the data on the positive subcarriers. The Hermitian symmetry operation is shown in a block with $\mathcal{H}$ in Fig. 2.9. Based on how a unipolar time domain signal is obtained, various types of optical OFDM schemes are proposed. A DC-biased optical OFDM (DCO-OFDM) is one of the most widely used spectrally efficient optical OFDM modulation schemes. In DCO-OFDM, a direct current bias is added to generate a unipolar signal [35, 88–90]. The additional DC requirement makes the scheme power inefficient com-

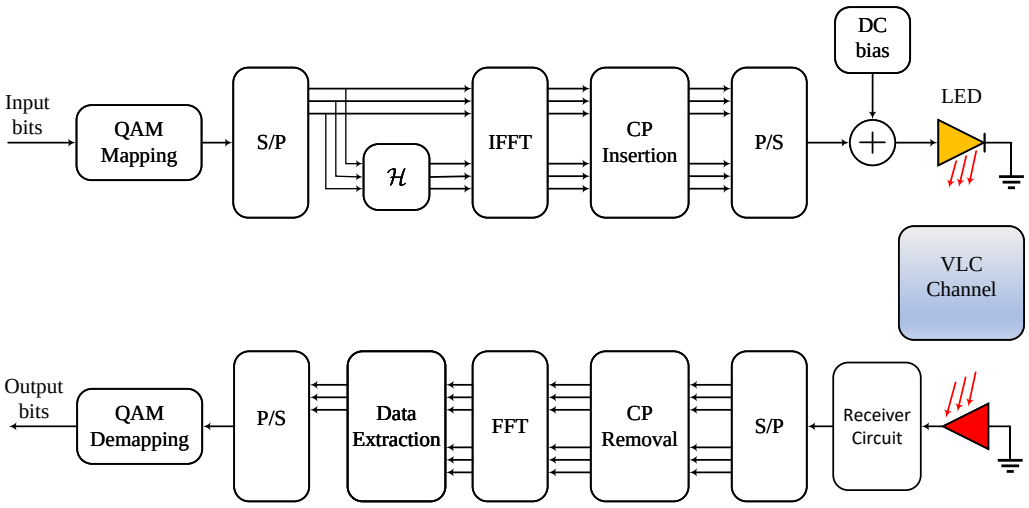

Figure 2.9: *A block diagram illustration of DCO-OFDM communication system. $\mathcal{H}$ denotes a Hermitian symmetry operation, S/P is serial-to-parallel conversion while P/S is parallel-to-serial conversion.*

pared to other forms of OFDM. However, uses all the available bandwidth efficiently [90, 91]. An alternative energy-efficient optical OFDM type is asymmetrically clipped optical OFDM (ACO-OFDM). In ACO-OFDM, in addition to the Hermitian symmetry, only the odd subcarriers are used for data transmission and the even subcarriers are set to zero [92]. This results in an asymmetric OFDM signal in the time domain, and by clipping and transmitting only the positive parts, ACO-OFDM signal is obtained. This approach results in an inherent unipolar signal, eliminating the requirement for DC biasing. However, only half of the available bandwidth is used for transmission [91]. More forms of unipolar OFDM schemes have been proposed to provide an energy-efficient alternative to DCO-OFDM. These include pulse amplitude modulated-discrete multitone modulation (PAM-DMT) [93], flipped OFDM [94], and unipolar OFDM (U-OFDM) [95]. However, all these schemes including ACO-OFDM have a reduced spectral efficiency compared to DCO-OFDM [84]. In this thesis, only DCO-OFDM will be considered for a spectrally efficient system. Furthermore, it should be noted that the power inefficiency associated with DCO-OFDM is not addressed in this study.

The DCO-OFDM frame is formed such that $X[k] = X^*[N_{\mathrm{FFT}} - k]$. In addition to this, $X[0] = X[N_{\mathrm{FFT}}/2] = 0$, where N_{FFT} is the number of subcarriers (the order of fast Fourier transform (FFT)), and $k = 0, 2, \cdots, N_{\mathrm{FFT}} - 1$ is the subcarrier index [90,96]. Mathematically,

this can be expressed as:

$$X[k] = \{0, X[1], X[2], \cdots, X[N_{\mathrm{FFT}}/2-1], 0, X^*[N_{\mathrm{FFT}}/2-1], \cdots, X^*[2], X^*[1]\}. \tag{2.9}$$

Here, $[\ \cdot\ ]^*$ denotes a complex conjugate operation. The waveform can then be expressed in the time domain as:

$$x[n] = \frac{1}{\sqrt{N_{\mathrm{FFT}}}} \sum_{k=0}^{N_{\mathrm{FFT}}-1} X[k] \exp\left(\frac{\mathrm{j}2\pi nk}{N_{\mathrm{FFT}}}\right), \qquad 0 \leq n \leq N_{\mathrm{FFT}} - 1. \tag{2.10}$$

To mitigate inter-symbol interference (ISI) caused by the multipath propagation of the OFDM signal, a cyclic prefix (CP) can be added. The CP is a copy of the last part of the OFDM symbol, and it is appended to the beginning of the symbol before it is converted into serial and transmitted [96].

At the receiver, data recovery starts with serial-to-parallel (S/P) conversion followed by removing the CP. The FFT operation transforms the received signal into its frequency domain equivalent to recover the data modulated onto each subcarrier. At this stage, the symmetry component is removed and a single-tap frequency domain equalisation can be employed on each subcarrier to retrieve the transmitted QAM symbols. Finally, after the parallel-to-serial conversion, QAM symbols are demodulated to recover the transmitted information bits.

2.5 Energy and Spectral Efficiency in VLC

Energy efficiency and spectral efficiency are two important metrics used to evaluate the performance of VLC systems. Energy efficiency refers to the ability of a communication system to transmit information with a low amount of energy. It is typically measured in bit per Joule (b/J), which indicates the number of bits of information that can be transmitted using a single Joule of energy. A communication system with high energy efficiency can transmit a large amount of information using a small amount of energy, making it more efficient and cost-effective. Spectral efficiency, on the other hand, refers to the ability of a communication system to utilise the available spectrum efficiently. It is typically measured in bit per second per Hertz (b/s/Hz), which indicates the number of bits of information that can be transmitted using a single Hertz of bandwidth. A communication system with high spectral efficiency can transmit a large amount of information using a small amount of bandwidth, making it more efficient and capable of sup-

porting more users or applications. In general, both energy efficiency and spectral efficiency are important metrics for evaluating the performance of VLC systems. Communication systems that are energy-efficient can reduce their power consumption and operating costs, while systems with high spectral efficiency can support more users or applications in a given frequency band. Improving both energy efficiency and spectral efficiency can help to maximise the capacity and performance of VLC systems. However, there is a trade-off between energy efficiency and spectral efficiency.

To understand the trade-off between energy and spectral efficiency, it is important to start with the limiting capacity of a linear channel formulated by Claude Shannon in [11]. It estimates the maximum bit rate that can be transmitted error-free at a given bandwidth B and average signal power constraint P_{s}, in a channel with a Gaussian distributed noise of average power P_{N}. Mathematically, the theoretical channel capacity limit C (in bit/s) which can be achieved in an error-free transmission for any specific modulation or coding scheme is given by [11]:

$$C = B \log_2 \left(1 + \frac{P_{\mathrm{s}}}{P_{\mathrm{N}}}\right) = B \log_2 \left(1 + \mathrm{SNR}\right). \tag{2.11}$$

Here, SNR is the signal-to-noise power ratio, which can also be defined in terms of SNR per bit. Given the symbol duration T_{s}, the average signal power of the transmitted symbol can be written in terms of average symbol energy as, $P_{\mathrm{s}} = E_{\mathrm{s}}/T_{\mathrm{s}} = E_{\mathrm{s}}R_{\mathrm{s}}$, where E_{s} is the average symbol energy and R_{s} is the symbol rate. Equivalently, P_{s} can be expressed in terms of energy per bit, E_{b} assuming a modulation order M. This is because $E_{\mathrm{s}} = E_{\mathrm{b}} \log_2 M$ and $R_{\mathrm{s}} = R_{\mathrm{b}}/\log_2 M$. Therefore, $P_{\mathrm{s}} = E_{\mathrm{s}}R_{\mathrm{s}} = E_{\mathrm{b}}R_{\mathrm{b}}$. On the other hand, the noise power, $P_{\mathrm{N}} = N_0 B$ where N_0 is the single-sided noise PSD. Consequently,

$$\mathrm{SNR} = \frac{P_{\mathrm{s}}}{P_{\mathrm{N}}} = \frac{E_{\mathrm{b}}R_{\mathrm{b}}}{N_0 B} = \frac{E_{\mathrm{b}}}{N_0}\eta. \tag{2.12}$$

Here, the SNR per bit, $\mathrm{SNR}_{\mathrm{b}} = E_{\mathrm{b}}/N_0$. While $\eta = R_{\mathrm{b}}/B$ is the spectral efficiency (in bit/s/Hz = bit/symbol) which measures the amount of information bit that can be transmitted in a given bandwidth. Using (2.12), it is possible to re-write the capacity limit in (2.11) and formulate the maximum spectral efficiency for an AWGN channels as:

$$\eta = \frac{C}{B} = \log_2 \left(1 + \frac{E_{\mathrm{b}}}{N_0}\eta\right). \tag{2.13}$$

Rearranging (2.13) for $\mathrm{SNR_b}$ gives:

$$\frac{E_\mathrm{b}}{N_0} = \frac{2^\eta - 1}{\eta}. \tag{2.14}$$

Equation (2.14) implies that SNR is an increasing function of the spectral efficiency. This is shown graphically in Fig. 2.10 (in solid dark line). Therefore, there is a trade-off between spectral efficiency and SNR requirement (sensitivity). That is, for a high spectral efficiency, high SNR is required. From (2.14), the lower bound of energy which is the minimum amount of SNR required to achieve an infinitesimal spectral efficiency can be found by:

$$\mathrm{SNR_{b,\,min}} = \left(\frac{E_\mathrm{b}}{N_0}\right)_{\mathrm{min}} = \lim_{\eta \to 0}\left(\frac{2^\eta - 1}{\eta}\right) = \ln 2 = -1.5917\ \mathrm{dB}. \tag{2.15}$$

This clearly shows that the trade-off between energy efficiency and spectral efficiency is an important consideration in the design and optimisation of VLC systems. The optimal trade-off between these two metrics will depend on the specific requirements and constraints of the communication system, such as the number of users or applications it needs to support, the available bandwidth and power, and the operating environment.

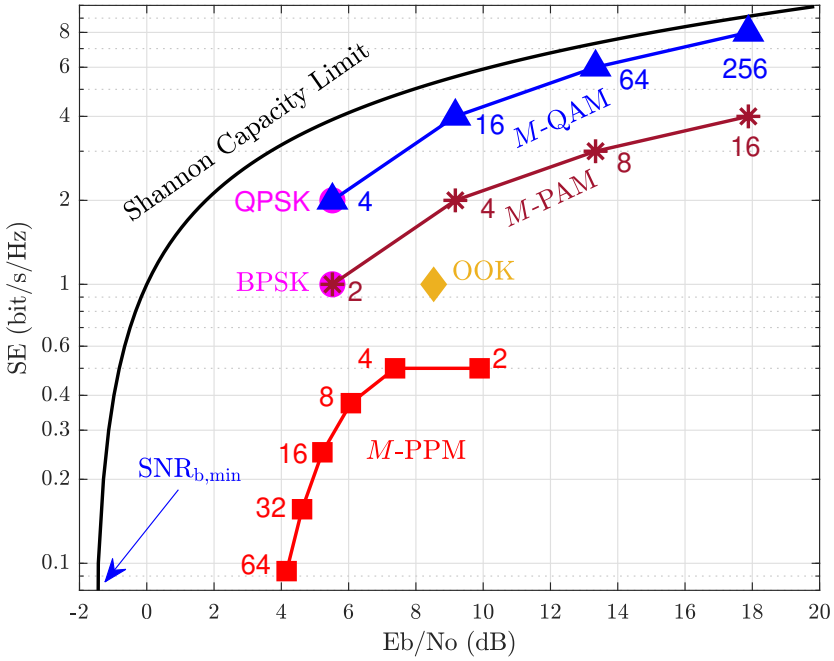

Figure 2.10: *Comparison of spectral efficiency vs SNR per bit of different modulation schemes limited by AWGN channel at BER* = 3.8×10^{-3}. *The Shannon capacity is also shown for reference.*

For applications which do not require high-speed data transmission, energy efficiency is the priority. These systems employ sensitivity constrained modulation schemes. On that regard, OOK can be seen as a benchmark. OOK offers a favourable balance between system performance and implementation complexity [9]. For a given bit rate, R_{b}, the bandwidth requirement of NRZ-OOK is inverse of the bit duration, $1/T_{\mathrm{b}}$ which is the bit rate R_{b}. That is, $B_{\mathrm{OOK}} = R_{\mathrm{b}}$. Therefore, the spectral efficiency of OOK is, $\eta_{\mathrm{OOK}} = 1$. Orthogonal modulation schemes such as PPM provide energy efficient system implementation at the cost of bandwidth. In these schemes, with increasing M, the energy efficiency tends toward the lower bound of energy, *i.e.* −1.5917 dB. In M-PPM, a number of $\log_2 M$ information bits is encoded by the position of an optical pulse within M equidistant time slots of a symbol duration. Therefore, for an identical bit rate R_{b}, the bandwidth requirement of M-PPM is:

$$B_{\mathrm{PPM}} = \frac{1}{T_c} = \frac{M}{\log_2 M}\frac{1}{T_{\mathrm{b}}} = \frac{M}{\log_2 M}R_{\mathrm{b}}. \tag{2.16}$$

The spectral efficiency of M-PPM is then $\eta_{\mathrm{PPM}} = \frac{\log_2 M}{M} < 1$.

Alternatively, modulation schemes with highest spectral efficiency can be chosen for high data rate transmission. These include PAM, phase shift-keying (PSK) and QAM. However, it comes at the cost of more SNR requirement. The goal of such systems will be to approach the capacity limit. For M-PAM, the bit rate is a product of the bandwidth used and the number of bits encoded in each symbol. That is $R_{\mathrm{b}} = B_{\mathrm{PAM}} \log_2 M$. Thus, the spectral efficiency is simply the number of information bits encoded: $\eta_{\mathrm{PAM}} = \log_2 M$. Similar spectral efficiency can be obtained in M-PSK and M-QAM. Unlike PAM, in PSK, the phase is varied in accordance with the digital information being transmitted. While in QAM, phase and amplitude modulations are combined using 2-dimensional in-phase and quadrature constellation points to encode information bits. Note that this spectral efficiency values represent theoretical maximum values that assume ideal channel conditions and perfect receiver performance. In practice, the actual spectral efficiency may be lower due to various factors that can degrade the quality of the transmitted signal and reduce the accuracy of the receiver. Overall, Fig. 2.10 shows the spectral efficiency against the amount of SNR per bit required to achieve a representative bit error rate (BER) = 3.8×10^{-3} in AWGN channel condition. Binary phase shift-keying (BPSK) and OOK achieve 1 bit/s/Hz spectral efficiency albeit the amount of SNR required is reduced by approximately −3 dB in BPSK. Higher spectral efficient systems can be realised using PAM or QAM schemes in which its efficiency increase with M. For low-rate applications, PPM is

is a convenient scheme as it provides energy efficient system alternative. In Chapter 5, another energy efficient modulation technique for low-data rate and low-power VLC applications is proposed.

2.6 Probabilistic Constellation Shaping

In the previous section, the trade-off between energy and spectral efficiency has been discussed. It is clear that enhancing energy and spectral efficiency and optimising the use of available scarce resources (energy and bandwidth) are crucial requirements of any communication system, including VLC. Yet, the theoretical upper bound of the information rate that can be achieved in an AWGN channel under a power constraint is limited to C as given by (2.11). This is possible only when the channel is fed by a transmitter source with a Gaussian distribution [11]. On the contrary, in conventional data transmission, each symbol is transmitted with equal probability. This uniform distribution of input symbols is not a perfect fit for the AWGN channel. Furthermore, the spectral efficiency is a coarse granular which can only lead to a discrete integer level. For example, $\eta = \log_2 M$ for M-QAM. Consequently, it does not allow for optimal utilisation of the channel capacity [12]. Thus, there exists a gap to the Shannon channel capacity [11,97]. Therefore, it is important to optimise the distribution of source symbols using signal shaping to close the gap.

Geometric shaping (GS) is one of the signal shaping techniques, where non-equidistant constellation points are used to approximate a Gaussian distribution [98]. In GS, symbols have equal probabilities and the goal is to have a signal constellation with a Gaussian-like geometry [99–102]. GS is typically based on ring constellations denoted which combines amplitude and phase-shift keying known as asymmetric phase-shift keying (APSK). Therefore, it does not require a distribution matcher, which maps input information bits into symbols with a desired probability distribution. However, the unequally spaced constellation points increase the DSP complexity and require a DAC with higher effective number of bits (ENOB) [103]. Moreover, determining the optimal constellation points for an arbitrary channel is not simple [104]. Another shaping method which has attracted significant interest is probabilistic shaping (PS). Here, the approach is to generate a Gaussian-like distribution over the signal structure. Therefore, in PS, the probability of occurrence of the constellation points are modified, rather than the positions, to form a Gaussian-like distribution [105–107]. Unlike GS, in PS, the probability of symbols can be optimised using a single parameter to fit an arbitrary channel condition [104].

Moreover, the fixed constellation positions make the DSP implementation simpler [104]. In this thesis, the focus is to the application of PS in VLC.

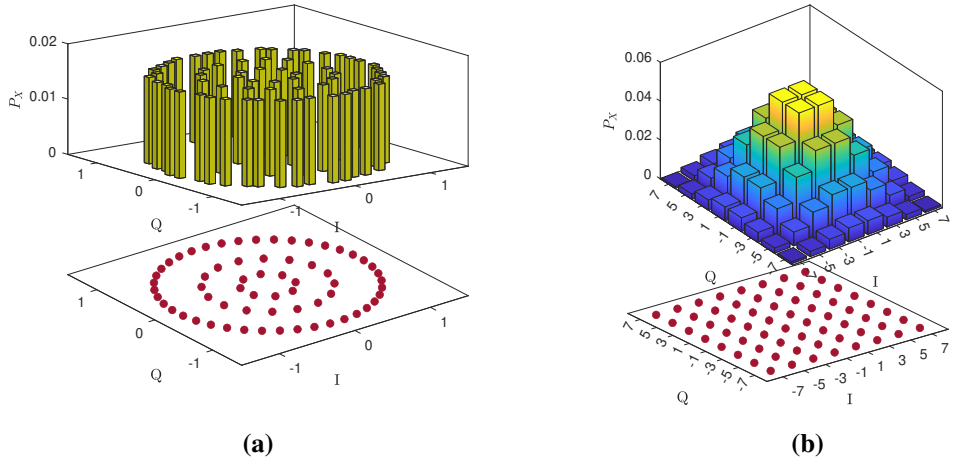

(a) **(b)**

Figure 2.11: *Graphical illustration of 64-QAM in geometric shaping (a) and probabilistic shaping (b) with the constellation points*

In order to have Gaussian source, symbols must be continuous and not restricted to a limited range of amplitudes. To realise this, the DAC and ADC need to have high resolutions. Moreover, the unlimited range of amplitudes result in large peak-to-average power ratios. These make a continuous Gaussian signalling difficult to work with in practice [104]. The way around this is to use discrete level of symbols which provide a Gaussian-like distribution. Several Gaussian-like distributions with discrete amplitudes across a finite range have been proposed to generate a Gaussian source. Some examples include exponential distribution, Pareto distribution, and Maxwell-Boltzmann distribution. These distributions determine the rate of information (entropy) based on the distribution of symbols, which in tern set a parameter called rate parameter, λ. For a modulation order, M, in the exponential distribution symbols at constellation points denoted by s_i are chosen by:

$$P\left(s_i\right) = \frac{\exp\left(-\lambda|s_i|\right)}{\mathrm{Z}\left(\lambda\right)}, \tag{2.17}$$

where,

$$\mathrm{Z}\left(\lambda\right) = \sum_{i=1}^{M} \exp\left(-\lambda|s_i|\right), \qquad \lambda \geq 0. \tag{2.18}$$

This distribution was applied to generate PS-based PAM symbols in direct detection system and has shown a 10% increase in the net data rate [108]. Meanwhile, in Pareto distribution the

probability of occurrence of symbols at a constellation point s_i is given by:

$$P\left(s_i\right) = \frac{\lambda s_{i_{\min}}^{\frac{\lambda}{s_i^{\lambda+1}}}}{\mathrm{Z}\left(\lambda\right)}, \tag{2.19}$$

where,

$$\mathrm{Z}\left(\lambda\right) = \sum_{i=1}^{M} \lambda s_{i_{\min}}^{\frac{\lambda}{s_i^{\lambda+1}}}, \qquad \lambda \geq 0, \tag{2.20}$$

and $s_{i_{\min}}$ is the minimum valued symbol among all symbols. In [109], it was shown that PS using Pareto distribution improves the performance of the colour shift keying (CSK) schemes. The other option of distribution is the Maxwell-Boltzmann distribution. Here, the probability of symbols at each constellation is selected from the Maxwell-Boltzmann distribution given by:

$$P\left(s_i\right) = \frac{\exp\left(-\lambda |s_i|^2\right)}{\mathrm{Z}\left(\lambda\right)}, \tag{2.21}$$

where,

$$\mathrm{Z}\left(\lambda\right) = \sum_{i=1}^{M} \exp\left(-\lambda |s_i|^2\right), \qquad \lambda \geq 0. \tag{2.22}$$

In all cases, $\mathrm{Z}\left(\lambda\right)$ is a normalisation factor which makes sure that the $\sum_{i=1}^{M} P\left(s_i\right) = 1$. Among the above Gaussian-like input distributions, it has been proven that the Maxwell–Boltzmann distribution is the optimal probability to maximise the entropy (and hence capacity) of the AWGN channel [106, Sec. IV], [110, Sec. VIII-A]. Due to this, in the literature that reports PS work, the Maxwell–Boltzmann distribution has been used frequently as an optimal Gaussian source [111–114]. In this thesis, the focus is towards using the Maxwell-Boltzmann distribution to generate a Gaussian-like PS input source and evaluate its potential in VLC systems.

Transforming independent and equiprobable input bits into a sequence of shaped output symbols with a desired distribution is the task of a distribution matcher. A constant composition distribution matcher (CCDM), proposed in [115], has drawn considerable interest to implement PS in optical fibre communication and achieve record-setting transmission rates and distances [12, 104, 111, 116]. The CCDM creates a target symbol distribution based on Maxwell-Boltzmann distribution by fixing the number of occurrence of symbols in each block length to n_s. That is a constellation point appears exactly n_i times out of the total block length giving $n_s = \sum_{i=1}^{M} n_i$. That leads to a probability mass function (PMF), $P\left(s_i\right) = \left[\frac{n_1}{n_s}, \cdots, \frac{n_M}{n_s}\right]$.

One of the benefits of using PS is a reduction in the amount of symbol energy. This is because in PS low-energy symbols (which are in the lower standard deviation of the Gaussian-like distribution) are transmitted more frequently than high-energy symbols. This will reduce the amount of average transmitted symbol energy at a specific error rate compared to the uniform distribution. This gain is known as shaping gain [106]. The gain in average energy, and thus consequently in SNR, will result in strong noise resilience and an increase in the achievable information rate for applications with limited signal power. The ultimate shaping gain which can be achieved using a continuous Gaussian symbol distribution is limited to $\pi \mathrm{e}/6$ ($\sim$ 1.53 dB) [110,117,118]. Therefore, the target of any practical system is to approach this ultimate shaping gain. Another advantage of PS is that it provides continuous and adaptive entropy transmission [12]. This is particularly important for multicarrier systems in which different levels of information bits are transmitted based on the channel frequency response [119–121]. In such systems, PS can provide a better fit to the channel response and achieves the desired data rate including approaching the channel capacity limit. PS has shown to be an optimum technique in optical fibre communications to achieve record-setting transmission rates and distances [12, 104, 111, 116, 122, 123]. Similar works have been reported enhancing the achievable information rate (AIR) of a VLC system [119–121, 124, 125].

2.7 Related Literature Comparative Discussion

The nonlinear distortion and limited modulation bandwidth of LEDs can have a negative impact on the performance of VLC systems. Therefore, techniques for enhancing the modulation bandwidth and mitigating distortion are important in VLC system design. One approach is to design the signal waveform in a way that is resistant to nonlinear distortion, such as by clipping the signal or scaling the amplitudes to fit within the linear range of the system. Another approach is to linearise the system nonlinearity, either at the transmitter or the receiver, through techniques such as pre-distortion or post-distortion. In high-speed VLC, the limited modulation bandwidth of LEDs can be a bottleneck, so optical OFDM in conjunction with adaptive information loading techniques have been proposed to increase the data rate. This section discusses these and other methods proposed in the literature for enhancing the performance of VLC systems.

Nonlinearity Mitigation and Enhancing the Modulation Bandwidth

Nonlinear distortion can degrade the performance of a VLC system, so distortion mitigation is crucial in a VLC system design. One way to tackle this problem is to design the signal waveform in such a way that it is not affected by nonlinear distortion. This can be realised by clipping the lower and/or upper bounds of the signal. Alternatively, the signal amplitudes can be scaled to fit in the linear region. These two methods are usually combined with DC bias point optimisation. In [72], a numerical method based on minimum mean square error (MMSE) criterion is proposed to optimise the DC bias that improves the BER performance. In [71], a low-complexity search algorithm is developed that finds the optimum biasing point, in addition to clipping, to maximise the system performance by enhancing the effective SNR of the system. The nonlinear modulation characteristics of LEDs were studied, and the bias current is optimised to minimise the error performance while increasing the modulation bandwidth [75].

Another approach is to linearise the system nonlinearity so that the input signal can be transmitted with minimal distortion or distortion-free. This signal processing can be carried out either at the transmitter or the receiver. In the transmitter, the transmitted signal is pre-distorted and transmission through the nonlinear system will reconstruct the original signal. Such work was reported in [70], where a pre-distortion technique combined with signal shaping is used to improve the link capacity. In [126], the nonlinearity is modelled by an equivalent discrete-time circuit which is then used to develop a nonlinear pre-distorter which inverts the distortion and enhances VLC link performance. While in [127], pre-distortion is applied with signal companding to improve system error performance. In the receiver side, it usually involves employing equalisers. A nonlinear feedforward decision feedback equaliser (DFE) was applied to compensate for nonlinearity in [74]. However, it has also been shown that the traditional linear equaliser is unable to recover the signal that has been distorted by the nonlinear LED response, and the nonlinear DFE is only effective when the signal is not highly distorted [126]. Recently, a pre-distortion scheme which is based on the Wiener-Hammerstein model was shown in a software-defined VLC link to mitigate nonlinearity in [128]. This was followed by another work which compared Hammerstein and Wiener VLC channels models [129]. In this work, a post-distortion based on the Hammerstein channel model was shown as a superior model to improve the system error performance. Overall, most of the existing works considered pre/post-distortion to linearise the dynamic range of the transmitted or apply clipping to limit the modulating signal in the linear region.

In this thesis, Chapter 3 presents two frameworks for optimising the DC bias of an LED to increase bandwidth at higher bias currents while minimising signal distortion. The proposed techniques involve either allowing for some nonlinear distortion or reducing signal swing while benefiting from higher bandwidth. The optimisation is also validated through experiment.

Adaptive Information Loading

For a high-speed VLC, the modulation bandwidth of LEDs is often a limiting factor. This means that the LED's ability to transmit data is restricted to a relatively narrow range of frequencies. As a result, the data rate that can be achieved using LEDs is often much lower than the data rate that can be achieved using other types of optical communication systems. To overcome this limitation and achieve higher data rates, it is necessary to modulate the signal beyond the −3 dB bandwidth of the LED. This can be accomplished using OFDM in conjunction with adaptive information loading (also known as adaptive bit loading). The available SNR of each subcarrier in all frequency ranges is estimated and information bits are allocated according to this pre-estimated SNR. Along with the bit allocation, the power in each subcarrier can be optimised to maximise the SNR resulting in adaptive bit-power loading. With such system, it is possible to transmit data at much higher rates, making LED-based communication systems more suitable for high-speed applications. Examples of literature demonstrating high data rate transmissions using a single LED include [40, 41, 59]. A wavelength division multiplexing (WDM)-based VLC has also been explored for higher data rates in [130–132].

In adaptive bit-power loading, discrete integer-level bits per symbol are allocated to each subcarrier. For example, for a given subcarrier, the pre-estimated SNR can accommodate 64-QAM which is 6 bit/symbol. Another subcarrier with lower SNR can only accommodate $M < 64$ which could be 5, 4, 3, or 2 bit/symbol. This does not provide the best possible fit for VLC channel frequency response. Thus, there still exists a capacity gap relative to the channel capacity limit formulated by Shannon [11]. To close this gap, the amount of information loaded should be adjusted to each subcarrier continuously, based on the pre-estimated SNR. This can be realised by PS-based optical OFDM. For such a scheme, a fixed modulation order, M-QAM symbols with different probabilistic distributions are applied to individual subcarriers based on the pre-estimated SNR. This provides continuous entropy loading that makes efficient use of the available bandwidth well beyond the −3 dB point.

Related literature applying PS in optical OFDM [2] in free-space VLC channel using LEDs include [119, 124]. While in UWOC system using laser diodes include [124, 125, 125]. In [119], a single LED VLC with PS-based OFDM is reported. However, despite the channel's capacity to accommodate higher modulation orders, the work is limited to PS with 256-QAM. Besides, subcarriers that are assigned to a group with the same QAM modulation order in the bit-loading scheme, are allocated with the same entropy in PS-256-QAM. This is contrary to the continuous entropy allocation that should fit the channel SNR response. A laser diode-based UWOC applying OFDM with PS-256-QAM has also been demonstrated to improve transmission capacity in [120, 125]. A similar approach with an laser diode-based VLC system using a higher-order format (PS-1024-QAM) is also reported in [124].

The rate adaptive feature of PS has also been employed for multiuser VLC access networks which adapt the rate based on a user's distance with PS in [121]. Just recently, a work which integrates PS with CSK was reported for enhancing the received SNR [109]. Also, in [133], PS is applied with spatial modulation-based VLC to improve system spectral efficiency. Here, PS is applied both to spatial and constellation symbols based on the user's location and SNR to maximise the achievable rate.

In this thesis, PS has been studied for use in optical OFDM-based VLC systems. In Chapter 4, the principle of adaptive entropy loading using PS is presented. The experimental demonstration of PS in both a single LED and WDM VLC systems is also discussed.

Energy Efficient Modulation Scheme

A low-rate wireless network requires simple, low-cost, and reliable communication with limited power consumption [134]. For such networks, energy efficiency is significantly important as applications using the network such as Internet of Things (IoT) use batteries which are intended to be used for a long duration [134, 135]. Meanwhile, VLC uses energy-efficient, low-cost, and ubiquitous LEDs and it is a suitable candidate for low-power systems [136]. Thus, using robust and sensitivity-constrained modulation techniques for VLC is essential.

Pulse modulation schemes are commonly used in IM/DD systems. Among various forms of pulse-based modulation schemes, OOK offers a good balance between system performance and

[2] In some literature, a digital baseband type of OFDM which uses bit-power loading based on pre-estimated SNR is also referred as discrete multi-tone (DMT).

implementation complexity [8, 9]. However, it is generally considered to be less energy efficient compared to other techniques. On the other hand, orthogonal modulation techniques such as PPM and frequency shift keying (FSK) can provide an energy-efficient system alternative at an expense of spectral efficiency [137–139]. In such schemes, the energy efficiency improves as the modulation order increases. PPM has been implemented in [86, 140], and shown in an experimental demonstration in [137, 141]. Nevertheless, PPM suffers a high peak-to-average power ratio (PAPR) and is sensitive to receiver synchronisation which requires complex equalisation [85–87].

An alternative orthogonal modulation technique which overcomes the limitations of PPM is FSK. It maintains a constant amplitude envelope as the amplitude of the transmitted signal remains unchanged regardless of the data being transmitted. This property makes FSK relatively easier to equalise or adjust the balance of the signal to remove distortions caused by the transmission medium. As a result, FSK requires simpler equalisation compared to other types of digital modulation [82, 142]. Inspired by these, several energy-efficient FSK modulation technique which satisfies unipolar and real-valued constraints of the IM/DD system were proposed [143, 144]. In [143], an energy-efficient unipolar variant of FSK which transmits the positive and sign flipped negative amplitudes in two consecutive symbol periods is proposed for low-data rate and low-power IoT applications. An asymmetric frequency shift keying (AFSK) which uses two rectified frequency tones to represent two symbols was also proposed for VLC [144]. In both cases, it was shown that the proposed FSK modulation is energy efficient relative to OOK and PAM. Yet, the FSK in [143] requires a complex maximum likelihood receiver.

In a communication system using FSK, the information is conveyed by shifting the frequency between two or more predetermined frequencies. On the other hand, a VLC channel is frequency selective by its nature [64]. Therefore, the channel response, or the amount of attenuation or amplification applied to different frequencies, is not the same for all frequencies. This means that the FSK symbols, which are transmitted at different frequencies, may not be received with the same strength. If the FSK symbols are mapped onto frequency regions where the channel has a large attenuation, the signal strength of those symbols will be reduced, making them more difficult to detect accurately. This can lead to errors in the communication system, reducing its performance.

One way to address this issue is to map each symbol to all frequencies linearly within the available bandwidth. This means that each symbol is spread out over a range of frequencies rather than being concentrated at a single frequency. That is a symbol is mapped to all frequencies linearly within the bandwidth forming a frequency shift chirp modulation (FSCM); also known as chirp spread spectrum (CSS) in LoRa [145, 146]. This can help to reduce the impact of the frequency selective channel, improving the performance of the system. This scheme has been studied well in literature including the error performance analysis and transmitter design for RF-based communication system [145, 147, 148].

There has been significant progress in VLC and LiFi research, but these advancements are not specifically aimed at resource-constrained devices [149]. The electrical and computing power limitations of IoT nodes require the development of energy-efficient modulation. Such a scheme should be able to transmit data effectively while minimising energy consumption. Despite their limitation discussed above, pulse-based modulation techniques, such as OOK and PPM, and FSK have been considered more suitable for resource-constrained. In this thesis, an alternative energy-efficient modulation technique called FSCM is proposed for low-data rate and low-power VLC applications. In Chapter 5, the principle of FSCM including signal generation and detection, error performance, and experimental demonstration is presented.

2.8 Summary

In this chapter, a comprehensive overview of VLC system relevant to the thesis has been presented. The chapter begins with a brief overview of VLC and its current status as a focus of research in optical wireless communication. It also provides introduction to VLC and its potential as a promising technology for various communication applications. The features of a VLC system, including its advantages over other communication technologies, its potential application areas, and the challenges that need to be addressed in order to fully realise its potential have been presented. Moreover, the system components in VLC, including the optical transmitters and receivers that are used to transmit and receive the optical signals, as well as VLC channel model, which represent the characteristics of the channel through which the optical signals are transmitted have been described. In addition, the chapter covers the various modulation techniques used in VLC, including pulse modulation techniques such as OOK, PAM, and PPM, as well as optical OFDM.

The chapter also discusses energy and spectral efficiency in VLC, highlighting the importance of maximising the use of the available bandwidth and minimising energy consumption in order to achieve high data rates and low-power communication. It is noted that finding a balance between energy efficiency and spectral efficiency is crucial when designing VLC systems. The optimal balance between these two metrics will depend on the specific needs and limitations of the communication system, such as the number of users or applications it needs to support, the available bandwidth and power, and the operating environment. The chapter also covers a discussion of probabilistic shaping, a technique used to improve the performance of high-speed VLC systems by optimising the signal constellation in the presence of noise. PS allows for continuous and adaptive entropy transmission, which is especially useful for optical OFDM-based VLC systems where different levels of information bits are transmitted in each subcarrier based on the channel frequency response. The chapter also includes a comparative discussion of related literature to the theme of the thesis.

This thesis will explore ways to improve the limited modulation bandwidth of LEDs, utilise adaptive information loading with PS, and implement energy-efficient modulation schemes for low-power applications. These techniques will be examined in more depth in subsequent chapters, as outlined in the introductory chapter.

Chapter 3
Bias Point Optimisation of LEDs for Capacity Enhancement

3.1 Introduction

Significant research effort has been put towards the development of high-speed VLC. Yet, such a system needs to address the challenges associated with the relatively low modulation bandwidth of commercial LEDs [150]. Various techniques such as pre- and post-equalisation, high-order modulation with OFDM have been explored to optimise the modulation bandwidth and achieve high data rates in the range of several Gb/s using a single LED [41, 42]. It has also been demonstrated that the LED modulation bandwidth increases as bias current increases until it saturates [74, 75]. However, an LED is a nonlinear device. That is, its emitted optical power as a function of the driving current is not completely linear. Consequently, driving the LED in the nonlinear region distorts the transmitted signal and deteriorates the system performance [68]. Therefore, it is imperative to optimise the DC bias point of an LED to benefit from increasing bandwidth at driving current while minimising any nonlinear distortion associated with operating beyond the dynamic range of the LED. This way, the achievable transmission capacity of the LED-based VLC system is enhanced.

In this chapter, two different methods of choosing the optimum DC bias point for intensity modulated VLC systems are discussed. The first approach considers increasing the DC bias from the mid-point of the linear region for higher modulation bandwidth which also leads to nonlinear distortion. Here, the effect of distortion on the system capacity is evaluated. The second approach investigates increasing the DC bias while keeping the modulating signal within the dynamic range of the transmitter. In this approach, the signal power is compressed, and the optical modulation index is reduced. As such, the SNR decreases as DC bias increases. Thus, the optimum DC bias that provides maximum capacity by increasing the modulation bandwidth is evaluated. Moreover, these optimisation techniques can be used together with existing pre/post equalisation and precoding/pre-distortion techniques. An experimental validation of the second optimisation method is also presented.

The remainder of the chapter is organised as follows. The characteristics of an LED, including its optical power and modulation bandwidth, and how these characteristics are affected by the drive current will be described in Section 3.2. The theoretical study of bias point optimisation, including the system design and principles of the optimisation methods will be discussed in Section 3.3. Specifically, the VLC channel model assumption and link capacity, as well as the bias point optimisation itself, will be examined. Simulation results and discussions will also be presented to further illustrate these concepts. In Section 3.4, an experimental validation of one of the optimisation methods, including the experiment setup and results, will be presented. Finally, the key points discussed in this chapter will be summarised in Section 3.5.

3.2 Characteristics of LED

An LED is a semiconductor device with *p*-type and *n*-type junctions confined inside a hetero-junction. When an LED is connected to a forward bias current, electrons are excited to the higher energy state (conduction band). As an electron in the excited state is unstable, it returns to the ground state spontaneously emitting a photon. This process is known as spontaneous emission. It is attributed to the spontaneous optical power radiation of LEDs. The amount of energy released due to this spontaneous emission is equivalent to the energy band-gap of the material made from. The peak wavelength (colour) of the radiated optical power is also mainly determined by the band-gap energy of the junction which in turn depends on the semiconductor material [8, 77].

Photons are radiated in random directions incoherently and only some of the radiated photons contributed to the light in the desired direction. Yet, the radiated optical power increases as the driving current increases. However, the response becomes nonlinear for a larger current. This is attributed to two reasons. The first is when the drive current increase, the junction temperature in the active area increases and it reduces the efficiency of the LED. Second, the increase in drive current causes an overflow of carriers in the active region. This will not increase the carrier concentration in the active region. Hence, the optical power saturates and leads to distortion in the modulating signal [8, 77]. A visual illustration of an LED response using a random modulating signal, $x\left(t\right)$ is shown in Fig. 3.1. In this instance, the LED is biased at i_{bias} by adding an offset current α to the mid-point bias current i_{mid}, that is $i_{\mathrm{bias}} = i_{\mathrm{mid}} + \alpha$ such that $i_{\mathrm{mid}} = i_{\mathrm{max}}/2$. Here, i_{max} denotes the maximum allowable bias current before saturation.

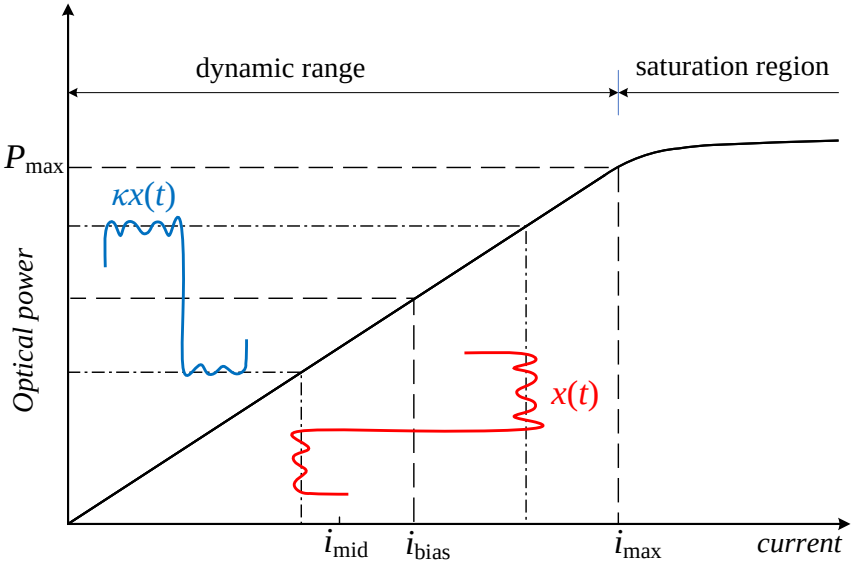

Figure 3.1: *Graphical illustration of an LED response biased at i_{bias} using a random modulating signal, $x\,(t)$. The maximum allowable bias current of the LED is $i_{\max}$ and the mid-point is $i_{\text{mid}} = i_{\max}/2$.*

Another important characteristic of an LED is its bandwidth. The modulation bandwidth of an LED determines the transmission rate and channel capacity of a VLC system. The frequency response of an LED depends on the driving current, carrier recombination lifetime in the active region, and the junction and parasitic capacitance. Therefore, the modulation bandwidth is limited by the response rate, which by itself is affected by the minority carriers lifetime, τ_{c} of the semiconductor. The −3 dB modulation bandwidth, which is defined as a frequency at which the power of an arbitrary transmitted signal drops by half, can be given as [77]:

$$f_{3\text{ dB}} = \frac{\sqrt{3}}{2\pi\tau_{\text{c}}}. \tag{3.1}$$

The modulation bandwidth of commercially available LEDs is often limited to only a few MHz [8,59]. However, like the optical power output, the modulation bandwidth is proportional to the drive current. Therefore, using an optimum drive current is important to benefit from increasing bandwidth at a higher driving current while minimising the resulting signal distortion.

In the subsequent discussions, the transmission bandwidth of the VLC link and the optical power output of the LED are modelled as a function of the bias current. The relationship is linear within the dynamic range and a constant value is assumed outside this region. Therefore,

the optical power can be written as:

$$P_{\text{opt}} = \begin{cases} m_O i_{\text{bias}}, & i_{\text{mid}} \leq i_{\text{bias}} < i_{\max_{\text{P}}} \\ P_{\max}, & i_{\text{bias}} \geq i_{\max_{\text{P}}}. \end{cases} \tag{3.2}$$

Similarly, the modulation bandwidth can be formulated as:

$$B = \begin{cases} m_B i_{\text{bias}}, & i_{\text{mid}} \leq i_{\text{bias}} < i_{\max_{\text{B}}} \\ B_{\max}, & i_{\text{bias}} \geq i_{\max_{\text{B}}}. \end{cases} \tag{3.3}$$

In the above equations, m_B and m_O denote the slopes of the linear functions of the dynamic ranges with a maximum bandwidth, $B_{\max}$ at drive current $i_{\max_{\text{B}}}$ and maximum power, $P_{\max}$ at drive current $i_{\max_{\text{P}}}$, respectively. For most LEDs the maximum bias current before saturation in bandwidth and optical power are identical. Therefore, $i_{\max_{\text{B}}} = i_{\max_{\text{P}}} = i_{\max}$. In the following section, the DC bias point optimisation problem as well as the VLC system model is presented.

3.3 Theoretical Study

A considerable amount of nonlinearity in VLC systems comes from the LED. That is because the relationship between the DC bias current and the output optical power is not fully linear. Thus, to minimise the effect of nonlinearity distortion on VLC systems, the data carrying signal should be within the linear dynamic range of the LED [151]. This is usually achieved by biasing the LED at the mid-point of its dynamic range [152]. In this work, two different approaches of choosing the DC bias (operating) point are explored. In the first approach, the modulating signal amplitude is kept constant while the bias current is increased from the mid-point of the dynamic range. In this approach, some of the signal go into the nonlinear region, introducing some distortion but operating at higher bias current offers much higher bandwidth. The second approach will be to increase the bias point while keeping the signal within the dynamic range of the LED. Thus, the signal power is reduced while the bandwidth is increased. In this method, the response of the LED is considered to be distortion-free.

3.3.1 System Design and Assumptions

The bias point optimisation technique in this chapter is based on the channel model provided in the introductory chapter of Section 2.3.3. Therefore, the VLC system with linear, time-invariant channel model shown in Fig. 2.4 is considered. The challenge in both methods is to find the optimum DC bias point that maximises the link capacity. Other sources of distortions are not considered in this work. Therefore, the modulating signal bandwidth is assumed to be less than the LED bandwidth.

In a LiFi system, the LoS communication link is typically the dominant link due to the fact that the power contributed by the NLoS paths is usually much smaller compared to the LoS signal power [81]. The channel DC gain, $H(0)$ is determined by the combination effect of the LoS and NLoS paths. In this thesis, a LoS link characterised by its channel DC gain is considered. If both NLoS and LoS links are to be considered, $H(0)$, which is a scaling factor in the SNR evaluation, will be different. However, the optimisation process remains the same.

In the bias point optimisation analysis to follow, the focus is on optimising the bias point at the fixed access point, which could be a ceiling or desk lamp, using a commercially available LED. The optimisation process is carried out during the setup phase to ensure efficient and optimal operation of the system during data communication. The optimisation can also be applied to a mobile user device where the process would be carried out independently for each device due to the continuously changing channel conditions. Consequently, there may be differences in the absolute optimum operating points for different users. The value of the optimised bias point is affected by several factors, including the LED and photodetector characteristics such as radiant intensity, active area and field of view, as well as the distance and orientation between the transmitter and receiver, and any obstacles in the path between them. These factors determine the channel DC gain, which in turn affects the available SNR. This chapter presents techniques for obtaining the optimum bias point, which is independent of the multiple access technique being used. Therefore, the proposed bias point is not affected by the specific method used to allow multiple users to access the system simultaneously.

For a VLC system with sufficient DC bias and a Gaussian distributed signal, the link capacity can be adequately represented by the Shannon equation given by (2.11). The SNR and B are functions of the bias current, i_{bias}. Therefore, in both methods the task will be to evaluate the optimum i_{bias} that maximises the capacity.

3.3.2 Bias Point Optimisation

Two different biasing methods are examined to evaluate the effect on SNR and consequently the capacity of the link. In the first method (*Method* 1, hereafter), the effect of distortion on SNR is studied by increasing the bias current and driving the LED into saturation region. In the second method (*Method* 2, hereafter), the LED is operating in the non-saturation region by compressing the modulating signal within the linear region. In this method, the result of squeezing the signal in linear region on SNR is studied as the driving current is increased.

Graphical illustration of these two methods is shown in Fig. 3.2 using a bias current against optical power output response of a typical VLMB1500 LED [153]. Here, a Gaussian distributed

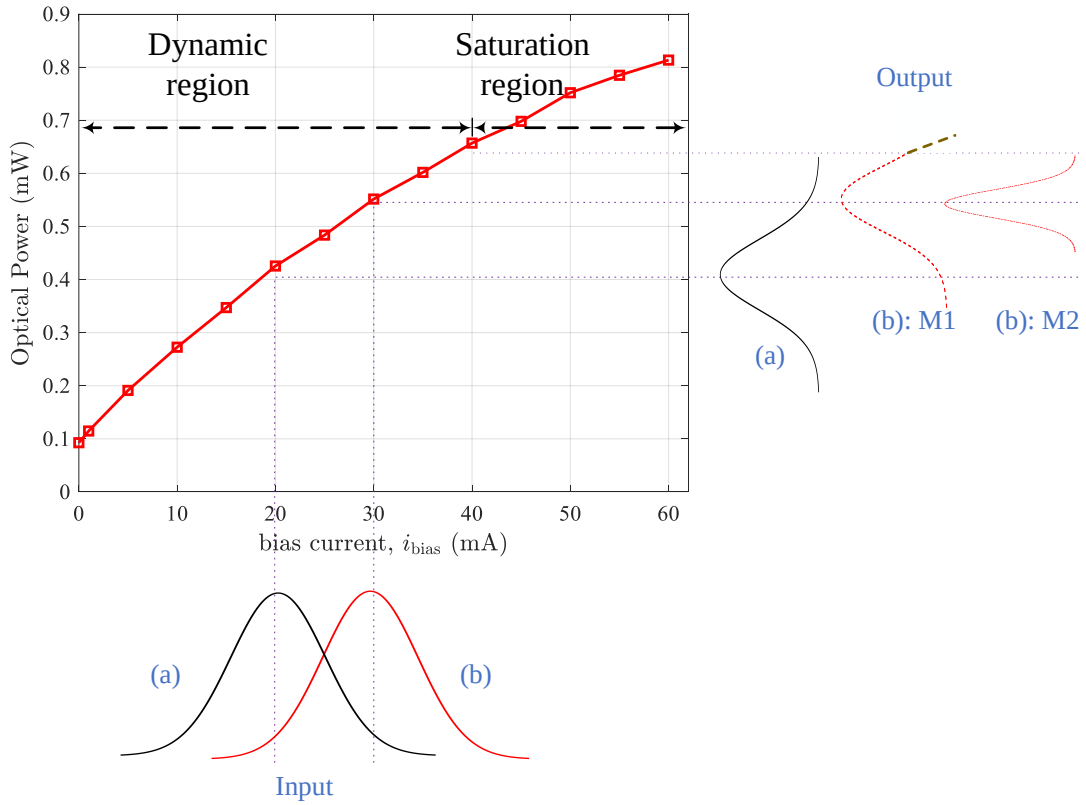

Figure 3.2: *Graphical illustration demonstrating the two bias optimisation methods: bias optimisation with constant signal amplitude and distortion and bias optimisation with no distortion*

modulating signal and two instances of offset currents, $\alpha = [0, 10]$ mA and thus biasing at $i_{\text{bias}} = i_{\text{mid}} + \alpha = [20, 30]$ mA are considered. Input signal biased at $i_{\text{bias}} = 20$ mA is labelled (a) while (b) shows the signal biased at $i_{\text{bias}} = 30$ mA. When $i_{\text{bias}} = 20$ mA is used, the LED is modulated in the linear region only and can be considered as distortionless (illustrated in the

black-solid Gaussian input and output signal labelled (a)). In *Method* 1, when $i_{\text{bias}} = 30$ mA, there is modulation of LED in the nonlinear region and results in distortion (shown in red-dash Gaussian input and distorted output signal labelled (b): M1). The amount of distortion should be estimated by comparing the signal power in the non-linear region to the total signal power and evaluate the resulting SNR and distortion ratio. In *Method* 2, when $i_{\text{bias}} = 30$ mA, the signal is compressed within the linear region of the LED (shown in red-solid Gaussian output signal labelled (b) M2). In this method, distortion is negligible, and the signal scaling factor needs to be evaluated to estimate the SNR. In the following, these two proposed methods are discussed in details.

Method 1: Bias Optimisation with Constant Signal Amplitude and Distortion

Due to the modulation of LED into the nonlinear region, the transmitted signal is distorted. The amount of distortion can be estimated as a ratio of power in saturation region to the total signal power. Therefore, the distortion factor, Δ can be expressed as a function of the bias point, $i_{\text{bias}} = i_{\text{mid}} + \alpha$ as:

$$\Delta\left(i_{\text{bias}}\right) = \frac{\int_{i_{\max}}^{i_{\max}+\alpha} x^2 f\left(x\right) dx}{\int_{-\infty}^{\infty} x^2 f\left(x\right) dx}, \tag{3.4}$$

where $f\left(x\right)$ is the probability density function (PDF) of $x(t)$, $i_{\max}$ is the maximum allowable drive current before saturation and α is offset from the mid-point current, i_{mid}, as shown in Fig. 3.1. In this equation, the numerator represents the signal power loss due to distortion while the denominator represents the total signal power. For computational simplicity, the zeroth moment expressions of (3.4) which can be simplified to ratio of two cumulative distribution functions is used. This gives:

$$\Delta\left(i_{\text{bias}}\right) \approx \frac{\int_{i_{\max}}^{i_{\max}+\alpha} f\left(x\right) dx}{\int_{-\infty}^{\infty} f\left(x\right) dx}. \tag{3.5}$$

Equation (3.5) is reasonable approximation of (3.4). To illustrate the validity of the approximation, numerical evaluation of equations (3.4) and (3.5) is carried out and the values are plotted in Fig. 3.3 assuming a Gaussian distributed signal $x(t)$. It shows that up to 35 mA bias current, equations (3.4) and (3.5) have similar values and above 35 mA equation (3.5) underestimates the distortion by less than 4%.

Due to the operation in the nonlinear region, the signal power is attenuated. Using the distortion

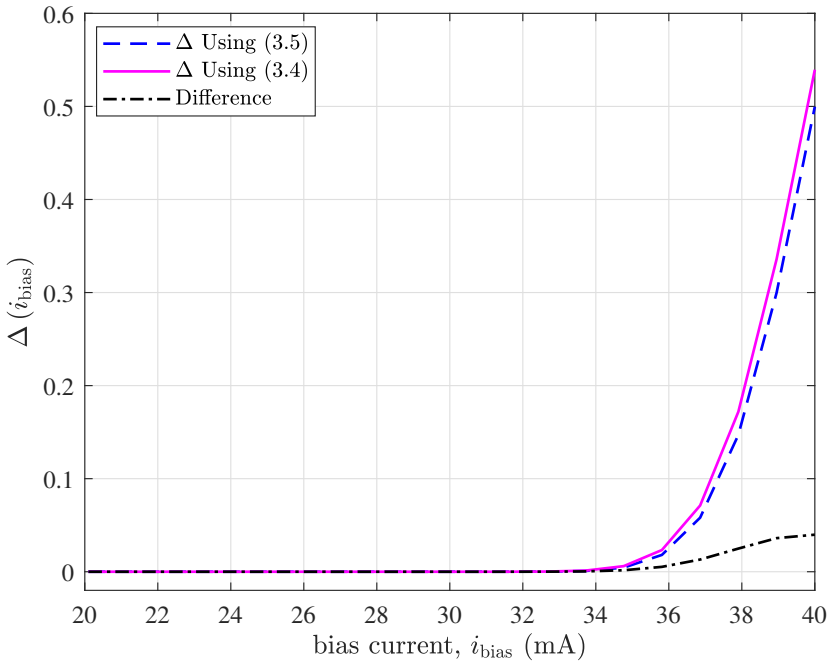

Figure 3.3: *Distortion factor, Δ as function of i_{bias} using equations (3.4) and (3.5)*

factor in (3.5), the attenuated signal power can be evaluated by:

$$P_{\text{s}} = (1 - \Delta)\, \mathbb{E}\left[|x\,(t)|^2\right]. \tag{3.6}$$

This shows that out of the transmitted modulating signal power, $\mathbb{E}\left[|x\,(t)|^2\right]$, only the information within the linear region is considered part of the important information-carrying signal power. The rest of modulating signal power, which is the information contained in the distortion region, contributes to interfering power. This is evaluated by using the distortion factor in (3.5) as follows:

$$P_{\text{I}} = \Delta \mathbb{E}\left[|x\,(t)|^2\right]. \tag{3.7}$$

In the above equations, $\mathbb{E}\left[\cdot\right]$ denotes the statistical expectation. This interfering power depends on the probability distribution of the signal and the biasing current, and it does not necessarily take into account the white power spectral density. The electrical SNR of the VLC model with distortion can then be expressed as:

$$\text{SNR}_{\text{M1}}\left(i_{\text{bias}}\right) = \frac{\kappa^2 R^2 H^2\left(0\right) P_{\text{s}}}{\sigma_{\text{n}}^2 + \kappa^2 R^2 H^2\left(0\right) P_{\text{I}}}, \tag{3.8}$$

where $H\left(0\right) = \int_{-\infty}^{\infty} h\left(t\right) \mathrm{d}t$ is the channel DC gain, which can be also evaluated by (2.8). The

second term in the denominator (3.8) accounts for the distorted signal power. Subsequently, for *Method* 1, the link capacity as a function of bias current $C_{\mathrm{M1}}\left(i_{\mathrm{bias}}\right)$ is obtained by combining (2.2), (2.3), (2.6), (3.2), (3.3), and (3.8) for $i_{\mathrm{mid}} \leq i_{\mathrm{bias}} < i_{\max}$ as:

$$C_{\mathrm{M1}} = m_B i_{\mathrm{bias}} \log_2 \left(1 + \frac{\kappa^2 R^2 H^2\left(0\right) P_{\mathrm{s}}}{2\left(qRm_O i_{\mathrm{bias}} + \frac{2\mathrm{K_B}T}{R_{\mathrm{L}}}\right) m_{\mathrm{B}} i_{\mathrm{bias}} + \kappa^2 R^2 H^2\left(0\right) P_{\mathrm{I}}} \right). \tag{3.9}$$

***Method* 2: Bias optimisation with no distortion**

In this method, the bias current is increased while the signal is compressed within the linear region of the LED. The signal scaling factor, ζ is used to keep the modulating signal within the linear dynamic range of the LED. As a function of bias current, ζ can be written as:

$$\zeta\left(i_{\mathrm{bias}}\right) = \begin{cases} \frac{i_{\max} - i_{\mathrm{bias}}}{\max|x(t)|}, & \max|x(t)| > i_{\max} - i_{\mathrm{bias}} \\ 1, & \text{otherwise.} \end{cases} \tag{3.10}$$

In *Method* 2, as the signal, $x(t)$ is constrained to the linear region only, there is negligible distortion. Thus, the electrical SNR is reduced to:

$$\mathrm{SNR}_{\mathrm{M2}}\left(i_{\mathrm{bias}}\right) = \frac{\kappa^2 R^2 H^2\left(0\right) \zeta^2 \mathbb{E}\left[\left|x\left(t\right)\right|^2\right]}{\sigma_{\mathrm{n}}^2}. \tag{3.11}$$

Similar to *Method* 1, the link capacity as a function of the bias current for *Method* 2, $C_{\mathrm{M2}}\left(i_{\mathrm{bias}}\right)$ is obtained as:

$$C_{\mathrm{M2}} = m_B i_{\mathrm{bias}} \log_2 \left(1 + \frac{\kappa^2 R^2 H^2\left(0\right) \zeta^2 \mathbb{E}\left[\left|x\left(t\right)\right|^2\right]}{2\left(qRm_O i_{\mathrm{bias}} + \frac{2\mathrm{K_B}T}{R_{\mathrm{L}}}\right) m_{\mathrm{B}} i_{\mathrm{bias}}} \right). \tag{3.12}$$

The link capacity expressions (3.9) and (3.12) are a product of a monotonically increasing linear function and a decreasing logarithmic function. Hence, there exist an optimum bias current, $\hat{i}_{\mathrm{bias}}$, which provides maximum link capacity. This optimum bias current with $i_{\mathrm{mid}} \leq \hat{i}_{\mathrm{bias}} < i_{\max}$ will satisfy:

$$\frac{\partial C_{\mathrm{M1|2}}\left(i_{\mathrm{bias}}\right)}{\partial i_{\mathrm{bias}}} = 0 \quad \text{and} \quad \frac{\partial^2 C_{\mathrm{M1|2}}\left(i_{\mathrm{bias}}\right)}{\partial i_{\mathrm{bias}}^2} < 0. \tag{3.13}$$

A closed-form analytical solution to (3.13) is untractable. However, a solution can be obtained with root-finding numerical methods. Moreover, to show the effect of the bias current on achievable capacity, a graphical solution of (3.13) is explored.

3.3.3 Simulation Results and Discussions

This section presents simulation results of the bias optimisation methods. In the simulation, a commercially available off-the-shelf LED VLMB1500 is used [153]. Its optical power response is characterised and presented in Fig. 3.4. The maximum allowable bias current before saturation in power is 40 mA for this particular LED. The response up to this current is fitted with a line which shows a firm coefficient of determination, $R^2 = 0.9916$. The modulation bandwidth

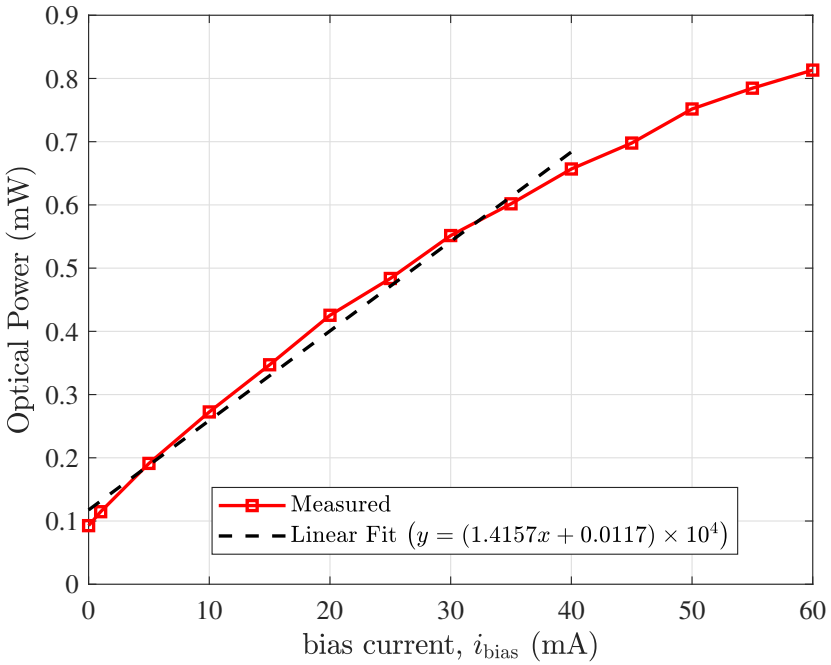

Figure 3.4: *Characteristics of VLMB1500 LED at different bias current showing measured output optical power and a linear fit with* $R^2 = 0.9916$

response is also measured and shown in Fig. 3.5. Similarly, the maximum bias current before saturation in bandwidth is 40 mA. The line fit in the dynamic region shows a strong coefficient of determination $R^2 = 0.9999$.

For the simulation example presented here, a maximum drive current of 40 mA is considered based on the VLMB1500 LED whose characteristics are plotted in Fig. 3.4 and Fig. 3.5. The bias current is started from the mid-point (20 mA) and increased to the maximum (40 mA)

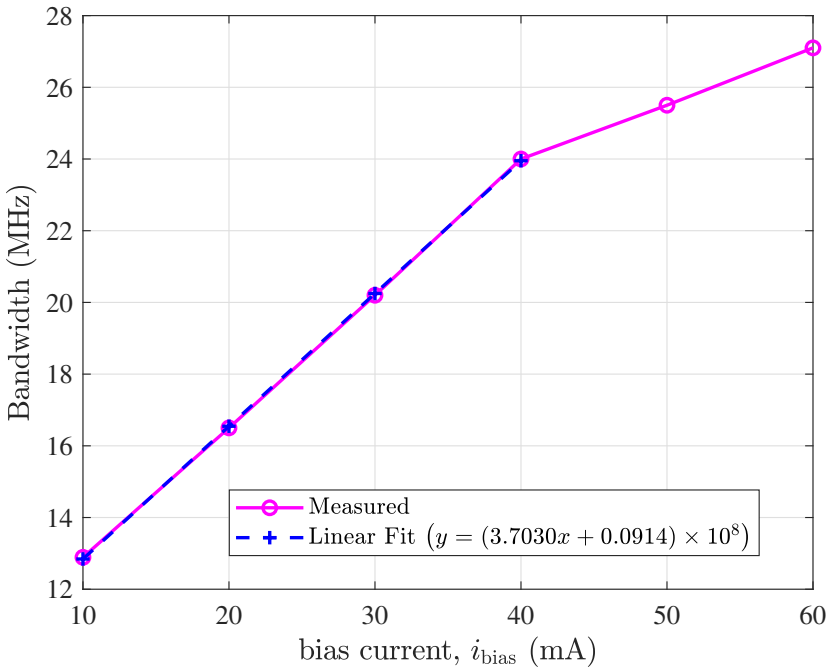

Figure 3.5: *Characteristics of VLMB1500 LED at different bias current showing measured −3 dB electrical bandwidth and linear fit with* $R^2 = 0.9999$

aiming to graphically determine the optimum drive current which provides maximum capacity. The simulation parameters are summarised in Table 3.1.

The first evaluation is carried out to the impact of the bias point optimisation methods to the signal power and the result is shown in Fig. 3.6. In *Method* 1, the signal power remains unchanged until the signal reaches the saturation region. Once the bias current reached around 35 mA, some content of the signal will be modulated in the saturation region. Therefore, the signal power is distorted. The signal power is reduced by about 3 dB when biased at 40 mA compared to 30 mA. The distorted signal power adds to the interfering signal power as given by (3.7). In *Method* 2, as the the bias current is increased, the modulating signal is kept in the linear region by decreasing the signal swing. This is done by multiplying the modulating signal by the scaling factor, ζ given by (3.10). Consequently, the signal power is always decreasing with increasing bias current.

Once the signal power against the bias current is estimated, the resulting SNR is evaluated using (3.8) and (3.11) for *Method* 1, and *Method* 2, respectively. The result is plotted at Fig. 3.7. The SNR in *Method* 1, stays fairly constant up to 27 mA. This is due to the fact the signal power is constant and there is no distortion up to this bias current. Furthermore, the impact of noise is

Table 3.1: *Simulation Parameters*

Parameter	Value
Average transmitted signal power, $\mathbb{E}\left[\left\|x\left(t\right)\right\|^2\right]$	1 W
Maximum allowable bias current, $i_{\max}$	40 mA
Slope of the dynamic range (bandwidth), m_{B}	370.30 MHz/A
Slope of the dynamic range (power), m_{O}	14.15 mW/A
Maximum bandwidth, $B_{\max}$	23.952 MHz
Maximum optical power, $P_{\max}$	0.6838 mW
Electrical-to-optical conversion factor of LED, κ	14.15 mW/A
Channel DC Gain, $H(0)$	1
Responsivity of photodetector, R	0.28 A/W
Electron charge, q	1.6021×10^{-19} C
Boltzmann's constant, $\mathrm{K_B}$	1.3806×10^{-23} J/K
Absolute temperature, T	300 K
Load resistance, R_{L}	50 Ω

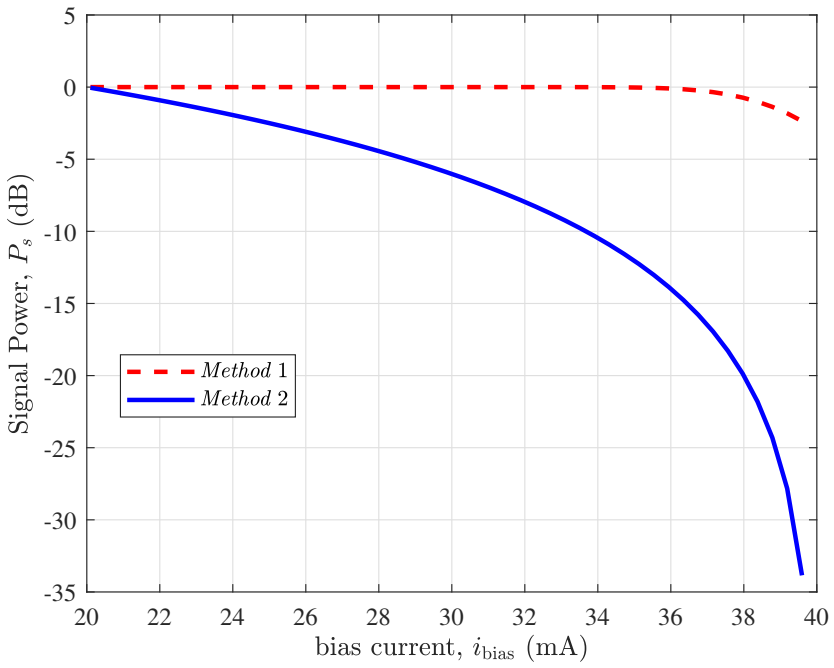

Figure 3.6: *Signal power against bias current for Method 1 and Method 2*

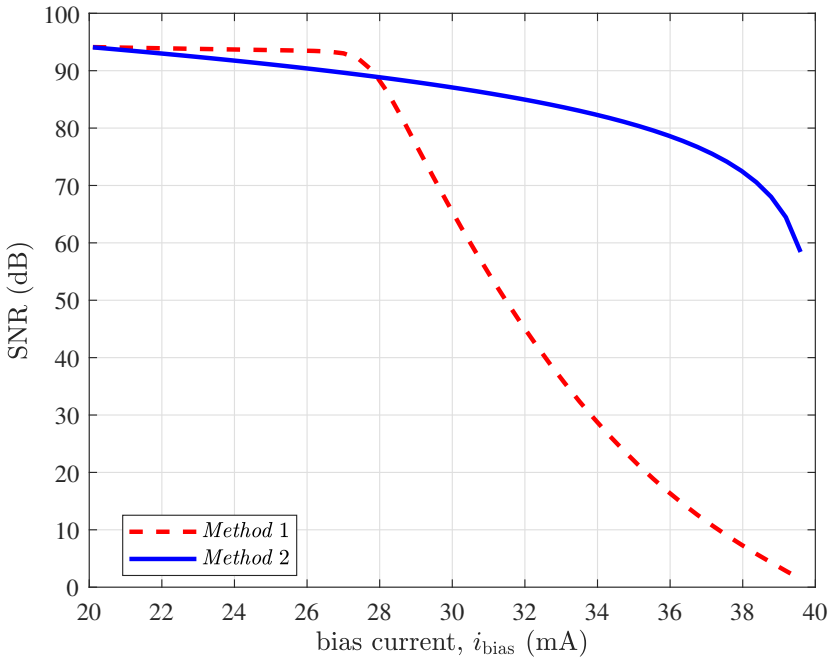

Figure 3.7: *SNR against bias current for Method 1 and Method 2*

minimal. However, as the bias current goes above 27 mA, there is a sharp decline in SNR as this is the bias current from which the impact of interference and noise gets stronger. On the contrary, the SNR in *Method* 2, is lower than in *Method* 1 only up to around 28 mA. However, there is no sharp decline as the impact is mainly from the reduction in the signal swing. Yet, there is a moderate reduction in SNR as the bias current increases due to the reduction in signal power and slight rise in noise.

The challenge in both bias optimisation method is to find the optimum bias current that maximises the modulation bandwidth which satisfies (3.13). The link capacity is linearly proportional to the modulation bandwidth while it is logarithmic proportional to SNR. The modulation bandwidth of the LED increases linearly with increasing bias current, shown in Fig. 3.5. While the SNR of both methods decreases as the bias current is decreased, shown in Fig. 3.7. Therefore, the question is whether the increase in bandwidth can compensate the reduction in SNR and results is capacity gain. The result of the capacity as the bias current is presented in Fig. 3.8. For both methods, the capacity increase until it reaches the maximum and declines. The optimum bias point, for maximum capacity with *Method* 1, is obtained at 27.4 mA. This shows that the gain from the linear increment in the electrical bandwidth is not sufficient to compensate for the distortion of signal power beyond this optimum point. Also, in *Method* 2, the capacity

increases as bias current increases until the optimum bias point is 33.7 mA. Both approaches record identical maximum capacity of about 590 Mbps for the parameters used. Note that the results in Fig. 3.8 provide the maximum achievable information rate using a Gaussian distributed signal and AWGN channel. For commonly used modulation formats, there will always be a performance gap from the maximum capacity predicted by (3.9) and (3.12). This capacity gap can be approached through probabilistic symbol shaping and channel coding [154].

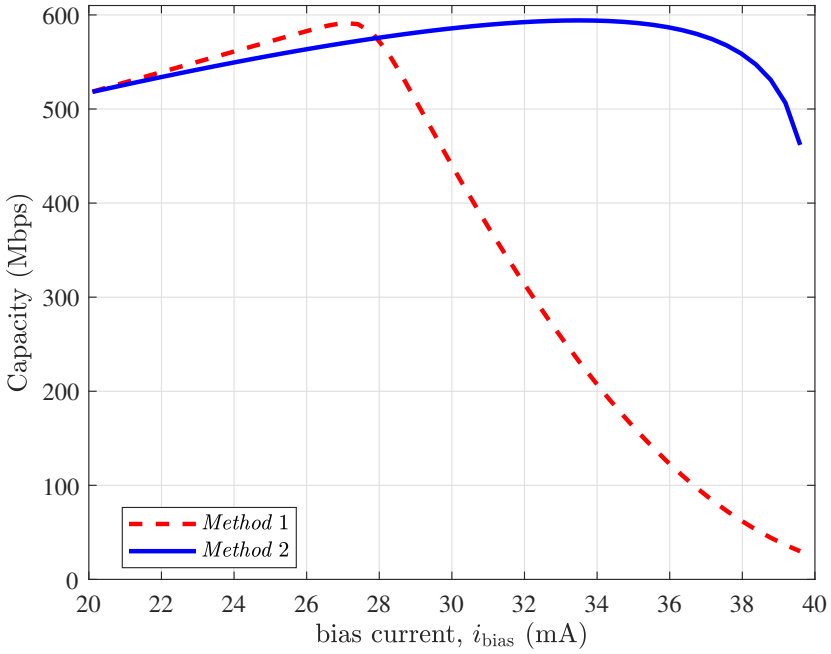

Figure 3.8: *Simulation results of capacity with different bias current for Method 1 and Method 2 using OFDM modulation scheme*

Another important aspect to compare the results of the bias optimisation methods is to evaluate the capacity per channel use which can estimate the spectral efficiency in bit/s/Hz. This result in capacity per channel use is shown in Fig. 3.9. In terms of efficient use of the available bandwidth at their respective optimum bias points, *Method* 1 is preferable with 30.6 bit/s/channel as against 27.5 bits/s/channel for *Method* 2. However, data transmission that uses *Method* 1 must be able to cope with any distortions introduced by this method or high transmission error rate will ensue.

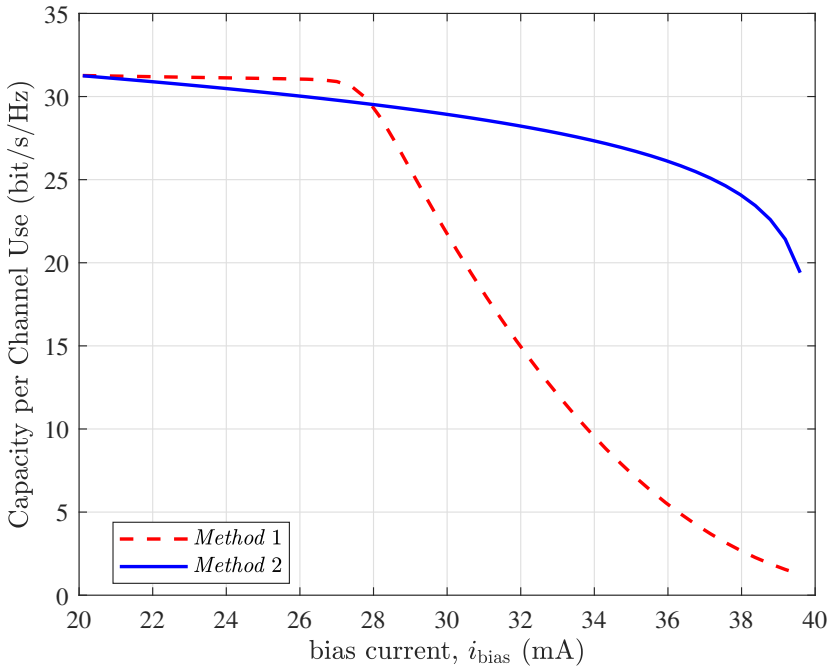

Figure 3.9: *Simulation results of capacity per channel use against bias current*

3.4 Experimental study

In this section, the experimental validation of *Method* 2 is presented. This method is preferred as it benefits more from the linear increase of modulation bandwidth as the DC bias is increased and there is no nonlinear distortion to contend with. Furthermore, for illustration purpose and simplicity, PAM-based VLC is implemented in the experiment.

3.4.1 Experiment Setup

A block diagram of the experimental setup is shown in Fig. 3.10. At the transmitter side, uniformly distributed random integers are generated and mapped into 4-PAM symbols. After up-sampling by oversampling factor of four, rectangular pulse shaping is applied to generate pulse signal. This offline signal generation is done in MATLAB. The pattern is then uploaded to an arbitrary waveform generator (AWG: Keysight 33622A) to generate the modulating signal. The sampling rate in the range of 40 MSa/s to 200 MSa/s are used in performance evaluation. The output of the AWG and the DC bias current from a DC power supply are combined using a bias-tee (Bias-Tee: Mini-Circuits ZFBT-4R2GW+). The output signal from the bias-tee is connected to the LED (VLMB1500-GS08). Since the half-power semi-angle of the LED is wide

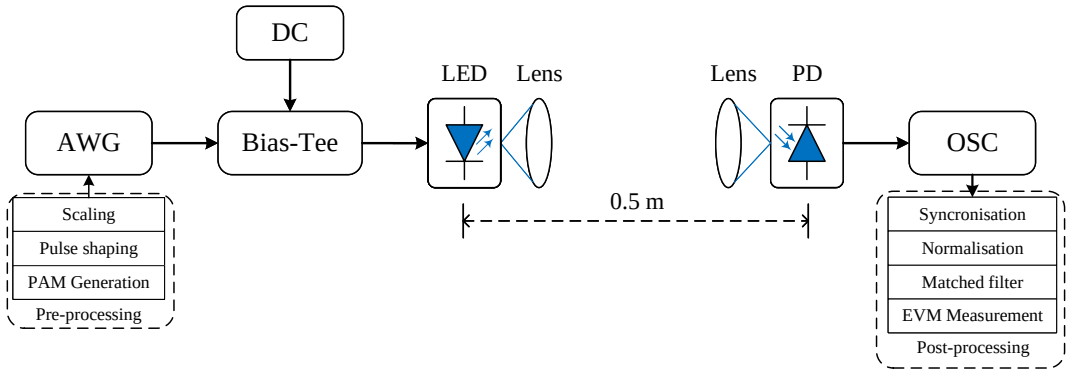

Figure 3.10: *The block diagram of the experimental setup*

(*i.e.* about 65° [153]), aspheric condenser lenses (Thorlabs ACL4532) are used to collimate the output light from the transmitter and focus it into the detection area of the photodetector.

At a receiver side with a link distance of 0.5 m, a photodetector (PD: ThorLabs PDA10A) is used to detect the intensity modulated signal. The receiver has a −3 dB bandwidth of 150 MHz and a built-in TIA with a gain of 5 V/mA. The received electrical signal is captured by an oscilloscope (OSC: Keysight MSO7104B) followed by offline processing in MATLAB. The post-processing includes alignment of received signal to transmitted, normalisation of the amplitude level, and matched filtering. For performance evaluation, the root-mean-square (RMS) error vector magnitude (EVM) is measured for different sampling rates of transmission.

3.4.2 Results and Discussions

Having determined the dynamic range of the LED as shown in Fig. 3.4 and Fig. 3.5, to validate the optimum biasing point which provides maximum capacity, five different biasing points are considered in a transmission experiment. These biasing points are all within the dynamic range of the LED. For each of these biasing points, the modulating PAM signal is scaled to fit the linear operating region of the LED. This is achieved by adjusting the peak-to-peak voltage $(V\mathrm{pp})$ output of the AWG. These values are, $V\mathrm{pp} = [540, 360, 240, 120, 40]$ mV at bias currents, $i_{\mathrm{bias}} = [20, 25, 30, 35, 38]$ mA, respectively.

To investigate the achievable transmission rate, the EVM metric at different sampling rates of the AWG are measured for all biasing points. The result is depicted in Fig. 3.11. It can be seen that the EVM increases as the transmission rate increases. Most importantly, the EVM

performance gets better when biasing current is increased from 20 mA to 30 mA and gets worse at higher biasing currents. The prediction that bandwidth will increase as bias current increases until it reaches a point of saturation is supported by this observation.

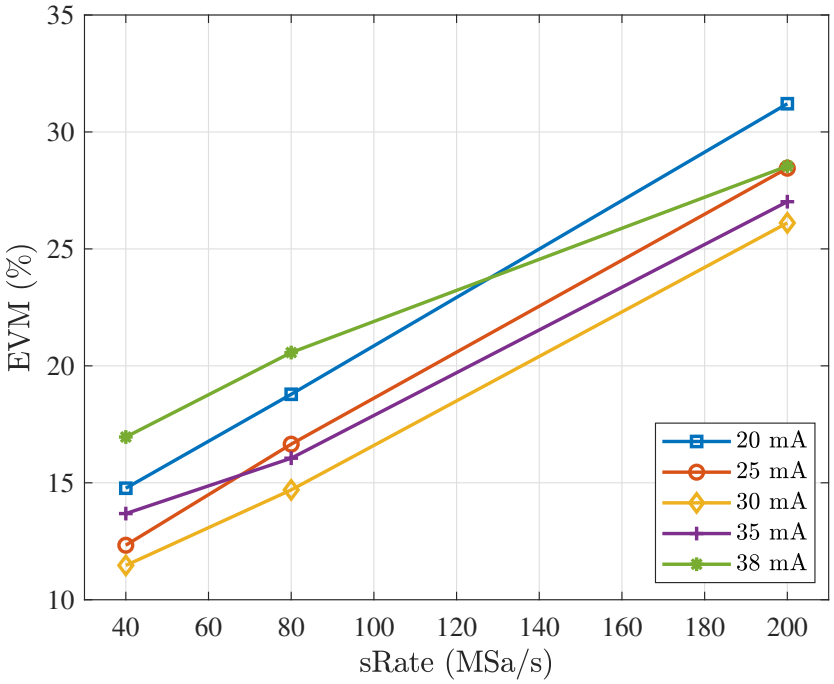

Figure 3.11: *Performance of the link in terms of EVM for different sampling rates*

The performance is further demonstrated in Fig. 3.12 by plotting the maximum attainable sampling rates at two EVM values against the bias current. In choosing these reference EVM values, the BER required to achieve the 7% hard decision forward error correction (HD-FEC) threshold of $\mathrm{BER} \leq 3.8 \times 10^{-3}$ is considered which can be achieved with 25% EVM or lower. The equivalent EVM is obtained by applying $\mathrm{EVM} = 1/\sqrt{\mathrm{SNR}}$ and the theoretical 4-PAM BER expression [155]:

$$\mathrm{BER} \approx \frac{1}{4}\left(3Q\left(\sqrt{\frac{2}{5}\mathrm{SNR}}\right) + 2Q\left(3\sqrt{\frac{2}{5}\mathrm{SNR}}\right)\right), \tag{3.14}$$

where $Q(\cdot)$ is the Gaussian Q-function. The result shows that a maximum sampling rate of 190 MSa/s, equivalent to 95 Mbit/s, is attained at 30 mA, considering a 25% EVM. This is an increase from 140 MSa/s (equivalent to 70 Mbit/s) when the LED is biased at 20 mA, in the middle of its dynamic range. Above the 30 mA bias current, the transmission rate drops. Similar trend is obtained at a lower EVM value of 20%.

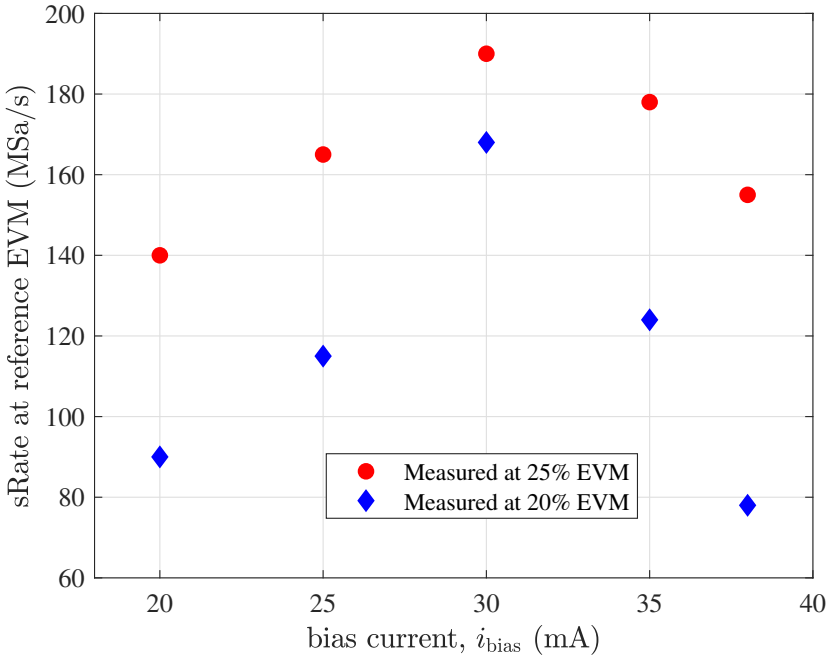

Figure 3.12: *Achieved sampling rates using 25% and 20% reference EVM at different bias current*

The bit rate per channel use (spectral efficiency in bit/s/Hz) is also shown in Fig. 3.13. This

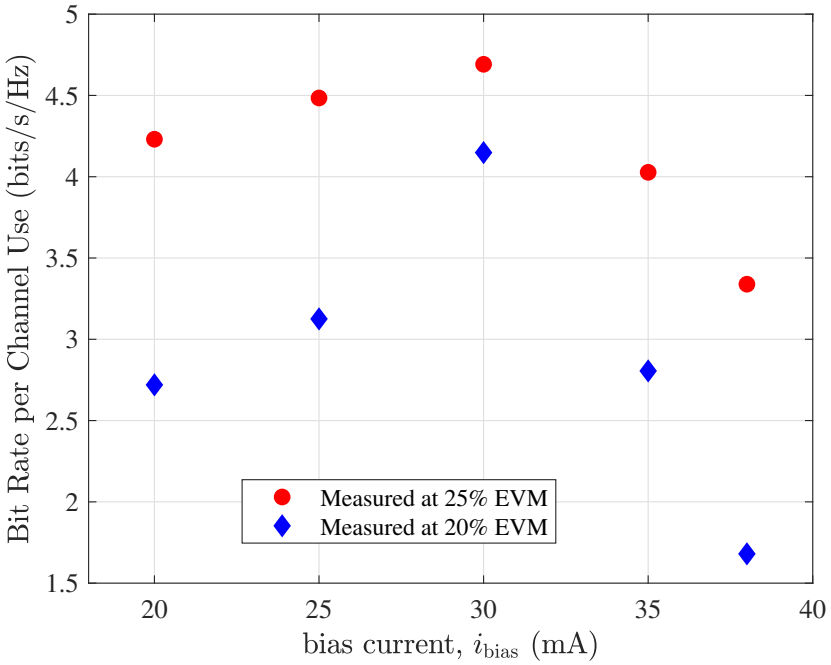

Figure 3.13: *Achieved bit rate per channel use considering 25% and 20% reference EVM at different bias current*

is obtained by evaluating the ratio between the achievable data rate at the bias current to the LED's modulation bandwidth at the same bias current. At the 25% reference EVM for the 4-PAM, 30 mA biasing provides 4.7 bit/s/channel use, higher than at other bias points. Overall, from Fig. 3.12 and Fig. 3.13, it can be seen that the optimum bias point is not in the middle of the dynamic range but at $31\ \mathrm{mA}$. This agrees quite closely with the $33.7\ \mathrm{mA}$ obtained from the simulation. This validates the simulation result of *Method* 2 bias optimisation discussed in the previous subsection. Thus, by using the optimum DC biasing and keeping the modulating signal power within the LED's dynamic range, transmission with higher rate is attained and consequently the link capacity is enhanced.

3.5 Summary

In this chapter, it has been shown that the modulation bandwidth of an LED increases as the DC bias increases from the midpoint of its linear region. The effect of this on the SNR has been examined, and two techniques for choosing the optimal DC bias point that maximises the link capacity, which is a measure of the amount of data that can be transmitted over a VLC channel, have been presented.

The first approach involves allowing the input signal swing to enter the saturation region of the LED as the bias point is increased. However, this results in nonlinear distortion that decreases the SNR. The second method involves constraining the input signal to the LED's dynamic range, which is the range of input values over which the device operates linearly, without any nonlinear distortion. Simulation results of the attainable capacity using these two methods have been presented, and it has been found that the optimal bias point does not lie at the middle of the dynamic range.

The simulation finding has been further validated through a PAM-based VLC experiment. The experimental results show that by increasing the bias current from the midpoint of the linear region (20 mA) to the optimal bias current (30 mA), the transmission rate can be increased by about 36%. Optimising the DC bias is also a valid approach to enhance the performance of an optical OFDM system, which can be combined with adaptive bit-power loading to increase the system's capacity. In such systems, the amount of information bit/symbol depends on the pre-estimated channel response in individual subcarriers, such as the channel gain and SNR. When the bias current is increased, the modulation bandwidth and channel gain also increase,

allowing more subcarriers to carry information bits. Consequently, the aggregate achievable information rate also increases. These optimisation approaches can also be combined with other techniques, such as pre/post equalisation and precoding/pre-distortion, to achieve even greater gains.

Overall, the modulation bandwidth of an LED is strongly influenced by the DC bias and choosing the optimal bias point can significantly increase the link capacity in a VLC system. By considering both the impact on the SNR, modulation bandwidth and the LED's dynamic range, it is possible to identify the optimal bias point and improve the performance of the system. These optimisation techniques can be used in combination with other approaches to further enhance the VLC system capabilities.

Chapter 4
Visible Light Communication Using Probabilistic Shaping

4.1 Introduction

The modulation bandwidth of LEDs can often be a limiting factor in achieving a high-speed VLC system. One way to overcome this limitation is to use OFDM in conjunction with adaptive information and power loading. This will allow modulation of the signal beyond the −3 dB bandwidth of the LED. In this system, the available SNR of each subcarrier in all frequency ranges is estimated, and information bits are allocated accordingly. This allows for the transmission of data at much higher rates, making LED-based communication systems more suitable for high-speed applications [40, 41, 59].

The adaptive bit-power loading approach, however, has a limitation in that it only allows for discrete integer-level bits per symbol to be allocated to each subcarrier. This does not provide the optimal fit for the VLC channel frequency response, leading to a capacity gap compared to the channel capacity limit formulated by Shannon [11]. To close this gap, the amount of information loaded should be continuously adjusted to each subcarrier based on the pre-estimated SNR. This can be achieved using PS-based optical OFDM, where different probabilistic distributions are applied to individual subcarriers based on the pre-estimated SNR. This continuous entropy loading allows for efficient use of the available bandwidth well beyond the bandwidth of LED.

In addition to improving the use of the limited modulation bandwidth of a VLC channel, PS reduces the amount of symbol energy required in transmission. This is because PS provides a Gaussian-like distribution over the signal constellation. Therefore, low-energy symbols, which have a lower standard deviation in the Gaussian-like distribution, are transmitted more frequently than high-energy symbols. This reduction in average symbol energy at a specific error rate, compared to a uniform distribution, is known as shaping gain [106]. The resulting shaping gain can be used to increase the SNR, which results in increased noise resilience and a

higher achievable information rate. This makes PS a valuable technique for improving the performance of VLC systems, particularly in high-speed applications.

In this chapter, the basic principle of PS including the generation of Gaussian-like distribution and its implementations are discussed. The performance metrics of PS in terms of symbol-wise and bit-wise information rates are formulated. In literature, the error performance of probabilistically shaped QAM symbols has not been studied. To address this gap, the symbol error rate (SER) of PS-based uncoded QAM with modulation order, M, (PS-M-QAM) under Gaussian noise-limited condition is analysed, and analytical expressions are provided. The analysis is based on an optimum maximum a-posteriori (MAP) detector derived for the probabilistic shaping scheme. The results are compared with the conventional uniformly distributed uncoded QAM symbols. The PS approach is also extended to Rayleigh and log-normal fading channel conditions and expressions to estimate the PS performance in the presence of fading are derived. The presented analysis is based on symbol error rate and therefore agnostic of the choice of bits-to-symbol distribution matcher. As a proof-of-concept implementation, PS is applied in conjunction with OFDM modulation to load information bits continuously and adaptively fit the channel response. PS provides efficient use of the available modulation bandwidth and transmission rates close to the channel capacity limits are demonstrated. In the first experimental demonstration, a single low-power LED is used to achieve beyond 1 Gbps. In the second experimental demonstration, a WDM-based VLC which used three (red, green, and blue) off-the-shelf LEDs is employed to realise nearly 11 Gbps transmission.

The chapter is arranged in the following way. Section 4.2 covers the principle of probabilistic shaping, which involves generating a Gaussian-like distribution of signal. The error performance of probabilistic shaping is analysed in both AWGN in Section 4.3 and fading channels, including log-normal fading and Rayleigh fading channels, in Section 4.4. The performance metrics of PS in terms of the symbol-wise and bit-wise achievable information rates are discussed in Section 4.5. Following these, the principle of entropy loading using PS for optical OFDM is presented in Section 4.6. These metrics will be used to measure the performance of experimental demonstrations of probabilistic shaping in single LED-based and WDM-based high-speed VLC systems presented in Section 4.7. Finally, Section 4.8 provides concluding remarks of the chapter.

4.2 The Principle of Probabilistic Shaping

According to Shannon's theory in [11], the information rate of an AWGN channel, which is a type of communication channel characterised by the presence of Gaussian noise, is limited by a theoretical upper bound given by (2.11). This upper bound can be achieved when the channel is fed by a transmitter source with a Gaussian distribution. In other words, if the input symbols at the transmitter are chosen from a Gaussian distribution, it is possible to achieve the highest possible information rate in the AWGN channel, given a certain power constraint. Probabilistic shaping is a technique that involves using a probability distribution, in this case, a Gaussian distribution. Input symbols are selected from the Gaussian distribution in order to maximise the information rate and approach the theoretical upper bound of the channel capacity. A Gaussian distribution, however, is characterised by continuous symbols with infinite amplitudes. In practical communication aspects, this leads to a high peak-to-average power ratio (PAPR) and it is impossible to implement due to limitations in digital-to-analogue and analogue-to-digital converters [104]. Therefore, symbols should be represented in a discrete and finite level of amplitudes to approximate the Gaussian distribution. The common distribution which gives such a Gaussian-like distribution is the Maxwell-Boltzmann distribution [106]. It has been shown that the Maxwell-Boltzmann distribution can maximise the entropy and the ultimate 1.53 dB shaping gain can be achieved [106, 110, 118].

For probabilistic shaped M-PAM (PS-M-PAM), given M-PAM symbols which are chosen independently from a set, $x_m = \{2m - 1 - M\}, m = 1, 2, \cdots, M$, the PMF of a constellation point x_m can be generated from the Maxwell-Boltzmann distribution given in (2.21). This can be rewritten as:

$$P_X(x_m) = \frac{1}{\sum_{j=1}^{M} \mathrm{e}^{-\lambda |x_j|^2}} \mathrm{e}^{-\lambda |x_m|^2}, \tag{4.1}$$

with $\lambda \geq 0$, which is a rate parameter used to search for the optimum PMF depending on the choice of entropy and average symbol energy. For $\lambda = 0$, (4.1) reduces to the uniform distribution with, $P_X = 1/M$, and as λ increases, the constellation distribution becomes Gaussian with reduced variance. A graphical illustration of PS-8-PAM with different rate parameter, λ is shown in Fig. 4.1. As λ reduces from 0.0902 in (a) to 0.0408 in (c), the probability of the outer signal amplitude being generated increases. And when $\lambda = 0$, the distribution becomes uniform with a probability of 1/8.

A distribution matcher transforms uniformly distributed input information bits to Maxwell-

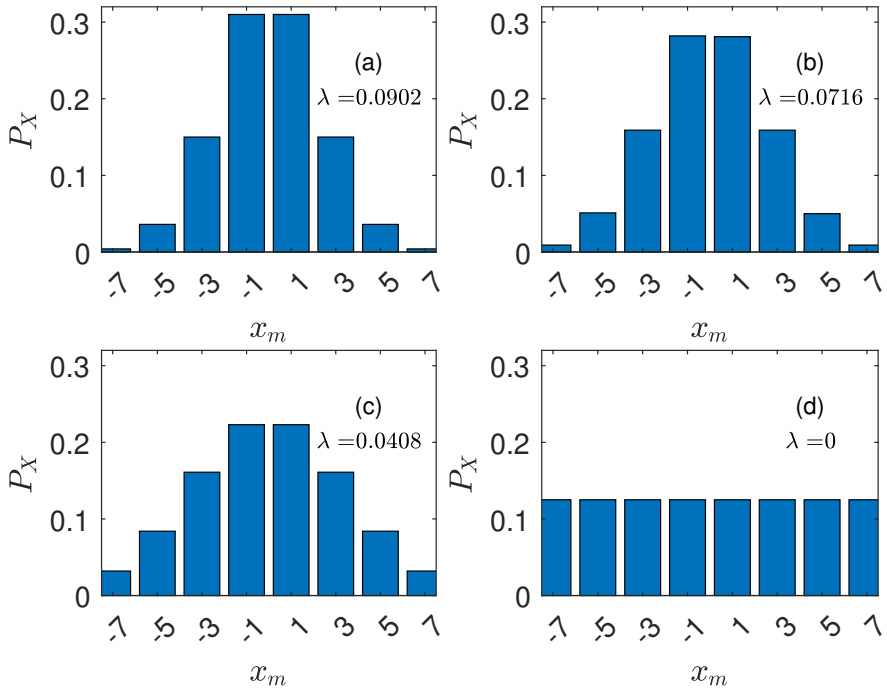

Figure 4.1: *Graphical illustration of PS-8-PAM using various parameters, λ. When $\lambda = 0$, the distribution becomes uniform.*

Boltzmann-distributed PAM output symbols. A CCDM, proposed in [115], provides a fixed length and invertible encoders and decoders. For a given rate parameter and modulation order M, the CCDM creates a distribution such that a symbol x_m appears n_m times in each fixed total length of CCDM blocks n_s. Therefore, this will create a PMF, $P_X = \left[\frac{n_1}{n_s}, \cdots, \frac{n_M}{n_s}\right]$.

The entropy of the system, which quantifies the unpredictability of information content, can be determined from (4.1) as:

$$H = \mathbb{E}\left[-\log_2\left(P_X\left(x_m\right)\right)\right] = -\sum_{m=1}^{M} P_X\left(x_m\right)\log_2\left(P_X\left(x_m\right)\right), \tag{4.2}$$

where $\mathbb{E}\left[\cdot\right]$ denotes expectation operation. Meanwhile, the average symbol energy can be evaluated as:

$$\xi_{\text{av}} = \sum_{m=1}^{M} \left|x_m\right|^2 P_X\left(x_m\right). \tag{4.3}$$

For unifrom distribution, the entropy in (4.2) reduces to:

$$H_{\text{u}} = \sum_{m=1}^{M} \frac{1}{M}\log_2 M = \log_2 M, \tag{4.4}$$

and the average symbol energy in (4.3) to:

$$\xi_{\text{av, u}} = \sum_{m=1}^{M} \frac{1}{M} (2m - 1 - M)^2 = \frac{1}{3} \left(M^2 - 1\right). \tag{4.5}$$

Note that, the H in PS is less than uniform distribution for the same M. Also, as λ increases, shaped symbols results in fractional numbers of bit/symbol such that $1 \leq H_{\text{ps}} < \log_2 M$. The fraction nature of entropy is important to realise adaptive and continuous entropy allocation.

The shaping gain, G which quantifies the reduction in average symbol energy in PS compared to a uniform distribution symbol can be evaluated by:

$$G = \frac{\xi_{\text{av, u}}}{\xi_{\text{av, ps}}}, \tag{4.6}$$

provided that the entropy of PS , $H_{\text{ps}} = H_{\text{u}} = \log_2 M$. Therefore, one needs to numerically determine λ which satisfies the equal entropy and use this λ to evaluate the average symbol energy of PS symbols, $\xi_{\text{av, ps}}$. Since PS has lower H at the same modulation order, M, higher orders, (*i.e.*, $2M$) should be used while it is M for uniform distribution. Figure 4.2 shows the shaping gain for increasing entropy values relative to the ultimate shaping gain, $\pi\text{e}/6 \approx 1.5329$ dB. The gain increases with entropy until it approaches the ultimate gain asymptotically, as shown in the inset figure. A key factor in the implementation of PS is finding the optimal PMF. As can be seen from Fig. 4.2, larger shaping gain can be found at higher entropy values. Therefore, to maximise the PS gain, a rate parameter which increases the entropy rate should be used. For that, the channel SNR response must be known or estimated a priori. More discussion will be made in Section 4.6 as part of the experimental study that demonstrates PS achieving near channel capacity transmission rate.

The constellation of a square M-QAM can be considered as two orthogonal $\sqrt{M}-$PAM constellations. This means every QAM symbol can be considered as two consecutive PAM symbols that represent real and imaginary parts of the QAM symbol. The PMF of an M-QAM constellation is, therefore, the product of the respective constituent PAM probabilities, while the entropy is twice the 1-dimensional entropy. Figure 4.3 shows graphical illustration of 64-QAM signal with four different entropy scenarios generated using the one-dimensional 8-PAM signal PMF shown in Fig. 4.1. In this work, most of the analyses are carried out with 2-dimensional QAM signals. For ease of analysis and graphical representation, some analysis are implemented using 1-dimensional PAM signal and extended to QAM cases. In this case, it will be stated explicitly.

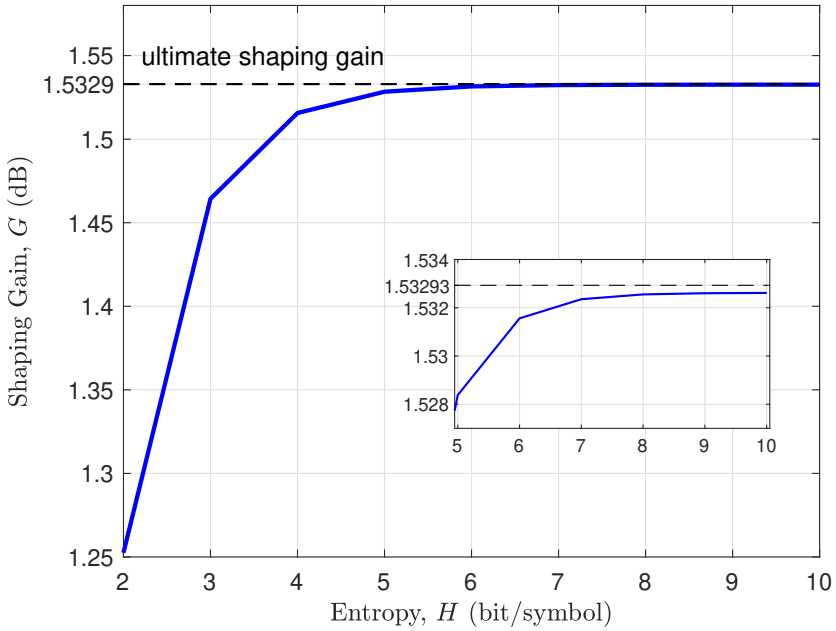

Figure 4.2: *Shaping gain for different entropy values. The inset figure shows how the shaping gain approaches the ultimate gain. Dashed black lines show the ultimate shaping gain.*

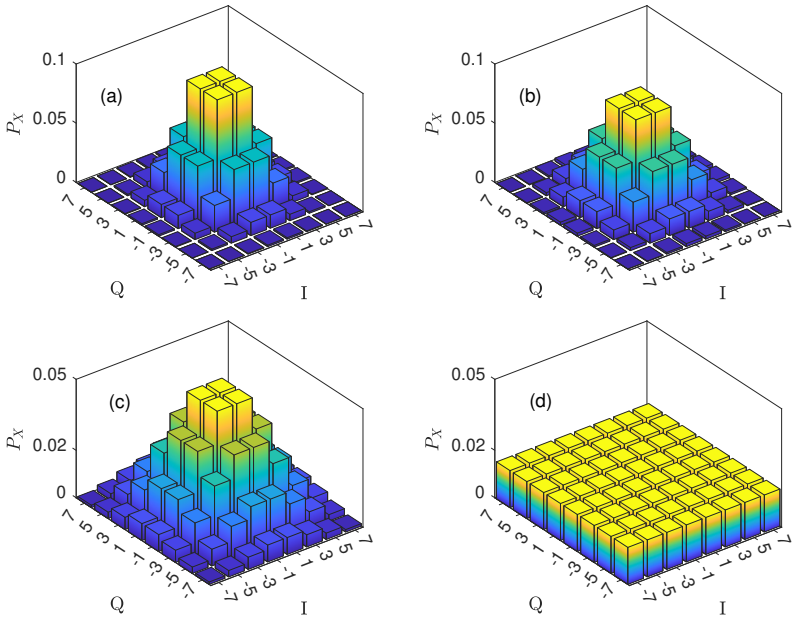

Figure 4.3: *Graphical illustration for probabilistic shaped 64-QAM with four different entropy values showing (a) H = 4.5 bit/symbol, (b) H = 4.80 bit/symbol, (c) H = 5.40 bit/symbol, (d) H = 6.00 bit/symbol (uniform distribution)*

4.3 Error Performance Analysis of PS in AWGN Channel

In this section, the theoretical error performance of PS is presented. The analysis is based on symbol error rate and therefore agnostic of the choice of bits-to-symbol distribution matcher. The SER of PS-based uncoded QAM with modulation order, M, (PS-M-QAM) under Gaussian noise-limited condition is analysed, and analytical expressions are provided. The results are compared with the conventional uniformly distributed uncoded QAM symbols.

The optimum detection scheme for PS is based on the MAP detector. This is because the detection needs to take the priori symbol distribution into account, unlike the maximum likelihood detector that does not [156]. In the following, the analysis is based on a 1-dimensional PAM signal and it is easily extended to a 2-dimensional QAM signal.

Consider an AWGN channel such that the received symbols over a symbol duration are defined as $Y = X + Z$, where X is the transmitted input PAM symbols and Z is an independent and identically distributed noise vector with Gaussian random variable $\mathcal{N}(\mu = 0, \sigma_n^2)$. The input symbols, X take values from $\{x_1, x_2, \cdots, x_m\}$ according to the priori PMF given by (4.1). Given the the transmitted symbols X, the memoryless and two-dimensional circularly symmetric channel conditional probability density is given by [156]:

$$P_{Y|X}\left(y|x_m\right) = \frac{1}{\sqrt{2\pi\sigma_n^2}} \exp\left(-\frac{|y - x_m|^2}{2\sigma_n^2}\right), \tag{4.7}$$

where $\sigma_n^2 = N_0/2$ is the noise variance of the channel, and N_0 denoting the single-sided noise power spectral density. The posterior distribution, $P_{X|Y}\left(x_m|y\right)$ can be used to estimate the unknown transmitted symbol given the channel conditional probability distribution in (4.7) and the marginal received symbols distribution, $P_Y\left(y\right)$. Based on the Baye's theorem, this can be expressed as follows [157]:

$$P_{X|Y}\left(x|y\right) = \frac{P_X\left(x_m\right)}{P_Y\left(y\right)} P_{Y|X}\left(y|x_m\right). \tag{4.8}$$

The marginal distribution, $P_Y\left(y\right)$ is independent of the value transmitted and it is the same for all symbols. Therefore, (4.8) can be further simplified to:

$$P_{X|Y}\left(x_m|y\right) = P_X\left(x_m\right) P_{Y|X}\left(y|x_m\right). \tag{4.9}$$

The MAP detector is thus based on maximising the argument of $P_{X|Y}\left(x_m|y\right)$ in (4.9), which

can be written as [156]:

$$\hat{m} \mapsto \underset{1\leq m\leq M}{\arg\max}\, P_{X|Y}\left(x_m|y\right) = \underset{1\leq m\leq M}{\arg\max}\left[P_X\left(x_m\right) P_{Y|X}\left(y|x_m\right)\right]. \tag{4.10}$$

In the following, the optimum symbol, $\hat{m}$ is simplified substituting (4.1) and (4.7) in (4.10):

$$\hat{m} = \underset{1\leq m\leq M}{\arg\max}\left[\frac{1}{\sum_{j=1}^{M}\mathrm{e}^{-\lambda|x_j|^2}}\mathrm{e}^{-\lambda|x_m|^2}\frac{1}{\sqrt{\pi N_0}}\mathrm{e}^{-\frac{|y-x_m|^2}{N_0}}\right] \tag{4.11a}$$

$$\overset{(a)}{=} \underset{1\leq m\leq M}{\arg\max}\left[\mathrm{e}^{-\lambda|x_m|^2}\mathrm{e}^{-\frac{|y-x_m|^2}{N_0}}\right] \tag{4.11b}$$

$$\overset{(b)}{=} \underset{1\leq m\leq M}{\arg\max}\left[\ln\left(\mathrm{e}^{-\lambda|x_m|^2}\mathrm{e}^{-\frac{|y-x_m|^2}{N_0}}\right)\right] \tag{4.11c}$$

$$= \underset{1\leq m\leq M}{\arg\max}\left[-\lambda\left|x_m\right|^2 - \frac{|y-x_m|^2}{N_0}\right] \tag{4.11d}$$

$$\overset{(c)}{=} \underset{1\leq m\leq M}{\arg\max}\left[-\frac{N_0}{2}\lambda\left|x_m\right|^2 - \frac{1}{2}|y-x_m|^2\right] \tag{4.11e}$$

$$= \underset{1\leq m\leq M}{\arg\max}\left[-\frac{N_0}{2}\lambda\left|x_m\right|^2 - \frac{1}{2}\left(|y|^2 + |x_m|^2 - 2yx_m\right)\right] \tag{4.11f}$$

$$\overset{(d)}{=} \underset{1\leq m\leq M}{\arg\max}\left[yx_m - \frac{1}{2}\left(1+N_0\lambda\right)|x_m|^2\right]. \tag{4.11g}$$

In the above simplification, the following assumptions are carried out; (a): positive constants does not change the value and hence are dropped, (b): $\ln(\cdot)$ is an increasing function, (c): $N_0/2$ is a positive number and multiplying by a positive number does not affect the result, (d): $|y|^2$ is the same for all m and hence it is dropped. Note that for uniform distribution in which, $\lambda = 0$ and $P_X\left(x_m\right) = 1/M$, reduces to the maximum likelihood detector with, $\hat{m} = \underset{1\leq m\leq M}{\arg\max}\, P_{Y|X}\left(y|x_m\right) = \underset{1\leq m\leq M}{\arg\max}\left(-|y-x_m|^2\right) = \underset{1\leq m\leq M}{\arg\min}\left(|y-x_m|\right)$. From (4.11g), it is possible to determined the decision region, D_m for all m and $1 \leq m' \leq M$ where $m' \neq m$ as:

$$D_m = \left\{y \in \mathbb{R} : y\left(x_m - x_{m'}\right) > \frac{1}{2}\left(1+N_0\lambda\right)\left(|x_m|^2 - |x_{m'}|^2\right)\right\}. \tag{4.12}$$

Note that from (4.12), there are at most $M-1$ threshold points, r_{th} where $D_m = D_{m+1}$.

The symbol error probability of the detection scheme is determined by accumulating the product of the priori distribution and the probability of error that occurs when the received symbol

is not in the D_m given x_m is transmitted. This can be written as:

$$P_{\mathrm{s}} = \sum_{m=1}^{M} p_X\left(x_m\right) \sum_{\substack{1 \leq m' \leq M \\ m' \neq m}} \int_{D_{m'}} p_{Y|X}\left(y|x_m\right) \mathrm{d}y. \tag{4.13}$$

4.3.1 Symbol Error Probability of PS-PAM

In this section, the error probability 4-PAM is derived. Using this as an example, a general SER of M-PAM is derived which is then used to derive the SER of M-QAM.

The signalling diagram of 4-PAM with amplitude levels of $x_m = \{\pm 1, \pm 3\}\sqrt{E_{\mathrm{s}}/\xi_{\mathrm{av}}}$ is shown in Fig. 4.4. Here, E_{s} is the symbol energy while ξ_{av} is the average symbol energy.

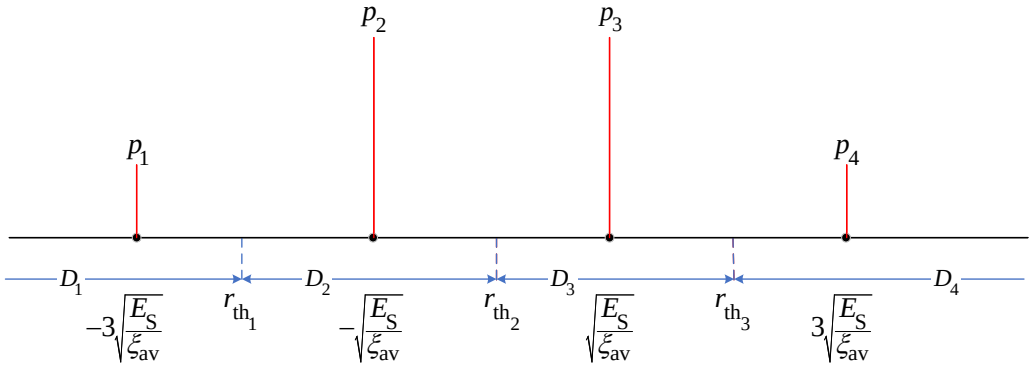

Figure 4.4: *PS-4-PAM with symmetrical PMF, decision boundaries and thresholds*

For the 4-PAM scheme, the decision boundaries are determined using (4.12) as:

$$D_1 = \left\{ y \in \mathbb{R} : y < -2\left(1 + N_0\lambda\right)\sqrt{\frac{E_{\mathrm{s}}}{\xi_{\mathrm{av}}}} \right\}, \tag{4.14a}$$

$$D_2 = \left\{ y \in \mathbb{R} : -2\left(1 + N_0\lambda\right)\sqrt{\frac{E_{\mathrm{s}}}{\xi_{\mathrm{av}}}} < y < 0 \right\}, \tag{4.14b}$$

$$D_3 = \left\{ y \in \mathbb{R} : 0 < y < 2\left(1 + N_0\lambda\right)\sqrt{\frac{E_{\mathrm{s}}}{\xi_{\mathrm{av}}}} \right\}, \tag{4.14c}$$

$$D_4 = \left\{ y \in \mathbb{R} : y > 2\left(1 + N_0\lambda\right)\sqrt{\frac{E_{\mathrm{s}}}{\xi_{\mathrm{av}}}} \right\}. \tag{4.14d}$$

Thus, the decision thresholds where $D_m = D_{m+1}$ are:

$$r_{\text{th}_1} = -2\left(1 + N_0\lambda\right)\sqrt{\frac{E_\text{s}}{\xi_\text{av}}}, \tag{4.15a}$$

$$r_{\text{th}_2} = 0, \tag{4.15b}$$

$$r_{\text{th}_3} = 2\left(1 + N_0\lambda\right)\sqrt{\frac{E_\text{s}}{\xi_\text{av}}}. \tag{4.15c}$$

Generally, the threshold points of M-PAM can be induced as:

$$r_{\text{th}_m} = \left(2m - M\right)\left(1 + N_0\lambda\right)\sqrt{\frac{E_\text{s}}{\xi_\text{av}}}. \tag{4.16}$$

Note that unlike the uniform distribution symbols, the MAP threshold points depend on the noise level and the shaping rate parameter, λ. This is further illustrated in Fig. 4.5 considering a normalised third threshold point, $\overline{r}_{\text{th}_3} = r_{\text{th}_3}/\sqrt{E_\text{s}/\xi_\text{av}}$ at different SNR per symbol (E_s/N_0) conditions. For equiprobable symbols where $\lambda = 0$, $\overline{r}_{\text{th}_3} = 2$. As λ increases, the threshold point increases and moves to the outer constellation point. The increase is higher in noisy channel ($E_\text{s}/N_0 = 10$ dB) compared to a channel with less noise ($E_\text{s}/N_0 = 16$ dB).

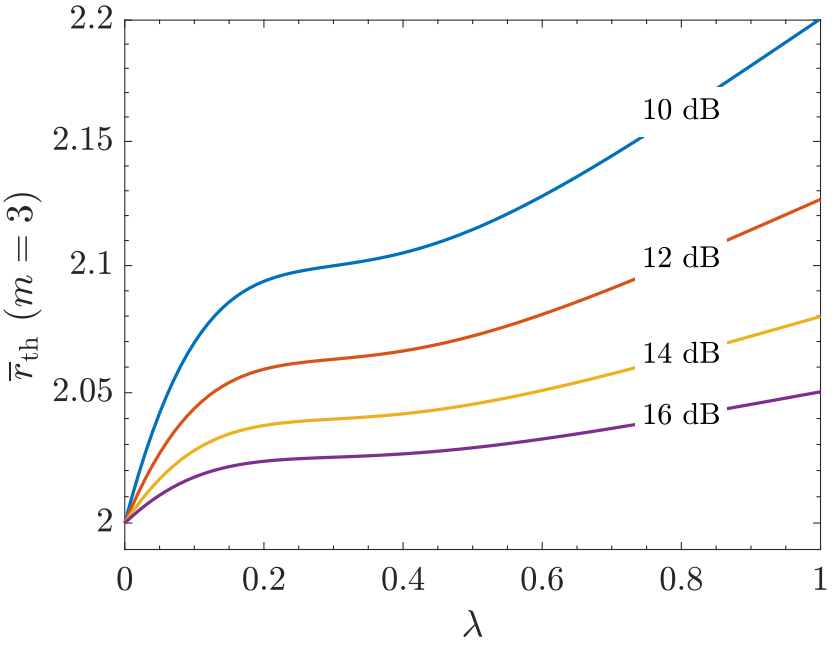

Figure 4.5: *The effect of rate parameter, λ and SNR per symbol (E_s/N_0) on the normalised third decision point, $\overline{r}_{\text{th}_3}$ of PS-4-PAM*

Taking advantage of the symmetry in amplitude and using (4.13), the error probability can therefore be evaluated as:

$$P_{\mathrm{s}} = 2p_1 \int_{r_{\mathrm{th}_1}}^{\infty} p\left(y|x=-3\sqrt{\frac{E_{\mathrm{s}}}{\xi_{\mathrm{av}}}}\right)\mathrm{d}y + 2p_2 \int_{-\infty}^{r_{\mathrm{th}_1}} p\left(y|x=-\sqrt{\frac{E_{\mathrm{s}}}{\xi_{\mathrm{av}}}}\right)\mathrm{d}y + 2p_2 \int_{r_{\mathrm{th}_2}}^{\infty} p\left(y|x=-\sqrt{\frac{E_{\mathrm{s}}}{\xi_{\mathrm{av}}}}\right)\mathrm{d}y \tag{4.17a}$$

$$= 2p_1 Q\left(\frac{r_{\mathrm{th}_1}+3\sqrt{\frac{E_{\mathrm{s}}}{\xi_{\mathrm{av}}}}}{\sqrt{\frac{N_0}{2}}}\right) + 2p_2 Q\left(\frac{-r_{\mathrm{th}_1}-\sqrt{\frac{E_{\mathrm{s}}}{\xi_{\mathrm{av}}}}}{\sqrt{\frac{N_0}{2}}}\right) + 2p_2 Q\left(\frac{r_{\mathrm{th}_2}+\sqrt{\frac{E_{\mathrm{s}}}{\xi_{\mathrm{av}}}}}{\sqrt{\frac{N_0}{2}}}\right) \tag{4.17b}$$

$$= 2p_1 Q\left(\left(1-2N_0\lambda\right)\sqrt{\frac{2}{\xi_{\mathrm{av}}}\frac{E_{\mathrm{s}}}{N_0}}\right) + 2p_2 Q\left(\left(1+2N_0\lambda\right)\sqrt{\frac{2}{\xi_{\mathrm{av}}}\frac{E_{\mathrm{s}}}{N_0}}\right) + 2p_2 Q\left(\sqrt{\frac{2}{\xi_{\mathrm{av}}}\frac{E_{\mathrm{s}}}{N_0}}\right). \tag{4.17c}$$

Using the fact that $p_2 = p_3$, as shown in Fig. 4.4, and $\epsilon \triangleq 1/\xi_{\mathrm{av}}$, (4.17c) can be further simplified to:

$$P_{\mathrm{s}} = 2\sum_{m=1}^{3} p_m Q\left(\left(1+\left(2m-4\right)N_0\lambda\right)\sqrt{2\epsilon\frac{E_{\mathrm{s}}}{N_0}}\right). \tag{4.18}$$

This provides the error probability of PS-4-PAM as a function of rate parameter, and SNR.

From the decision boundary expressions in (4.14), (4.16), and the SER of 4-PAM in (4.18), regular patterns can be drawn for general M-PAM signal. This general form of symbol error performance of PS-M-PAM is given as:

$$P_{\mathrm{s}} = 2\sum_{m=1}^{M-1} p_m Q\left(\left(1+\left(2m-M\right)N_0\lambda\right)\sqrt{2\epsilon\frac{E_{\mathrm{s}}}{N_0}}\right). \tag{4.19}$$

Note that for equiprobable symbols, $\lambda = 0$ and $p_m = 1/M$ for all m and (4.19) reduces to the error probability of a conventional uniform M-PAM.

To illustrate the impact of λ on SER given in (4.19), the SER of PS-16-PAM is shown in Fig. 4.6 for different λ values. The PS-16-PAM symbols are generated with entropy rates, H = {3, 3.2, 3.6, 3.92} bit/symbol using λ = {0.0331, 0.0250, 0.0132, 0.0047}. The SER of uniform 16-PAM (H = 4 bit/symbol) is also shown for comparison. The result shows that PS achieves better energy efficiency and the gain increases as the λ increases. However, it comes

at the cost of reduced net information rate: as λ increases, H decreases. Thus, to maximise the PS gain with optimum entropy level, the knowledge of the channel SNR response of the system is required, from which optimum PMF and thus the entropy is determined by the choice of optimum λ. This optimisation process is realised by minimising the gap between the entropy of symbols to the pre-estimated channel capacity. This will be discussed further in an experimental study that demonstrates how PS achieves near channel capacity transmission in Section 4.6.

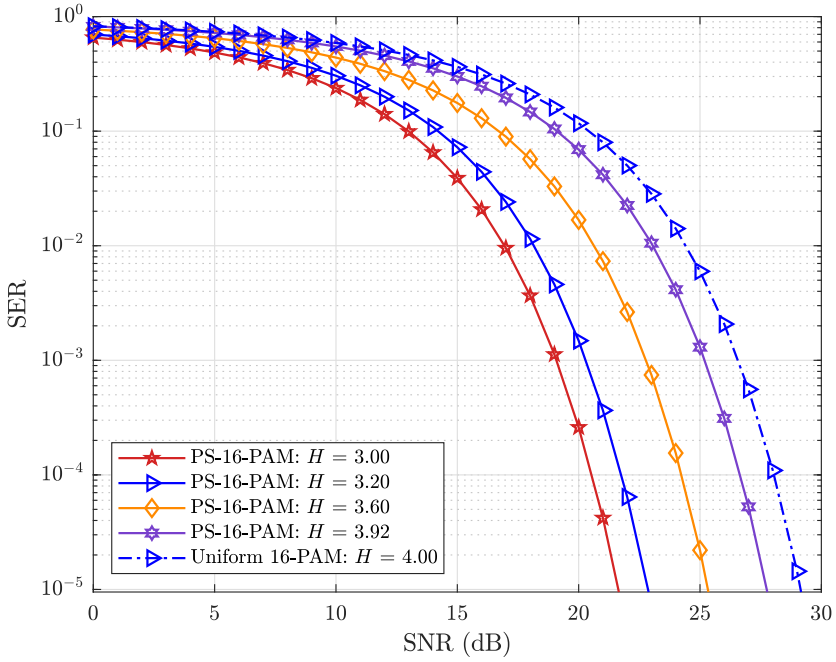

Figure 4.6: *Error performance of PS-16-PAM at different entropy levels and uniform 16-PAM*

To evaluate the PS error performance independent of a choice of rate parameter, comparison at equal net entropy rates is crucial. Therefore, the SER performance at equal net entropy rates, by using PS-M-PAM symbols against uniform symbols of lower order, is carried out and shown in Fig. 4.7. The results are also validated with Monte Carlo simulations. Here, H = 2 bit/symbol (PS-8-PAM and uniform 4-PAM), H = 3 bit/symbol (PS-16-PAM and uniform 8-PAM), and H = 4 bit/symbol (PS-32-PAM and uniform 16-PAM) are considered. In all cases, PS has better SER performance than the uniform signal with 1.13 dB, 1.37 dB, 1.43 dB SNR gains at SER = 10^{-3} for $H = \{2,\ 3,\ 4\}$ bit/symbol, respectively. This validates that the SNR gain is not necessarily associated with the entropy reduction. In fact, at equal entropy rates, PS approaches the ultimate 1.53 dB shaping gain. Higher SNR gain can be obtained by using PS-QAM which uses two orthogonal PS-PAM constellations. This will be discussed in the following subsection.

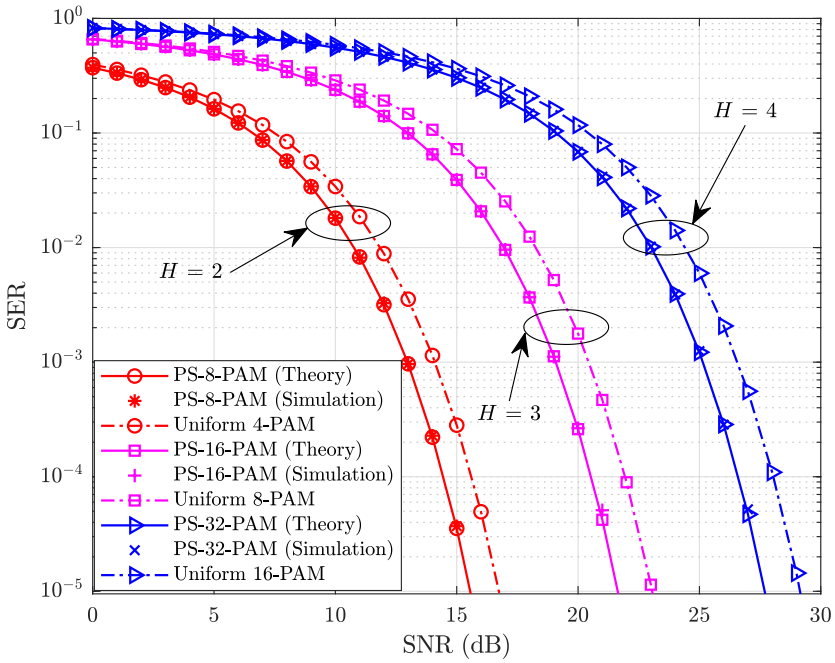

Figure 4.7: *Error performance of PS and uniformly distributed PAM for different modulation orders at equal net entropy rates under AWGN channel condition*

4.3.2 Symbol Error Probability of PS-QAM

The error probability of M-QAM can be determined from the error probability of $\sqrt{M}$-PAM with half the total energy as [156]:

$$P_{\mathrm{s}|M-\mathrm{QAM}} = 1 - \left[1 - P_{\mathrm{s}\left|\substack{\sqrt{M}-\mathrm{PAM} \\ E_{\mathrm{s}/2}}\right.}\right]^2. \tag{4.20}$$

Using (4.20) and the half energy form SER of PS-M-PAM given by (4.19), the SER of PS-M-QAM is obtained as:

$$P_{\mathrm{s}} = 4\sum_{m=1}^{\sqrt{M}-1} p_m Q\left(\sqrt{\Omega_m \frac{E_{\mathrm{s}}}{N_0}}\right) - 4\left[\sum_{m=1}^{\sqrt{M}-1} p_m Q\left(\sqrt{\Omega_m \frac{E_{\mathrm{s}}}{N_0}}\right)\right]^2, \tag{4.21}$$

where,

$$\Omega_m = \left(1 + \left(2m - \sqrt{M}\right) N_0 \lambda\right)^2 \epsilon. \tag{4.22}$$

For PS-4-QAM, all constellation points are in an equal constellation ring with same probabilities. Hence, $\lambda = 0$, $\epsilon = 1$, and $\Omega_m = 1$. Consequently, (4.21) reduces to:

$$P_{\mathrm{s}} = 2Q\left(\sqrt{\frac{E_{\mathrm{s}}}{N_0}}\right) - Q^2\left(\sqrt{\frac{E_{\mathrm{s}}}{N_0}}\right), \tag{4.23}$$

which is the same as the symbol error probability of uniformly distributed 4-QAM.

The SER of PS-QAM given by (4.21) corroborated with Monte Carlo simulation is shown in Fig. 4.8. For comparison, the SER of the conventional uniformly distributed QAM is also included. In this illustration, PS-M-QAM symbols with M = {16, 64, 256} are generated with entropy, H = {3.6, 5.4, 7.2} bit/symbol using rate parameter, λ = {0.1353, 0.0408, 0.0119}, respectively. The entropy of PS-M-QAM is thus set to be $0.9 \times \log_2 M$ of the uniform counterparts. The performance improvement from PS over the uniformly distributed symbols is evident from the result. For all modulation orders shown and ranges of SNR, the PS outper-

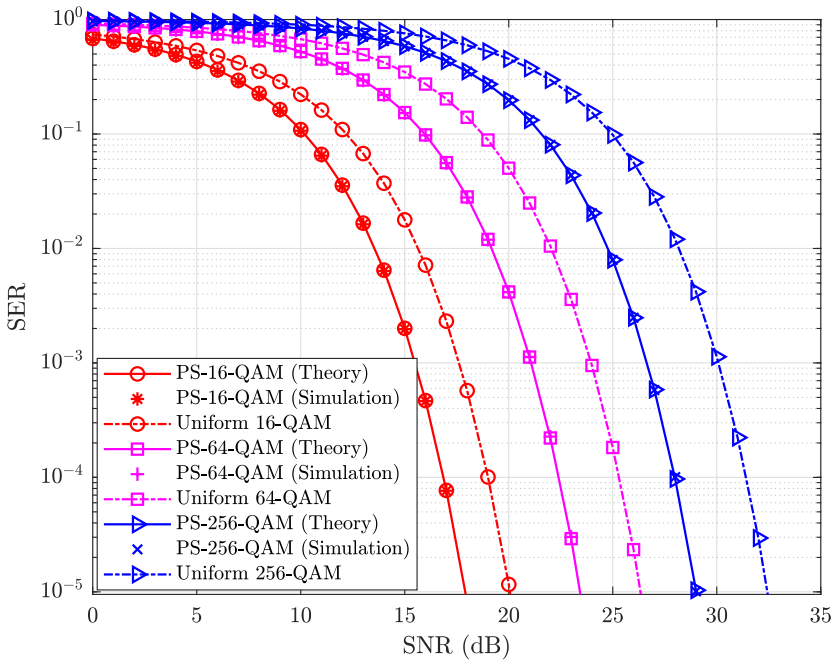

Figure 4.8: *Error performance of PS and uniformly distributed QAM for different modulation orders under AWGN channel condition*

forms uniform distribution. For instance, at SER $= 10^{-3}$, about 2.12 dB, 2.89 dB, 3.45 dB SNR improvement is obtained from PS-16-QAM, PS-64-QAM, and PS-256-QAM over the corresponding uniform QAM symbols, respectively.

The SER performance comparison is also repeated at equal net entropy rates by using PS-M-QAM symbols against uniform symbols of lower order ($M/4$-QAM) and the result is presented in Fig. 4.9. Entropy rates, H = 4 bit/symbol (PS-64-QAM and uniform 16-QAM), H = 6 bit/symbol (PS-256-QAM and uniform 64-QAM), and H = 8 bit/symbol (PS-1024-QAM and uniform 256-QAM) are considered. In all cases, PS has better SER performance than the uniform signal with SNR gains of 1.16 dB, 1.41 dB, and 1.52 dB for $H = \{4, 6, 8\}$ bit/symbol, respectively, at SER = 10^{-3}. These shaping gains are higher than PS-PAM and achieve the ultimate shaping gain.

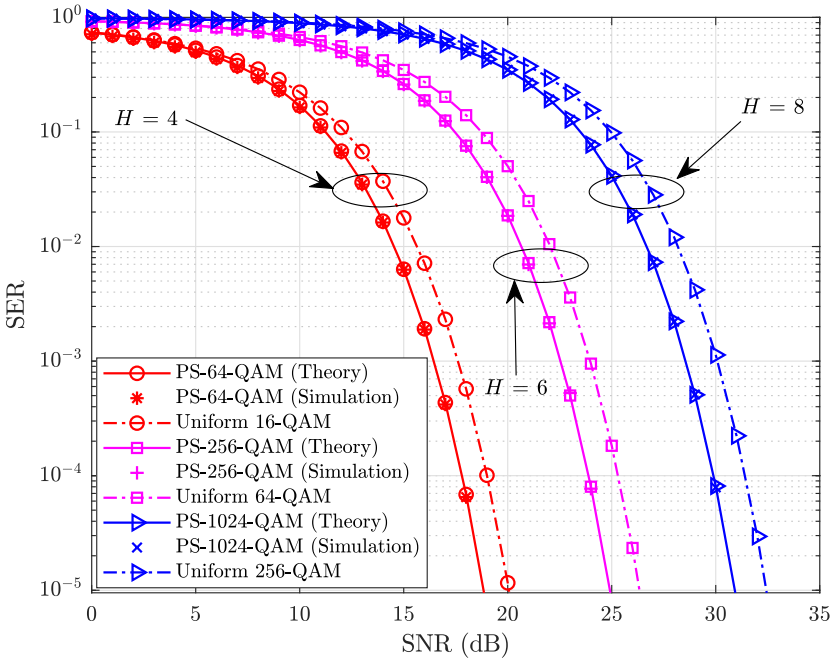

Figure 4.9: *Error performance of PS and uniformly distributed* QAM at the same net entropy values

4.4 Error Performance in Fading Channels

In a fading wireless channel, the received instantaneous signal power is scaled by $|h|^2$, where the channel coefficient, h is a random variable. Thus, the instantaneous SNR per symbol is defined as $\gamma = |h|^2 E_s/N_0$, and the average SNR per symbol becomes $\overline{\gamma} = \overline{|h|^2} E_s/N_0$. Due to the impact of fading on the received signal amplitude, the decision threshold of M-PAM given

in (4.16) for noise-limited condition will now change to the generalised form given by:

$$r_{\mathrm{th}_m} = (2m - M)\left(|h|^2 + N_0\lambda\right)\frac{1}{h}\sqrt{\frac{E_\mathrm{s}}{\xi_\mathrm{av}}}. \tag{4.24}$$

The effect of h and λ on the normalised third decision threshold point, $\overline{r}_{\mathrm{th}_3}$ is demonstrated in Fig. 4.10. For this instance, SNR = 10 dB is considered. For equiprobable case ($\lambda = 0$), and

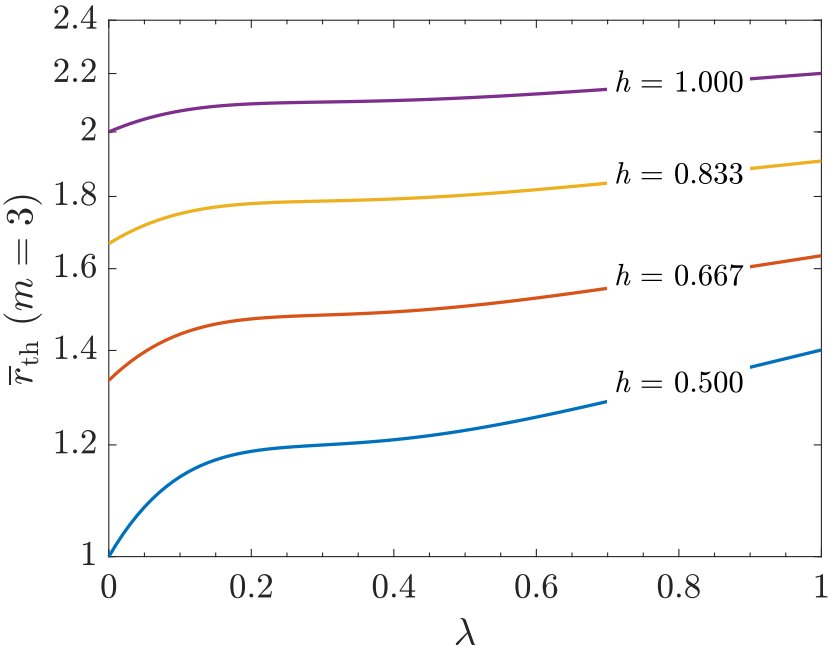

Figure 4.10: *The effect of rate parameter, λ and SNR per symbol, E_s/N_0 on the normalised third decision point, $\overline{r}_{\mathrm{th}_3}$ of PS-4-PAM*

strong attenuation ($h = 0.5$), the threshold is $\overline{r}_{\mathrm{th}_3} = 1$ as against $\overline{r}_{\mathrm{th}_3} = 2$ with $h = 1$. This figure shows that the threshold is no longer fixed but varies with h for any given λ and N_0. In noise-limited case, this depends on the SNR and λ as it was shown in Fig. 4.5.

The average symbol error probability in the a fading channel then becomes [158]:

$$P_{\mathrm{s|Fading}} = \int_0^\infty P_\mathrm{s}(\gamma)\, p_\gamma(\gamma)\, \mathrm{d}\gamma, \tag{4.25}$$

where $p_\gamma(\gamma)$ is a probability density function (PDF) of the instantaneous SNR which depends on the nature of the fading channel. $P_\mathrm{s}(\gamma)$ is evaluated by the SER expression defined in (4.13) and takes into account the impact of fading on decision thresholds given by (4.24). However, this leads to an expression which is not tractable. Therefore, in the following subsections, a

sub-optimum tractable SER of Rayleigh and log-normal fading channel conditions with the decision threshold based on (4.16) is presented. It should be noted that the analysis can be easily extended to other fading models.

4.4.1 Log-normal Fading Channel

The average symbol error probability in the presence of log-normal fading can be evaluated using (4.25) and its irradiance PDF, $p_\gamma(\gamma) = p_I(I)$, given by [159]:

$$p_I(I) = \frac{1}{\sqrt{2\pi\sigma_I^2}} \frac{1}{I} \exp\left(-\frac{\left(\ln\left(I/I_0\right) - \mu\right)^2}{2\sigma_I^2}\right), \quad I \geq 0 \tag{4.26}$$

where $\mu = -\sigma_I^2/2$ and σ_I are the mean and standard deviation of $\ln(I)$, respectively. From (4.21) and (4.26), the SER of PS-M-QAM in log-normal fading channel can be evaluated, using a Gauss-Hermite quadrature integration [160, equation 25.4.46], as:

$$P_{\mathrm{s}} \approx \frac{4}{\sqrt{\pi}} \sum_{n=1}^{N} w_n \sum_{m=1}^{\sqrt{M}-1} p_m Q\left(\Gamma_n \sqrt{\Omega_m \bar{\gamma}}\right) - \frac{4}{\sqrt{\pi}} \sum_{n=1}^{N} w_n \left(\sum_{m=1}^{\sqrt{M}-1} p_m Q\left(\Gamma_n \sqrt{\Omega_m \bar{\gamma}}\right)\right)^2 \tag{4.27}$$

where,

$$\Gamma_n = I_0 \exp\left(\nu_n \sqrt{2\sigma_I^2} - \sigma_I^2/2\right). \tag{4.28}$$

Here, $\{\nu_n\}$ and $\{w_n\}$ denote the zeros and weights of the N^{th}-order Hermite polynomial with $n = 1, 2, \cdots, N$, respectively. The accuracy of (4.27) depends on the order of the Hermite polynomial.

The SER performance comparison between PS-QAM in log-normal turbulence channel (expression (4.27)), validated with Monte Carlo simulation, and the corresponding uniformly distributed symbols is shown in Fig. 4.11. For this figure, the turbulence strength, $\sigma_I^2 = 0.1$ and Hermite polynomial order, $N = 20$, which gives effective approximation to a numerical integration, are considered. Using similar input rates as in the AWGN case, the PS-M-QAM symbols with entropy, H = {3.6, 5.4, 7.2} bit/symbol are generated for M = {16, 64, 256} respectively. The result demonstrates performance improvement from PS compared to the uniform distribution. At SER $= 10^{-3}$, for instance, PS-16-QAM, PS-64-QAM, and PS-256-QAM yield SNR gains of about 2.02 dB, 2.83 dB, 3.40 dB compared to the uniformly distributed QAM symbols, respectively. At the same SER and $\sigma_I^2 = 0.1$, the fading penalty is about 4.5 dB

for both schemes. These results reveal that PS can efficiently improve system performance in a log-normal fading channel as well.

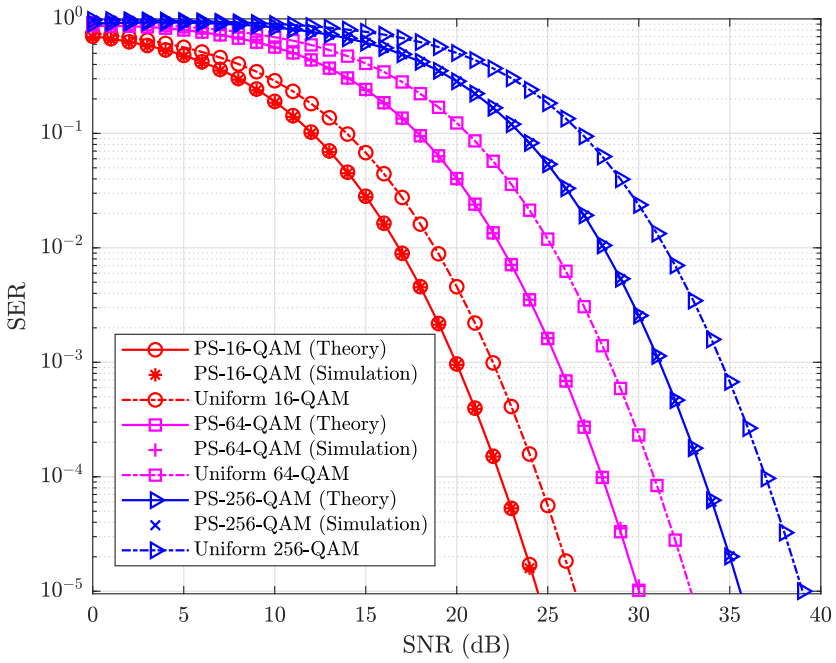

Figure 4.11: *Error performance of PS and uniformly distributed* QAM for different modulation orders in log-normal fading channel with $\sigma_I^2 = 0.1$

4.4.2 Rayleigh Fading Channel

The PDF of the instantaneous SNR for the Rayleigh fading channel is given by [158]:

$$p_\gamma(\gamma) = \frac{1}{\overline{\gamma}} \exp\left(-\frac{\gamma}{\overline{\gamma}}\right), \quad \gamma \geq 0. \tag{4.29}$$

Using (4.21) and (4.29) in (4.25), the symbol error probability of PS-M-QAM in Rayleigh fading channel is estimated as:

$$P_{\mathrm{s}} \approx 2 \sum_{m=1}^{\sqrt{M}-1} p_m \left(1 - \sqrt{\frac{\Omega_m \overline{\gamma}}{2+\Omega_m \overline{\gamma}}}\right) - \sum_{m=1}^{\sqrt{M}-1} p_m^2 \left(1 - \sqrt{\frac{\Omega_m \overline{\gamma}}{2+\Omega_m \overline{\gamma}}} \left(\frac{4}{\pi} \tan^{-1}\left(\sqrt{\frac{2+\Omega_m \overline{\gamma}}{\Omega_m \overline{\gamma}}}\right)\right)\right)$$
$$- \sum_{j=1}^{\sqrt{M}-1} \sum_{i=1}^{j-1} p_j p_i \left[2 - \frac{4}{\pi}\left(\sqrt{\frac{\Omega_i \overline{\gamma}}{2+\Omega_i \overline{\gamma}}} \tan^{-1}\left(\sqrt{\frac{2+\Omega_i \overline{\gamma}}{\Omega_i \overline{\gamma}}}\right) + \sqrt{\frac{\Omega_j \overline{\gamma}}{2+\Omega_j \overline{\gamma}}} \tan^{-1}\left(\sqrt{\frac{2+\Omega_j \overline{\gamma}}{\Omega_j \overline{\gamma}}}\right)\right)\right]. \tag{4.30}$$

Figure 4.12 shows the SER PS-QAM evaluated by (4.30) and its Monte Carlo simulation validation. To illustrate, the PS-M-QAM symbols with $M = \{16, 64, 256\}$ and entropy, $H = \{3.6, 5.4, 7.2\}$ bit/symbol are generated, respectively, similar to the AWGN cases. The theoretical uniformly distributed QAM performance under the Rayleigh fading condition is also plotted for comparison. The result demonstrates performance improvement from PS compared to the uniform distribution. At a particular SER of 10^{-3} , for instance, PS-16-QAM, PS-64-QAM,

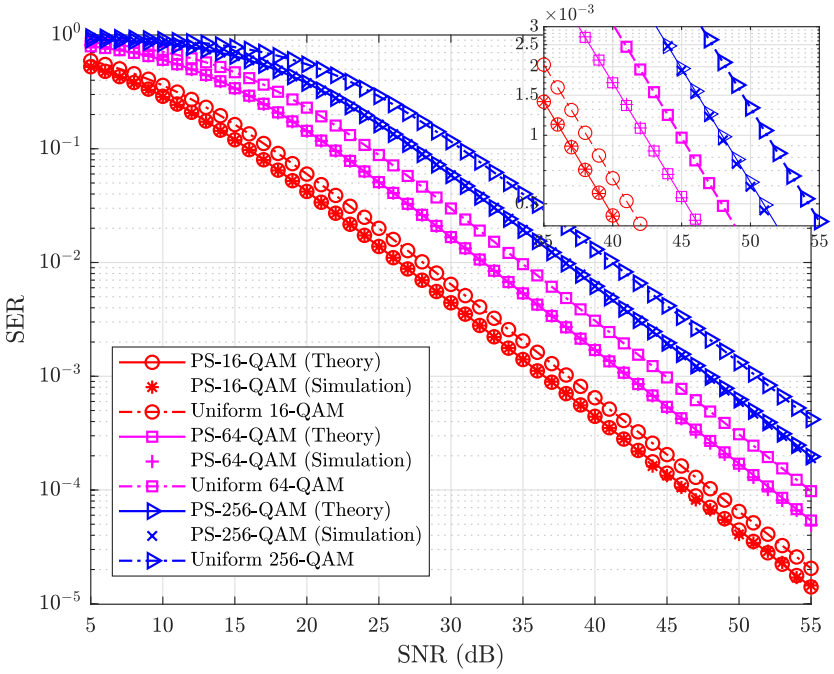

Figure 4.12: *Error performance of M-QAM for different modulation orders in Rayleigh fading channel. The inset shows the SER above 35 dB SNR.*

and PS-256-QAM yield SNR gain of about 1.63 dB, 2.59 dB, and 3.27 dB compared to the respective uniform QAM symbols. While at the same SER, the fading penalty is about 21 dB for both schemes. These results demonstrate that PS can effectively improve system performance in a Rayleigh fading wireless channel.

4.5 Achievable Information Rates of PS

In the following, the achievable information rate is presented as a performance metric of probabilistic shaping. The focus will be on both symbol-wise and bit-wise decoding achievable information rates.

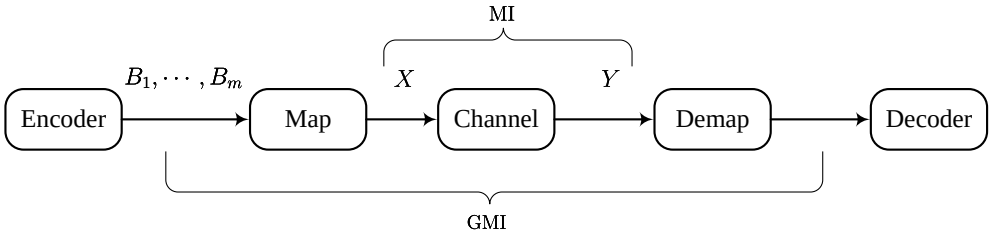

Figure 4.13: *Block diagram of a transmitter with probabilistic shaping, and symbol-wise mutual information (MI) and bit-wise demapper generalised mutual information (GMI) rates under a given channel*

Consider transmitted input symbols X and the corresponding output symbols Y under a memoryless channel, as shown in Fig. 4.13. The symbol-wise input X is consists of complex M-QAM symbols with unit energy, *i.e.* $\mathbb{E}\left[|X|^2\right] = 1$. The modulation order denoted by M takes on 2^m symbols, where m is number of bits per symbol. Only the case where m is even considered. Thus, M-QAM has a square constellation and can be decomposed into its constituent one-dimensional $\sqrt{M}$-PAM constellation.

4.5.1 Mutual Information

Mutual information measures the amount of information that can be obtained from output random variable Y after observing the transmitted input symbols X. It is determined by the entropy of the received symbol, $H(Y)$ and the conditional entropy $H(Y|X)$ and defined as [161]:

$$\mathbb{I}(X;Y) = H(Y) - H(Y|X) = \mathbb{E}\left[\log_2 \frac{P_{Y|X}(y|x)}{P_Y(y)}\right]. \tag{4.31}$$

Here, $P_{Y|X}(y|x)$ is the channel conditional probability density function, and $P_Y(y)$ is the marginal distribution of Y. Given the the transmitted symbols X, the memoryless and two-dimensional circularly symmetric channel conditional probability density is given by (4.7). Meanwhile, the marginal distribution of Y can be found using the marginal distribution of X denoted as $P_X(x)$ and $P_{Y|X}$ as:

$$P_Y(y) = \sum_{x \in X,\ y \in Y} P_{Y|X}(y|x)\, P_X(x). \tag{4.32}$$

To evaluate the mutual information using (4.31), a Monte Carlo simulations of N input-output pairs (x_k, y_k) of the channel can be used as an estimation. This gives achievable information rate in bit per symbol, $\mathrm{R_{SYM}}$ as a lower bound to the mutual information $\mathbb{I}(X;Y)$. That is:

$$\mathrm{R_{SYM}} \approx \frac{1}{N}\sum_{k=1}^{N} \log_2 \frac{P_{Y|X}(y_k|x_k)}{P_Y(y_k)}. \tag{4.33}$$

In Fig. 4.14, the simulation result of mutual information in bit per symbol evaluated using (4.33) is showed. For probabilistic shaped symbols, the entropy used in the simulation for 16-QAM, 64-QAM, and 256-QAM is 3.8, 5.7, and 7.6 bit/symbol, respectively. The Shannon's capacity limit in bit/symbol is also shown as a reference. As the SNR increases, the mutual information

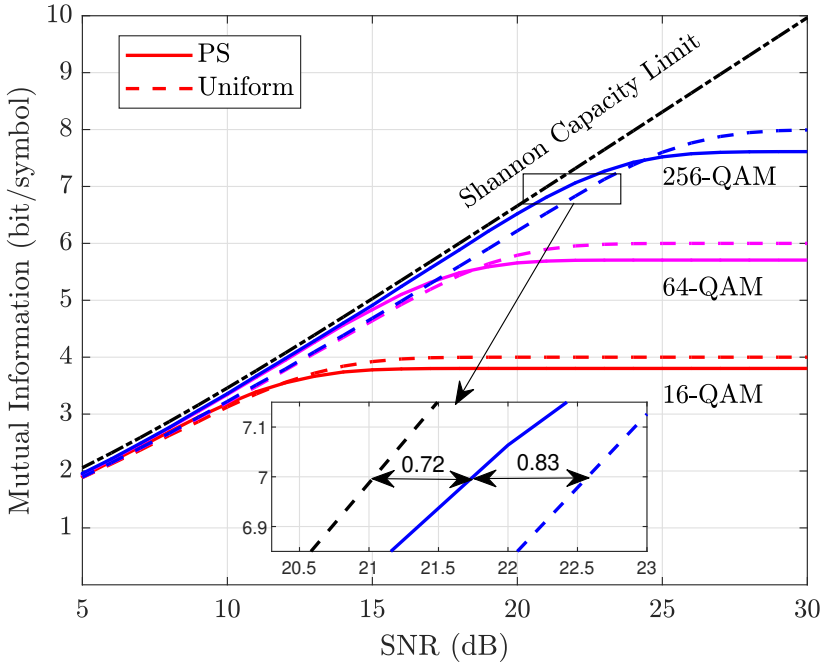

Figure 4.14: *Mutual information with SNR per symbol, defined as a ratio of signal energy to noise power spectral density, for uniformly distributed and probabilistic shaped 16-QAM, 64-QAM, and 256-QAM. The Shannon's capacity limit is shown as a reference.*

of 16-QAM, 64-QAM, and 256-QAM, for both uniformly distributed and probabilistic shaped, saturate to 4, 6, and 8 bit/symbol, respectively. The gain in probabilistic shaping in each of these modulation orders can be seen in the regions where the SNR is lower than the SNR threshold where the mutual information starts to saturate. That is, in the low SNR regime, the mutual

information of a probabilistic shaped symbols approaches the Shannon capacity limit. This can be seen in the the inset figure in Fig. 4.14. It shows that at 7 bit/symbol mutual information, 0.83 dB can be gained from probabilistic shaping over the uniformly distributed symbols while the gap to the Shannon's limit with the probabilistically shaped symbols is only about 0.72 dB.

4.5.2 Generalised Mutual Information

Mutual information is an important metric if the receiver and its decoders are not considered. Therefore, it generally provides the upper bound of an achievable information rate for a given input and a memoryless channel. However, a practical system will have a bit-wise demapper and binary decoder, as shown in Fig. 4.13. The symbol-wise shaped input X consists of m bit levels which can be represented by logical entities $B = B_1, \cdots, B_m$ and the decoder operates on bit-wise metrics. The effective performance metrics to accurately represent the achievable information rate of such a system with ideal binary soft-decision forward error correction (SD-FEC) decoding is the generalised mutual information (GMI) [162–164].

For a memoryless AWGN channel with independent and identically distributed discrete input, $X = (x_1, x_2, \cdots, x_N)$ and the corresponding output, $Y = (y_1, y_2, \cdots, y_N)$, the GMI can be calculated through the use of Monte Carlo simulation. This involves generating a large number of random samples from the joint distribution of the variables in question. By averaging the mutual information calculated from each of these samples, it is possible to estimate the GMI with a high degree of accuracy as [111]:

$$\mathrm{GMI} \approx \frac{1}{N}\sum_{n=1}^{N} -\log_2 P_X(x_n) - \frac{1}{N}\sum_{n=1}^{N}\sum_{i=1}^{m} \log_2\left(1 + \mathrm{e}^{(-1)^{b_{n,\,i}}\Lambda_{n,\,i}}\right). \tag{4.34}$$

The first term in (4.34) is the entropy of the constellation. The second term calculates the impact of channel noise from measured channel statistics and the probabilistic distributions. Moreover, $b_{n,\,i} \in \{0, 1\}$ is the i^{th} bit of the n^{th} transmit symbol, and the soft bit-wise demapper output, $\Lambda_{n,\,i}$ are the log-likelihood ratio (LLR) computed with 2D Gaussian auxiliary channel as [111]:

$$\Lambda_{n,i} = \log \frac{\sum_{x\in\chi_1^i} \mathrm{e}^{-\frac{|y_k - x|^2}{2\sigma_n^2}} P_X(x)}{\sum_{x\in\chi_0^i} \mathrm{e}^{-\frac{|y_k - x|^2}{2\sigma_n^2}} P_X(x)}, \tag{4.35}$$

where χ_1^i and χ_0^i denote the set of constellation points whose i^{th} bit is 1 or 0, respectively. σ_n^2

is the noise variance of the AWGN channel.

For an optical OFDM-based VLC, the GMI is measured from each data subcarriers. Once the GMI of each subcarrier is evaluated from the measured channel statistics and the distributions of the received symbols using (4.34), the overall data rate of the VLC system is obtained as:

$$R_{\mathrm{b}} = \frac{\sum_{k=1}^{\frac{N_{\mathrm{FFT}}}{2}-1} \mathrm{GMI}_k}{N_{\mathrm{FFT}} + N_{\mathrm{CP}}} \times R_{\mathrm{s}}, \tag{4.36}$$

where R_{s} is the symbol rate, and N_{CP} is the cyclic prefix size. Note that the data rate in (4.36) is an aggregate data rate before removing the FEC OH and an ideal FEC is assumed.

4.5.3 Normalised Generalised Mutual Information

GMI measures the number of information *bits per symbol* of a system with modulation order M that can be reliably transmitted through a channel. GMI can be normalised by the M, and a metric which quantifies the number of information *bits per transmit bit*, called the normalised generalised mutual information (NGMI) can be derived. Like GMI, NGMI is regarded as a reliable SD-FEC threshold for uniform as well as probabilistically shaped symbols [163]. NGMI is given by:

$$\mathrm{NGMI} \;=\; 1 - \frac{H - \mathrm{GMI}}{\log_2 M}, \tag{4.37}$$

with $0 \leq \mathrm{NGMI} \leq 1$, and H representing the source entropy as in (4.2). For uniform M-QAM, $H = \log_2 M$, and thus, (4.37) reduces to $\mathrm{NGMI} = \mathrm{GMI}/\log_2 M$. Note that, similar to NGMI, the forward error correction (FEC) code rate R_{c} quantifies the number of information *bits per transmit bit* [163]. Therefore, for a system with an ideal binary FEC, error-free decoding is possible if $\mathrm{NGMI} = R_{\mathrm{c}}$ while in a practical system $\mathrm{NGMI} = R_{\mathrm{c}} + \delta$ with $\delta \geq 0$. The required amount of ideal FEC overhead (OH) to achieve error-free post-FEC can also be inferred from the NGMI using [119]:

$$\mathrm{OH} = \frac{1 - \mathrm{NGMI}}{\mathrm{NGMI}}. \tag{4.38}$$

For example, if the NGMI of a system is 0.8, it can be inferred from the NGMI value that an ideal FEC with R_{c} = 0.8 and 25% FEC OH will be able to produce error-free post-FEC transmission.

4.6 Optical OFDM with PS

Various forms of OFDM modulation schemes have been proposed for VLC [84]. These modulation techniques should satisfy the requirement of intensity modulation (IM) to generate real and unipolar LED modulating signals. A DCO-OFDM is one of the most widely used spectrally efficient optical OFDM modulation schemes [90, 96]. In DCO-OFDM, a direct current bias is added to generate a unipolar signal. Furthermore, to realise real-valued OFDM waveform, Hermitian symmetry is imposed on the subcarriers of the OFDM frames such that $X[k] = X^*[N_{\mathrm{FFT}} - k]$ and $X[0] = X[N_{\mathrm{FFT}}/2] = 0$ where N_{FFT} is the number of subcarriers, and k is the subcarrier index as formulated in (2.9).

The response of a VLC channel is frequency-selective due to the limited modulation bandwidth of LEDs, and the channel itself [64]. Consequently, different subcarriers have different SNR values. Applying a fixed-rate OFDM, by allocating QAM signal with a fixed modulation order, to all subcarriers leads to underestimating the channel capacity [41]. Alternatively, the entropy of the system should be allocated adaptively for each subcarrier to maximise the AIR. This is attained by estimating the available SNR of each subcarrier, SNR_k, before the actual data transmission.

In the conventional bit-power loading scheme, the estimated SNR_k is used to adaptively assign the subcarriers with different QAM formats. It allows for higher modulation orders to be used in the subcarriers with higher estimated SNR. This is achieved while ensuring the target probability of error, P_b^{T}. In this work, the HD-FEC threshold of 3.8×10^{-3} which imposes 7% coding overhead is assumed. The bit-power loading which is based on the Levin-Campello algorithm [165]. The algorithm uses a modified form of the water-filling algorithm to optimise the bit and power distribution across the bits in a way that maximises the overall SNR of the system. The basic idea is to assign more information bits to subcarriers with higher SNR provided that the BER is less than the target BER. This involves the following optimisation on each OFDM subcarrier:

$$\text{maximise} \quad m_k = \log_2 M_k \tag{4.39a}$$

$$\text{subject to} \quad \mathrm{BER}\left(M_k, \mathrm{SNR}_k\right) \leq P_b^{\mathrm{T}} \tag{4.39b}$$

$$\sum_{k=1}^{\frac{N_{\mathrm{FFT}}}{2}-1} \nu_k^2 = N_{\mathrm{act}}. \tag{4.39c}$$

Here, m_k is the number of bit/symbol per subcarrier, N_{act} is the number of active data subcarriers with $m_k > 2$ bit/symbol, ν_k^2 is the power loading factor, and $\text{BER}\left(M_k, \text{SNR}_k\right)$ given by (4.40) [166], is the theoretical BER of M_k-QAM for subcarrier k with SNR_k.

$$\text{BER}\left(M_k, \text{SNR}_k\right) \approx \frac{4}{\log_2 M_k}\left(1 - \frac{1}{\sqrt{M_k}}\right) \times \sum_{l=1}^{2} Q\left((2l-1)\sqrt{\frac{3\text{SNR}_k}{M_k - 1}}\right). \tag{4.40}$$

The constraint in the adaptive bit-power loading technique is that it applies discrete integer-level bit allocation onto each subcarrier which is not a perfect fit for the channel frequency response. However, PS-based entropy loading can provide a better fit to the channel response and thus approach the channel capacity limit [167]. For PS-based optical OFDM scheme, different probabilistic constellation distributions with a fixed modulation order, M-QAM symbols are applied to individual subcarriers based on the pre-estimated SNR.

The PS-M-QAM constellation points are taken from $\chi = \{x_1, x_2, \cdots, x_M\}$ with PMF $P_X\left(x_i\right)$, in which its 1-dimensional PMF is chosen from the Maxwell-Boltzmann distribution shown in (4.1). To achieve a transmission rate close to the channel capacity in a subcarrier, C_k, the entropy of PS-M-QAM at subcarrier k, H_k should approach C_k. This involves adjusting P_X using an optimum rate parameter, λ which can be expressed as follows:

$$\text{minimise} \quad \left| -\sum_{\substack{i=1,\\ x_i \in \chi}}^{M_k} P_X\left(x_i\right) \log_2 P_X\left(x_i\right) - C_k \right| \tag{4.41a}$$

$$\text{subject to} \quad C_k = \log_2\left(1 + \text{SNR}_k\right). \tag{4.41b}$$

The following experimental demonstration will employ these two entropy loading optimisation processes and subsequently, performance comparisons will be made.

4.7 Experimental Demonstration of PS in VLC

In this section, the performance of experimental demonstrations of probabilistic shaping in single LED-based and WDM-based high-speed VLC systems is presented.

4.7.1 Single LED High-speed VLC with PS

This section details the experimental setup and results that demonstrate the performance comparison of adaptive bit-power loading and PS using a single low-power LED.

4.7.1.1 Experimental Setup

The block diagram in Fig. 4.15 lays out the signal generation and detection process for the DCO-OFDM VLC system. In the transmitter DSP , a stream of binary input is generated and

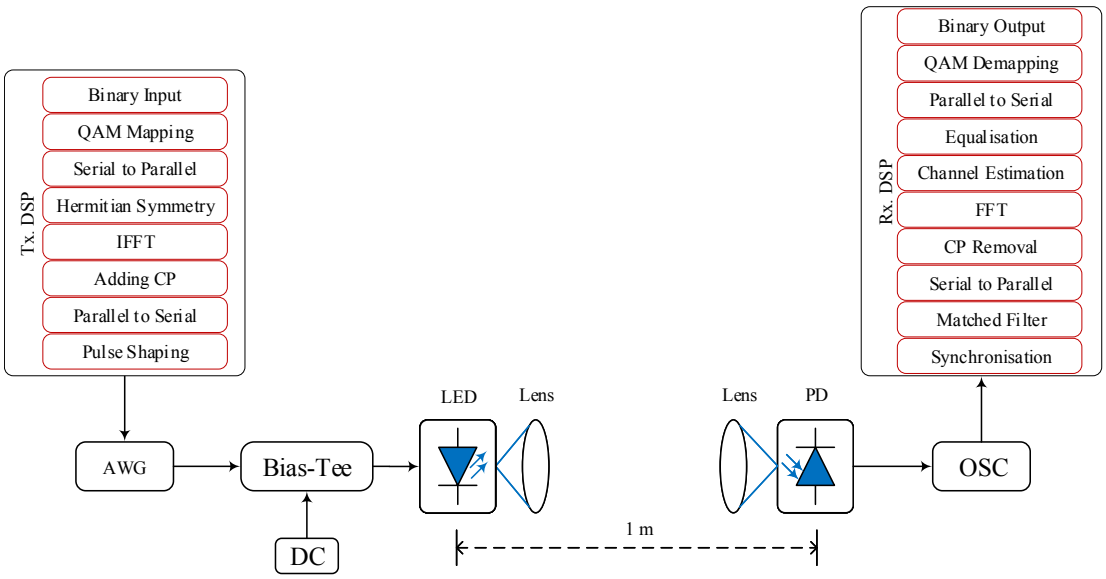

Figure 4.15: *Experimental setup with transmitter and receiver side offline DSP steps*

then mapped into M-QAM symbols. In the bit-power loading scheme, different QAM formats are applied, while for OFDM with the PS technique, a fixed M-QAM with different probabilistic constellation distributions is employed based on the pre-estimated SNR. After applying the Hermitian symmetry, each symbol is loaded onto the orthogonal subcarriers by employing an IFFT. The OFDM frame size is set to $N_{\text{FFT}} = 1024$ subcarriers. Cyclic prefixes (CPs) are inserted at the start of each OFDM frame. A value of $N_{\text{CP}} = 5$ is found to be sufficient for the ISI

to be removed [38, 40]. The symbols can then be multiplexed into serial time-domain output. A root-raised cosine (RRC) pulse shaping filter is employed to utilise the limited bandwidth of the optical link effectively [168]. The waveform pattern is then uploaded to an arbitrary waveform generator (AWG: Keysight 81180A) to generate the electrical modulating signal. The sampling rate of the AWG is set to 2 GSa/s. The output of the AWG is superimposed on the DC bias current via a bias-tee (Bias-Tee: Mini-Circuits ZFBT-4R2GW+). The output signal from the bias-tee is connected to the LED (VLMB1500-GS08). Since the half-power semi-angle of the LED is wide (*i.e.* about 65°), aspheric condenser lenses (Thorlabs ACL4532) are used to collimate the output light from the transmitter and focus it into the detection area of the photodetector.

At a receiver side with a link distance of 1 m, a photodetector (PD: ThorLabs PDA10A) is used to detect the intensity modulated signal. The receiver has a −3 dB bandwidth of 150 MHz and a built-in TIA with a gain of 5 V/mA. The received electrical signal is captured by an oscilloscope (OSC: Keysight MSO7104B) followed by processing in MATLAB. The received waveform from the oscilloscope is synchronised and then matched filter is applied. This is followed by removal of CP, and FFT operation. This provides the received QAM signal in the frequency domain at each of the subcarriers. The estimated frequency response of the system is used to equalise the received signal which can then be demodulated using the QAM demodulator.

Primarily, the channel response and available SNR at each subcarrier, SNR_k, are estimated using pilots composed of multiple 4-QAM-based OFDM frames. The SNR for each OFDM subcarriers is obtained by evaluating the EVM of the received pilot 4-QAM signal [169]. Note that, in PS-based OFDM, 1024-QAM symbols are mapped into individual subcarriers. The PS-1024-QAM symbols are generated from two orthogonal 32-PAM symbols. The choice of this higher modulation order allows utilising the available SNR to the full extent. However, it comes with a requirement of a greater number of sample points which goes beyond the memory depth of the available devices. Consequently, the GMI performance of PS-based system is evaluated offline from experimentally measured channel response. To carry out a fair comparison, this offline performance measurement is repeated for the bit-power loading technique as well and used to make a comparison with the PS technique. In addition, the performance of uniformly-loaded 8-QAM and 16-QAM OFDM technique are also investigated.

4.7.1.2 Experimental Results and Discussions

The VLC data transmission is performed at a 2 GSa/s sampling rate with an oversampling factor of 4 sample per symbol. Hence, the symbol rate, $R_s = 500$ MBaud. The DC bias point of the LED is a crucial parameter of the experiment. Details of the DC bias optimisation process is presented in Chapter 3. In this experiment, an optimum DC bias of 30 mA is applied to the LED which is measured to give approximately 21 MHz −3 dB electrical bandwidth. At the selected bias point, the system performance as a function of the modulation signal depth, (peak-to-peak voltage, Vpp) is investigated. The SNR distribution per subcarrier is shown in Fig. 4.16. As

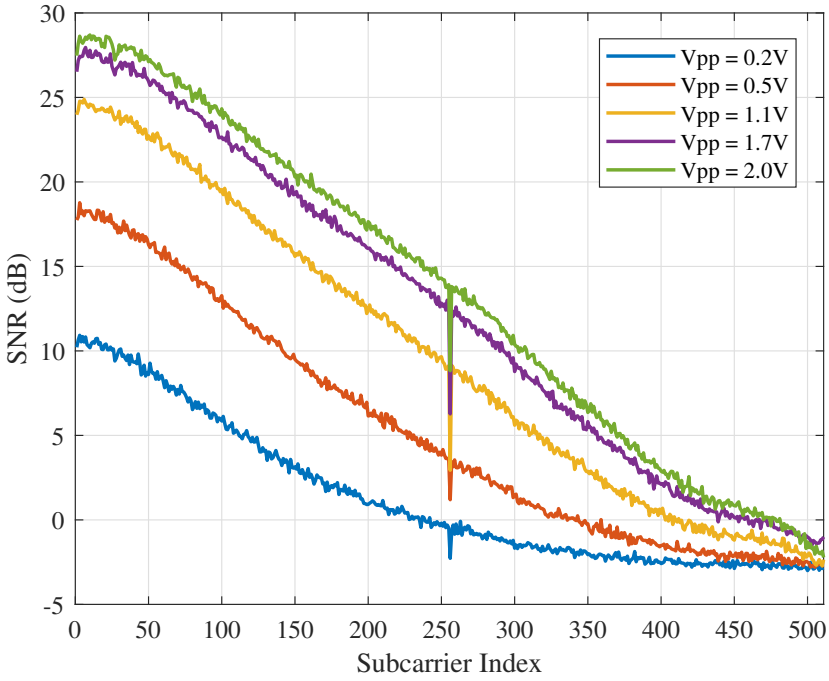

Figure 4.16: *Channel SNR response versus individual subcarriers for different signal depth at 30 mA DC bias*

expected, the SNR improves as Vpp increases. Yet, for all measurements, there is a sharp SNR drop at then 256th subcarrier, which is at 125 MHz frequency. This is due to harmonic distortion that can be caused by nonlinearities in electronic components used in the experiment. Despite reducing the number of bits that could be loaded onto this subcarrier, this will not affect the system error performance as bits are allocated based on the estimated SNR. Consequently, the VLC channel response at the optimised values for the DC bias at 30 mA and the modulation signal depth at 2 V is used in the adaptive bit-power loading and PS-based OFDM techniques.

The adaptive bit allocated per subcarrier is shown in Fig. 4.17 (a) along with the channel ca-

pacity which is also used as source entropy for PS-based OFDM. The entropy of the bit-power loading system takes only discrete integers with a maximum of 9 bit/symbol. Among 511 data subcarriers, 364 subcarriers are loaded with 2 bit/symbol or more. The corresponding power loading per subcarrier is also shown in Fig. 4.17 (b). On the contrary, the PS scheme takes

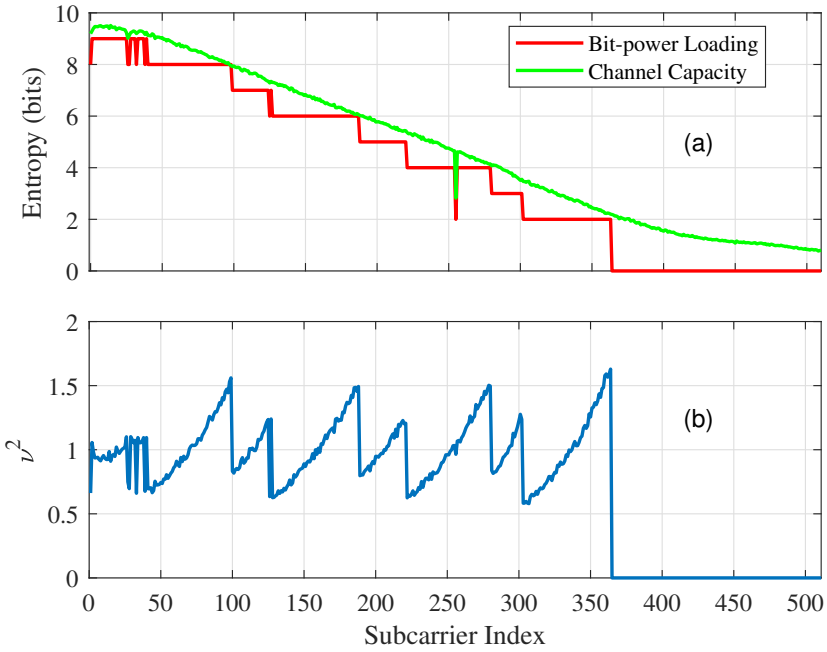

Figure 4.17: *The entropy and power allocation (a) showing bit loading and channel capacity per subcarrier and (b) power loading per subcarrier*

continuous entropy values and applies a fixed 1024-QAM signal. The graphical illustration of PS-1024-QAM signal at different subcarriers is shown in Fig. 4.18. Note that the distributions become more shaped as the entropy decrease, and the probability of occurrence of outer point may converge to zero.

To evaluate the information rates in each of the schemes, the GMI is evaluated from the experiment data. Figure 4.19 shows the GMI versus different subcarriers for bit-power loading and PS-1024-QAM. The GMI of uniformly-loaded 8-QAM and 16-QAM OFDM and the Shannon capacity limit of the channel are also presented as a performance reference. The uniform 8-QAM and 16-QAM OFDM schemes result in a maximum of 3 and 4 bit/symbol GMI per subcarrier, respectively in the high SNR region. As expected, this decreases with decreasing SNR. The GMI of the bit-power loading exhibits a gap to the capacity limit, and declines sharply in a staircase manner when the SNR drops. While the GMI of PS-1024-QAM approaches the Shannon capacity across all subcarriers, realising a near capacity transmission rate.

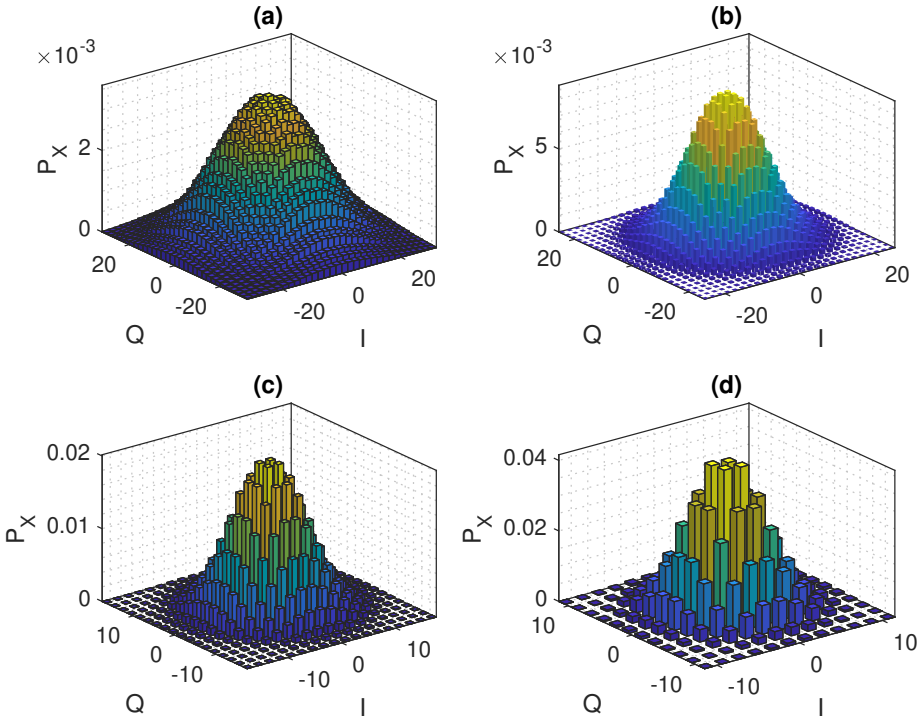

Figure 4.18: *Graphical illustration of PS-1024-QAM with four different entropy values at subcarrier index of (a) 50 (b) 100 (c) 150 and (d) 200*

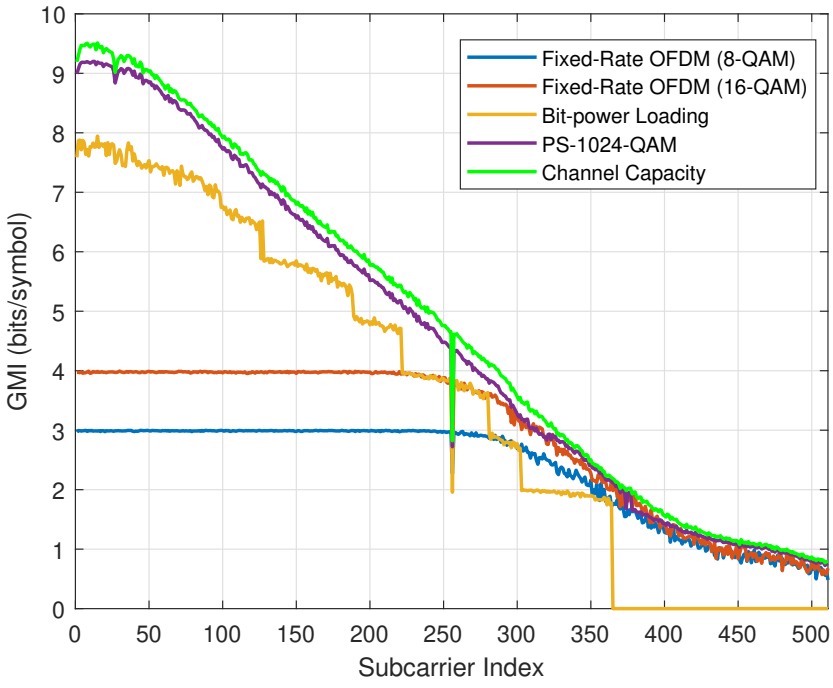

Figure 4.19: *Measured GMI per subcarrier for fixed-rate, bit-power loading and PS-based OFDM schemes*

In terms of NGMI, for the bit-power loading, the lowest NGMI is 0.8260 and requires an overall FEC OH of approximately 7%. Meanwhile, for PS the minimum NGMI is 0.9679 and reduced the required overall OH to just below 2%. The aggregate data rate of bit-power loading is 888.82 Mbps. While for PS, 1.13 Gbps can be achieved, indicating an increase of 27.13% compared to the bit-power scheme. These results clearly demonstrate with PS, the VLC information rate can be enhanced substantially.

4.7.2 WDM-Based High-speed VLC with PS

This section details the experimental setup and results that demonstrate the performance comparison of adaptive bit-power loading and PS in a WDM-based VLC system.

4.7.2.1 Experimental Setup

The system block diagram along with the picture of the setup in the lab is shown in Fig. 4.20. The signal generation and detection process of DCO-OFDM is implemented in MATLAB. In the transmitter side, a stream of binary input is generated and then mapped into M-QAM symbols. In the bit-power loading scheme, different QAM formats are applied at each subcarrier based on the pre-estimated SNR. For the PS-based OFDM system, a fixed M-QAM with different probabilistic constellation distributions is applied. Hermitian symmetry is imposed, and each symbol is loaded into orthogonal subcarriers by applying an IFFT. The OFDM frame size is set to $N_{\mathrm{FFT}} = 2048$ subcarriers. Cyclic prefixes (CPs) are inserted at the start of each OFDM frame. A value of $N_{\mathrm{CP}} = 5$ is found to be sufficient for the ISI to be removed [38, 40]. The symbols can then be multiplexed into serial time-domain output. The waveform pattern is then uploaded to an arbitrary waveform generator (AWG: Keysight M8195A). The sampling rate of the AWG is set to 16 GSa/s. Note that the modulating signals, for the three colours, are generated using different seeds and are thus independent of each other. Each output signal from the AWG is amplified (Amp1, Amp2, Amp3: Mini-Circuits ZHL-1A-S+) and fed into bias-tees (Bias-Tee: Mini-Circuits ZFBT-4R2GW+) which superimpose the OFDM signal with the DC bias current. Each bias-tee output is used to drive off-the-shelf red, green, and blue (598-8D10-107F, 598-8081-107F, 598-8D90-107F) micro-LEDs which have dominant wavelengths of 630 nm, 525nm, and 470nm, respectively. Since the half-power semi-angles of the LEDs are wide (*i.e.* about 70°), aspherical condenser lenses (L1, L2, L3: Thorlabs ACL4532) are used to collimate the output light from individual transmitters. The modulated output signals of all three

colours of LEDs are combined with dichroic mirrors as shown in Fig. 4.20. The first dichroic mirror (DM1: Thorlabs DMLP605L), which has a 620 - 800 nm transmission band and 605 nm cut-on wavelength, transmits red while reflecting the green signal. Another dichroic mirror (DM2: Thorlabs DMLP490L), with 505 - 800 nm transmission band and 490 nm cut-on wavelength, passes red and green while reflecting the blue signal. At this level, a combination of the red, green, and blue collimated light signal is attained.

The receiver is 50 cm away from the transmitter. It consists of the same configuration of dichroic mirrors to separate and send each colour to its respective photoreceiver. One dichroic mirror (DM3: Thorlabs DMLP490L) reflects the blue light while the other (DM4: Thorlabs DMLP605L) separates the green. Aspherical condenser lenses (L4, L5, L6: Thorlabs ACL50832) are used to focus the light into the active detection area of photodetectors (PD: New Focus 1601 AC). The receiver has a -3 dB bandwidth of 1 GHz and a built-in TIA with a gain of 700 V/A. The output signal of each receiver is captured by using the three channels of a high-speed oscilloscope (OSC: Keysight MSO7104B) sampling at 4 GSa/s and followed by signal processing in MATLAB. The received waveform from the oscilloscope is resampled and symbols synchronised. The CPs are then removed and the symbols demodulated.

In the experiment, the channel response and available SNR of each subcarrier, SNR_k, are estimated using pilots composed of multiple 4-QAM-based OFDM frames. The SNR for each OFDM subcarrier is obtained by evaluating the EVM of the received pilot 4-QAM signal [169]. Note that, in PS-based OFDM, 1024-QAM symbols are mapped into individual subcarriers for the red and blue links while 256-QAM is used in the green link. The PS-M-QAM symbols are generated from two orthogonal $\sqrt{M}$-PAM symbols. The choice of this higher modulation order allows utilising the available channel to the full extent. However, it comes with a requirement of a greater number of sample points which goes beyond the memory depth of the available oscilloscope. Consequently, the GMI performance of PS-based system is evaluated offline from experimentally measured channel response. To carry out a fair comparison, this offline performance measurement is repeated to the bit-power loading technique and used to make a comparison with the PS technique.

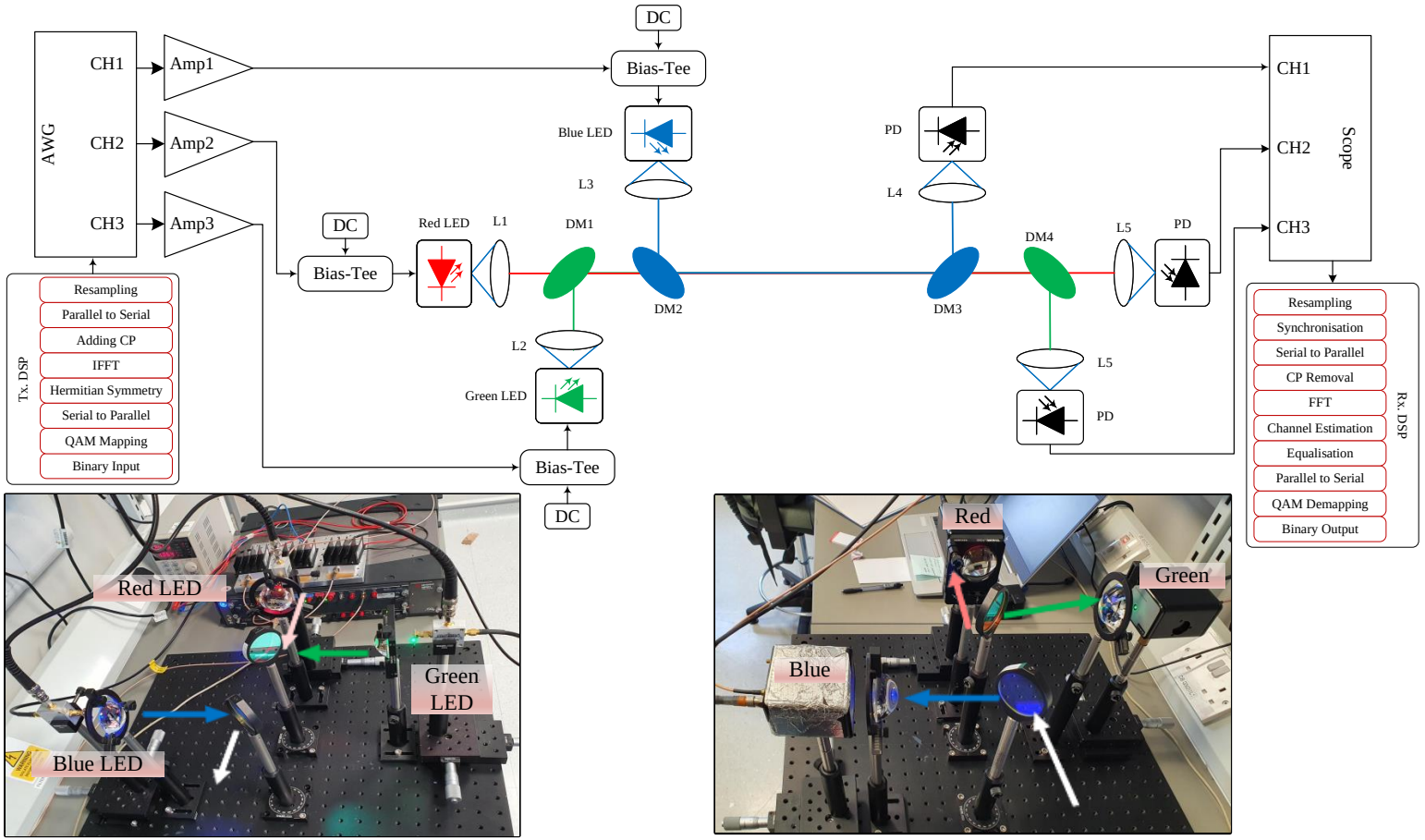

Figure 4.20: *Experimental setup with the picture of the setup at the transmitter and receiver sides, and signal generation and detection DSP steps*

4.7.2.2 Experimental Results and Discussions

The WDM-based VLC data transmission is performed at a symbol rate, R_s = 1.4 GBaud. The DC bias point of the LEDs is a significant parameter of the experiment. For each LED, the optimum driving point is determined by minimising the possible signal distortion while the information bits to be loaded is maximised. Details of the DC bias optimisation process is presented in Chapter 3. Accordingly, the DC bias of the red, green, and blue LEDs are found as 45 mA, 50 mA, 45 mA at which the −3 dB modulation bandwidths are 22 MHz, 32.4 MHz, and 51.5 MHz, respectively. Through an iterative process, the optimum values of modulating signal amplitude which maximise the SNR responses of the red, blue, and green LED links are found to be 450 mV, 350 mV, and 200 mV, respectively.

Figure 4.21 shows the overall SNR response of the system per subcarrier index at these optimum DC bias points and Vpp. In all measurements, a drop in SNR is observed at certain subcarrier indices due to nonlinear harmonic distortion in the system. This distortion is caused by nonlinearities in the electronic components used in the experiment. The harmonic distortion occurs at integer multiples of 125 MHz, specifically at the 183rd (125 MHz), 366th (250 MHz), 549th (375 MHz), 731st (500 MHz), and 914th (625 MHz) subcarriers. Despite reducing the

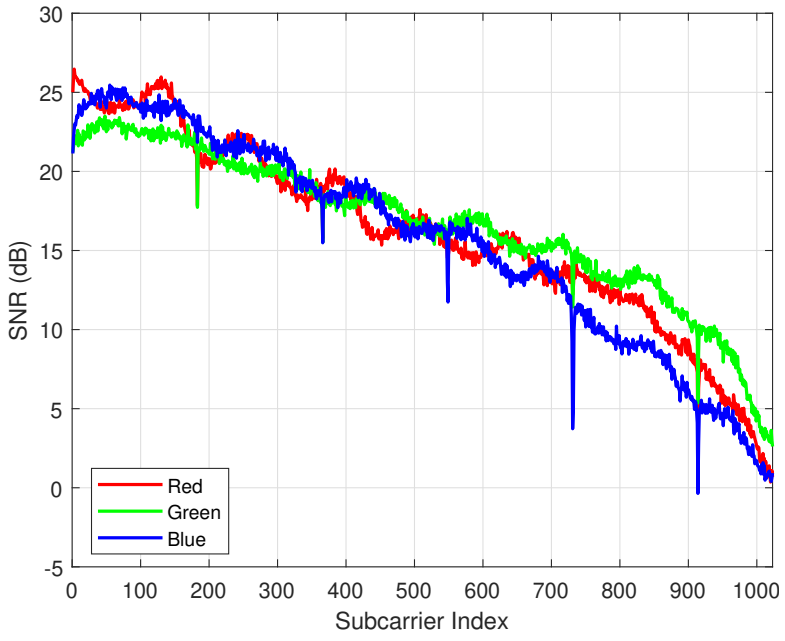

Figure 4.21: *Channel SNR response versus individual subcarriers for the red, green, and blue links at the optimum DC bias and Vpp*

number of bits that could be loaded onto these subcarriers, it does not affect the system error

performance as bits are allocated based on the estimated SNR. All the links exhibit comparable SNR responses in all frequency ranges.

The overall frequency response in terms of the channel gain of the system for each colour is also presented in Fig. 4.22. The amount of optical power detected by individual photodetectors is important to the channel gain. Even though the amount of optical cross-talk is found to be minimal, a substantial portion of power is lost due to the dichroic mirrors. The optical power detected by the red, green, and blue receivers with the dichroic mirrors in the setup is found to be only 91%, 89%, and 95% of the setup without the dichroic mirrors, respectively.

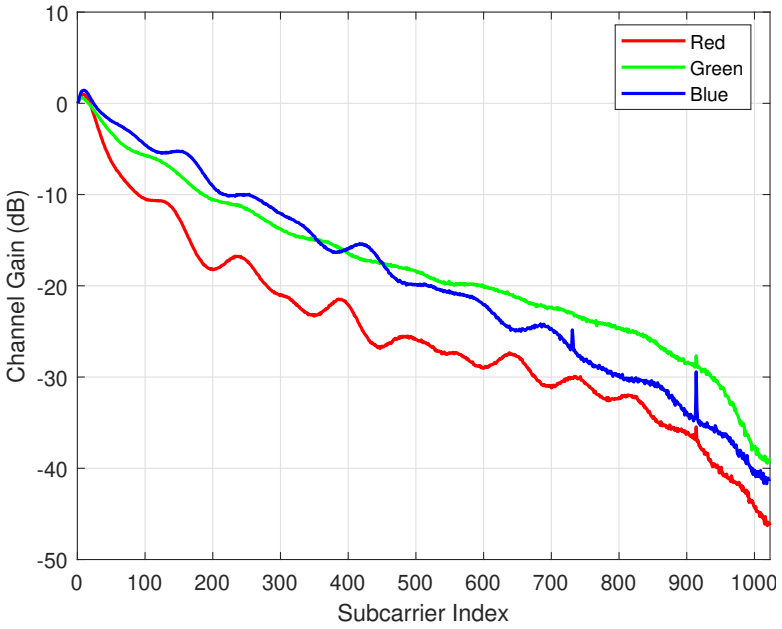

Figure 4.22: *Channel gain versus individual subcarriers for the red, green, and blue links at the optimum DC bias and Vpp*

The adaptive bit allocated per subcarrier and the rate used in the PS schemes for each of the links is shown in Fig. 4.23. The entropy of the bit-power loading system takes only discrete integers. For red, green, and blue links a maximum of 8 bit/symbol, 7 bit/symbol, and 8 bit/symbol are allocated. Besides, for red, green, and blue links 902, 953, and 857 data subcarriers, respectively, are loaded with at least two or more bit/symbol. The PS scheme is set to take continuous entropy values equal to the corresponding channel capacities. A fixed 1024-QAM signal level is applied in all subcarriers to both red and blue links, as these links can have above 8 bit/symbol entropy. Meanwhile, the green link can allocate just below 8 bit/symbol with which 256-QAM is employed.

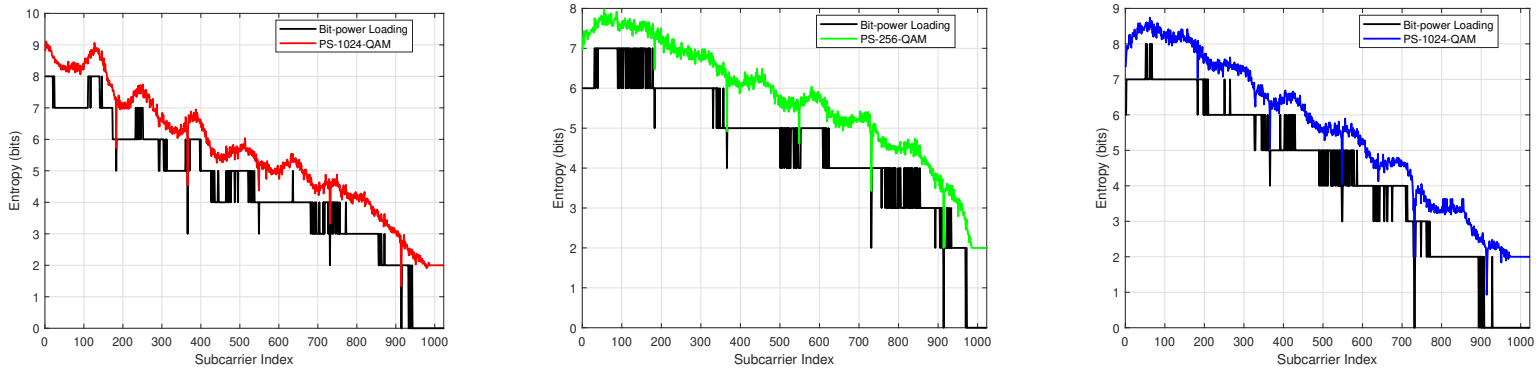

(a) *Red* **(b)** *Green* **(c)** *Blue*

Figure 4.23: *Entropy allocation per subcarrier in PS and bit-power loading for red, green, and blue links*

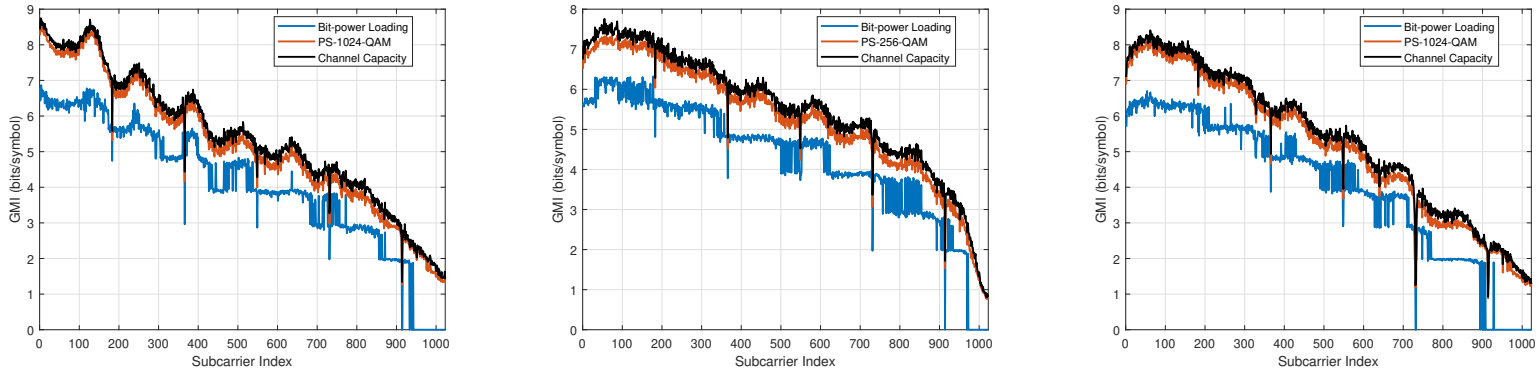

(a) *Red* **(b)** *Green* **(c)** *Blue*

Figure 4.24: *Measured GMI per subcarrier in PS and bit-power loading based OFDM schemes for red, green, and blue links*

The performance of the bit-power loading and PS schemes is analysed by evaluating the GMI values in each of the colours. These GMI results at different subcarriers applying bit-power loading and PS are shown in Fig. 4.24 for each colour. The GMI of Shannon's channel capacity of each link based on AWGN channel is also presented as a reference. In all three links, the PS-based OFDM technique approaches Shannon's capacity, while the bit-power loading exhibits a gap to the capacity limit across all subcarriers.

The NGMI result per subcarrier for each colour is also shown in Fig. 4.25. The PS has the highest and almost consistent NGMI values with average NGMI = $\{0.9757,\ 0.9712,\ 0.9760\}$ while for the bit-power loading the average NGMI = $\{0.9362,\ 0.9400,\ 0.9391\}$ for the red, green, and blue links, respectively. The corresponding FEC OH requirement in each scheme for each colours is shown in Table 4.1.

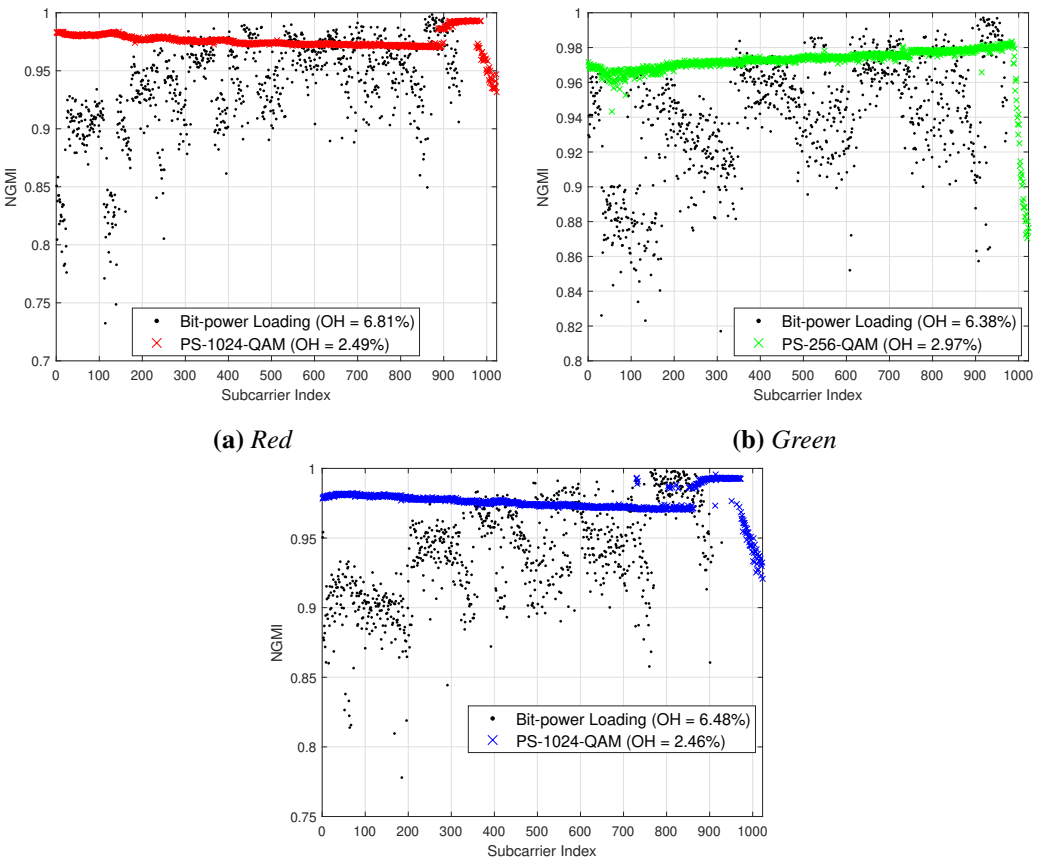

(a) *Red* **(b)** *Green*

(c) *Blue*

Figure 4.25: *NGMI per subcarrier in PS and bit-power loading based OFDM schemes for red, green, and blue links*

In terms of data rate, in PS, an aggregate data rate of 10.81 Gb/s is achieved. This is only with under 3% overall FEC OH requirement. The aggregate net data rate after the FEC OH reductions in each colour is 10.52 Gb/s. Meanwhile, using bit-power loading, only 8.60 Gb/s aggregate data rate with approximately 7% overall FEC OH requirement is attained. The net data rate after the FEC OH reduction is 8.04 Gb/s. The summary of data rates achieved in each scheme for each colour is shown in Table 4.1. The result indicates that PS improves the capacity by almost 25.7% (which is about 30.8% if the net data rate is considered) compared with the bit-power loading scheme and with a lower FEC OH requirement. At the same FEC OH of 3%, the gain is even higher at over 45.1%. These results clearly demonstrate that the VLC information rate can be enhanced substantially with the application of PS and WDM .

Table 4.1: *Summary of Data Rate and FEC OH Results*

	Data Rate (Gb/s)		FEC OH (%)		Net Rate (Gb/s)	
	BPL	PS	BPL	PS	BPL	PS
Red	2.84	3.61	6.81	2.49	2.65	3.52
Green	2.99	3.65	6.38	2.97	2.80	3.54
Blue	2.77	3.55	6.48	2.46	2.59	3.46
Aggregate	8.60	10.81	—		8.04	10.52

4.8 Summary

In this chapter, the use of VLC with PS is examined through both theoretical and experimental studies. The symbol error performance of PS with a MAP detection scheme is analysed, with closed-form analytical expressions being validated through Monte Carlo simulations. A framework is presented that demonstrates how PS can be used to trade energy efficiency for spectral efficiency, and how the design parameters can be chosen. The effect of the shaping rate parameter, which determines the probability distribution and therefore the source entropy and spectral efficiency, on the error performance of PS is also examined. The results of this study show that PS outperforms the use of a uniform distribution, and significantly reduces the SNR required to achieve a certain error probability.

Two experiments were conducted to demonstrate the practicality of this approach. In the first

experiment, a single low-power LED was used to achieve a data rate near the capacity limit. In the second experiment, a WDM-based VLC system was used, with three LEDs of different colours being independently modulated for parallel and simultaneous data transmission. In both experiments, the achievable rates of PS and adaptive bit-power loading techniques were compared. Unlike the bit-power loading optimisation method, PS provides continuous entropy loading, allowing for efficient use of the available bandwidth beyond the −3 dB point. In the first experiment, PS resulted in an aggregate achievable information rate of 1.13 Gbps, a 27.13% increase over the bit-power loading achievable information rate. In the second experiment, PS resulted in an aggregate achievable information rate of 10.81 Gbps, a 25.7% increase over the bit-power loading approach.

Overall, the use of VLC with PS has been demonstrated to be an effective method for increasing spectral efficiency and achieving higher data rates. The symbol error performance of PS was shown to outperform the use of a uniform distribution, requiring a lower SNR to achieve a certain error probability. This approach was then successfully implemented in two experimental demonstrations, resulting in significant increases in achievable information rate compared to the use of adaptive bit-power loading. These results demonstrate the potential for PS to be used in visible light communication systems to maximise information rate and approach capacity limits.

Chapter 5
Frequency Shift Chirp Modulation for Visible Light Communication

5.1 Introduction

A low-rate wireless network is a type of communication network that operates at a relatively low-data transmission rate and is designed to be simple, low-cost, and reliable [134]. These types of networks are often used in applications where power consumption is a major concern, such as the Internet of Things (IoT), where devices are often powered by batteries that need to last for an extended time [134, 135]. One solution for addressing the power consumption needs of low-rate wireless networks is to use VLC, which utilises energy-efficient, low-cost, and widely available LEDs as the means of transmitting data [136]. VLC is well-suited for low-power systems due to its inherent energy efficiency, making it an attractive option for use in low-rate wireless networks. However, to effectively utilise VLC in low-rate wireless networks, robust and sensitivity-constrained modulation techniques must be employed. Robust modulation techniques are those that can withstand interference and other disruptions, ensuring that data can be transmitted and received with high reliability. Sensitivity-constrained modulation techniques, on the other hand, are designed to minimise the amount of power needed to transmit data, thereby reducing the overall energy consumption of the system. By combining these two approaches, VLC can be used to transmit data with high reliability and low-power consumption, making it an ideal choice for use in low-rate wireless networks.

Modulation techniques such as OOK, and PAM are relatively easy to implement and have been thoroughly studied [82, 84, 170, 171]. While it is possible to achieve a 1 bit/s/Hz spectral efficiency with OOK, it is generally considered to be less energy efficient compared to other techniques [82]. Spectral efficiency of $\log_2 M$ bit/s/Hz can be achieved with M-ary PAM (M-PAM) but the required SNR increases with increasing M. On the contrary, in orthogonal modulation techniques such as M-ary PPM (M-PPM) and M-ary FSK (M-FSK), the energy efficiency improves as M increases at an expense of spectral efficiency [137–139]. Nevertheless, PPM suffers high PAPR and is sensitive to receiver synchronisation which requires complex

equalisation [85–87]. Meanwhile, FSK has a constant envelope property and requires relatively simpler equalisation [82, 142]. In [143], energy-efficient FSK compatible with VLC has been proposed for low-data rate and low-power IoT applications. An FSK-based underwater VLC has also been demonstrated in [172]. However, in frequency selective channels and applications where the modulation bandwidth is limited such as VLC, its performance degrades [145]. That is because FSK symbols mapped onto frequency region where the channel attenuation is larger will lead to erroneous detection. To overcome this, a symbol can be mapped to all frequencies linearly within the bandwidth forming a frequency shifted chirp signal, and hence the name frequency shift chirp modulation (FSCM); also known as chirp spread spectrum (CSS) in LoRa [145, 146]. This scheme has been studied well in literature including the error performance analysis and transmitter design for RF-based communication system [145, 147, 148].

In this chapter, an FSCM that is compatible with a VLC system for low-power and low-data rate application is studied. FSCM signal generation and detection process is presented. Furthermore, the error performance in noise-limited and frequency-selective channels with limited modulation bandwidth is analysed and validated with Monte Carlo simulations. Finally, a proof-of-concept experimental demonstration of the FSCM-based VLC system as well as its performance comparison with other conventional modulation schemes is presented.

The remaining sections of the chapter are structured as follows. The theoretical principles of FSCM are first introduced in Section 5.2. The demodulation process for detecting an FSCM signal in an AWGN channel is then presented in Section 5.3. Section 5.4 discusses the error performance and energy efficiency of FSCM in an AWGN channel, while Section 5.5 compares the energy and spectral efficiency of FSCM with other conventional modulation techniques. In Section 5.6, the experimental demonstration of the FSCM-based VLC system is presented and its performance is compared with other conventional modulation schemes. Finally, Section 5.7 provides a summary of the key points covered in the chapter.

5.2 Frequency Shift Chirp Modulation

A chirp signal produces a sinusoidal waveform whose frequency increases linearly over time using the entire allocated bandwidth for transmission [146]. Suppose a baseband transmission bandwidth, B in which a sample is transmitted every $T_{\text{sample}} = 1/B$. A chirp modulator with a cardinality of M sends a symbol at a symbol duration of $T_{\text{s}} = M \times T_{\text{sample}} = M/B$.

A chirp which transmits a symbol starting at the lowest frequency (0 Hz) and increasing linearly up to the highest frequency (*i.e.* B) is called a basic chirp [148]. The basic chirp can be regarded as transmitting a symbol "0", while the subsequent symbols $[1, 2, \cdots, M-1]$ are transmitted by cyclically shifting the frequency of the basic chirp. Hence, the name FSCM [145]. The frequency of a basic chirp is given by:

$$f_0(t) = ct, \quad 0 \leq t \leq T_\mathrm{s}, \tag{5.1}$$

where c is a chirp rate in which the frequency of the signal changes over a symbol duration, $c = B/T_\mathrm{s}$ [Hz/s]. Consequently, the continuous-time domain waveform of a basic chirp is defined by:

$$x_0(t) = \exp\left(\mathrm{j}2\pi \int_0^t f_0(\tau)\,\mathrm{d}\tau\right) = \exp\left(\mathrm{j}\pi ct^2\right). \tag{5.2}$$

An illustration of the waveform of a basic chirp, $x_0(t)$ with $M = 64$ and $B = 100$ kHz is shown in Fig. 5.1. It shows the frequency increasing linearly from 0 Hz to the maximum frequency which is 100 kHz.

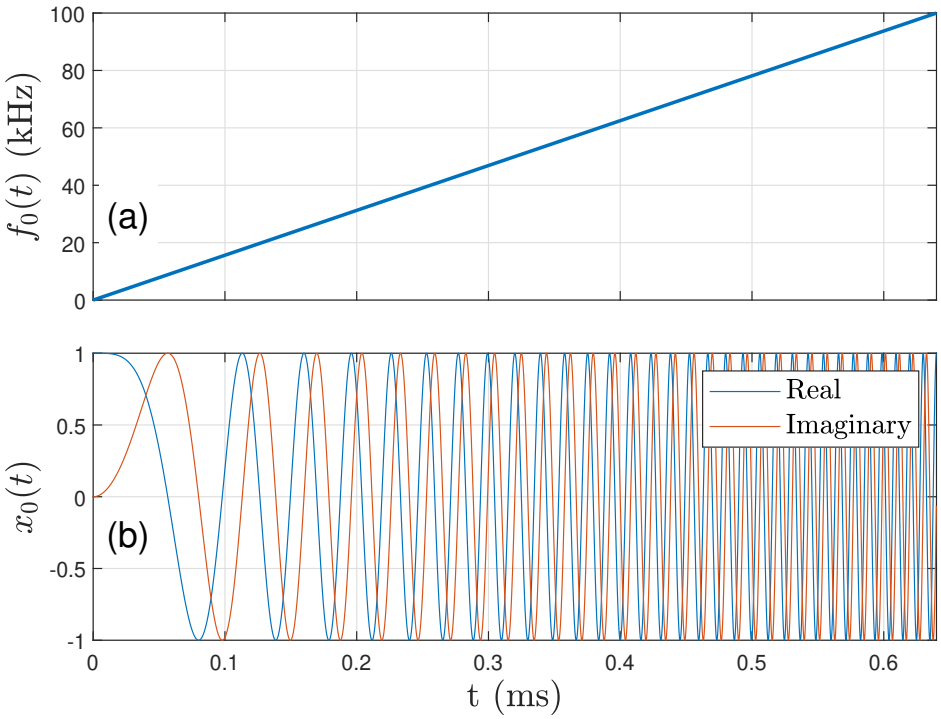

Figure 5.1: *A basic chirp signal with $M = 64$ and $B = 100$ kHz. In (a) the frequency, $f_0(t)$ is shown while (b) shows the real and imaginary parts of the basic chirp, $x_0(t)$.*

The chirp signal for M different symbols can be generated by cyclically shifting the basic chirp frequency. When the shifted frequency reaches the highest frequency within the symbol duration, it wraps down and starts from 0 Hz. For symbols $m = 0, 1, \cdots, M-1$, this can be realised by applying the *modulo* operator as follows:

$$f_m(t) = \mathrm{mod}\left(\frac{m}{T_\mathrm{s}} + f_0(t), B\right) = \mathrm{mod}\left(\frac{m}{T_\mathrm{s}} + ct, B\right). \tag{5.3}$$

This results in a frequency shift chirp modulated signal, $x_m(t)$. Figure 5.2 shows an example of FSCM signal with $M = 64$ and $B = 100$ kHz generated for symbols $m = [0, 1, 12, 33, 63]$ demonstrating the cyclic shift as m increases from 0 to 63. The basic chirp with $m = 0$ has a

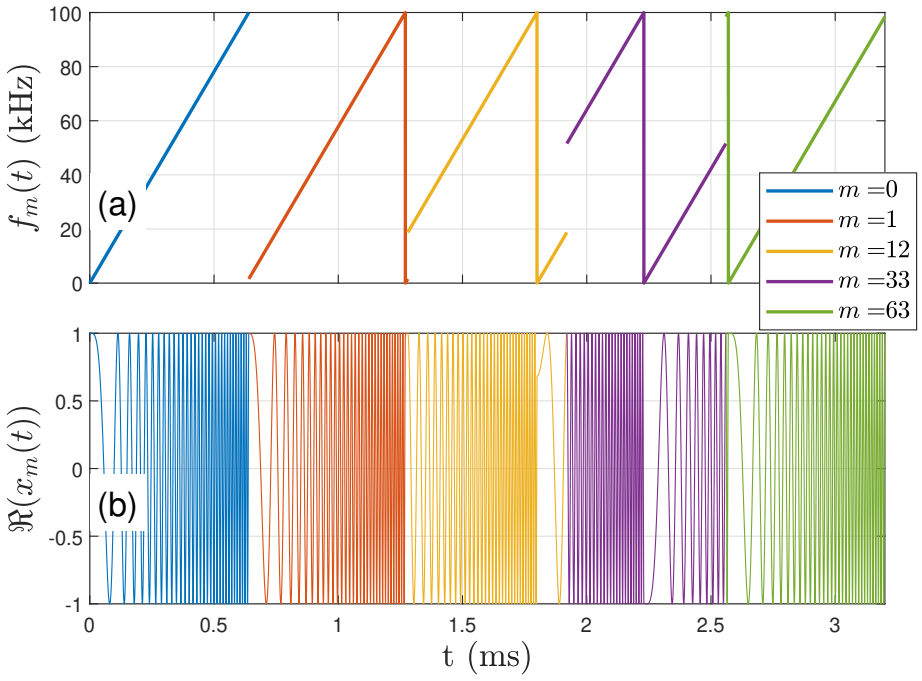

Figure 5.2: *A FSCM signal with $M = 64$ and $B = 100$ kHz, using $m = [0, 1, 12, 33, 63]$. The frequency of $f_m(t)$ is shown in (a) while the real part of the signal, $x_m(t)$ is plotted in (b).*

frequency which increases linearly from 0 Hz up to the 100 kHz bandwidth. The next symbol, $m = 1$ starts from $1/T_\mathrm{s}$, reaches B, and wraps down to 0 Hz, and increases the frequency within the symbol duration. More pronounced shifts in starting frequency, wrapping back to 0 Hz when maximum bandwidth is reached, and increasing linearly again can be observed in larger symbols $m = 12$, $m = 33$, and $m = 63$. Particularly in $m = 63$, which is the largest symbol for this 64-FSCM, the starting frequency, $63/T_\mathrm{s}$ is almost close to the B and thus wraps

down to 0 Hz in the shortest time and linearly increases again in the rest of the symbol duration. For all of these symbols, the real-time domain waveform shown in Fig. 5.2 (b) represents the frequency variations in Fig. 5.2 (a).

The continuous-time chirp symbol can be represented by M samples of $x_m(t)$ taken at a sampling rate, $F_{\text{sample}} = B$ over the symbol duration [145]. This is particularly important for digital implementation of this scheme in hardwares such as field programmable gate arrays (FPGA). Therefore, with digital samples (5.2) can be reformulated as:

$$x_0[n] = \exp\left(\mathrm{j}\pi c t^2\right)_{|t=nT_{\text{sample}}} \tag{5.4a}$$

$$= \exp\left(\mathrm{j}\pi \frac{B}{T_{\text{s}}} \left(nT_{\text{sample}}\right)^2\right) \tag{5.4b}$$

$$= \exp\left(\mathrm{j}\pi \frac{B^2}{M} n^2 B^{-2}\right) \tag{5.4c}$$

$$= \exp\left(\mathrm{j}\pi \frac{n^2}{M}\right), \tag{5.4d}$$

where $n = 0, 1, \cdots, M-1$. Similarly, the digital samples of $x_m[n]$ can be obtained by cyclically shifting the frequency of the basic chirp by m samples as:

$$f_m[n] = \mathrm{mod}\left(\frac{m}{T_{\text{s}}} + ct, B\right)_{|t=nT_{\text{sample}}} \tag{5.5a}$$

$$= \mathrm{mod}\left(\frac{m}{T_{\text{s}}} + \frac{B}{T_{\text{s}}} nT_{\text{sample}}, \frac{M}{T_{\text{s}}}\right) \tag{5.5b}$$

$$= \mathrm{mod}\left(\frac{m}{T_{\text{s}}} + \frac{n}{T_{\text{s}}}, \frac{M}{T_{\text{s}}}\right) \tag{5.5c}$$

$$= \mathrm{mod}\left(m + n, M\right). \tag{5.5d}$$

Moreover, $x_0[n]$ repeats itself after every M samples, *i.e.*, $x_0[n+M] = x_0[n]$, for all n. Consequently, the m^{th} digital FSCM signal can be written as $x_m[n] = x_0[n+M]$.

Despite the property mentioned above, which simplifies the implementation of $x_m[n]$, the FSCM is a complex-valued signal and therefore incompatible with VLC systems in its original form. While a real-valued chirp signal can be obtained by considering only the real part of $x_m[n]$ (as shown in Fig. 5.2 (b)), this work considers a complex-valued FSCM. The need for a complex-valued FSCM stems from the digital implementation approach and the chosen detection method. This choice enables easier and cost-effective implementation of the FSCM system into future hardware setups.

To generate a real and unipolar modulating signal, the DCO-OFDM approach used for complex-valued QAM signals is followed. This technique applies an IFFT on the FSCM signal and its Hermitian symmetry to generate a real-valued modulating signal. The input vector to the IFFT is written as:

$$\Gamma[k] = [0 \;\; x_m[0] \;\; x_m[1] \;\; \cdots \;\; x_m[M-1] \;\; 0 \;\; x_m^*[M-1] \;\; \cdots \;\; x_m^*[1] \;\; x_m^*[0]], \quad (5.6)$$

where $k = 0, 1, \cdots, N_{\text{IFFT}}$ and $n = 0, 1, \cdots, M-1$. N_{IFFT} denotes the order of IFFT. It can be seen from (5.6) that $\Gamma[k]$ requires at least $N_{\text{IFFT}} = 2(M+1)$. In Fig. 5.3, an FSCM symbol with $M = 4$ and $m = 3$ formed with (5.6) is shown as illustration. In this figure, (a) shows the real part of $\Gamma[k]$ and (b) shows $\gamma[n]$ which is the IFFT of $\Gamma[k]$. It clearly shows a symbol $m = 3$ mapped across all available frequencies $k = 1, 2, 3, 4$.

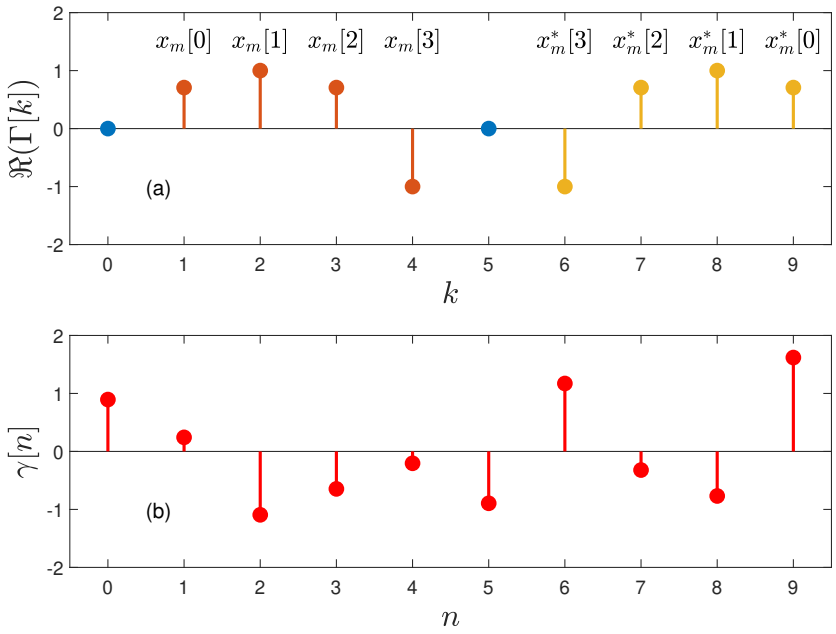

Figure 5.3: *An FSCM symbol with $M = 4$ and $m = 3$ showing (a) the real part of $\Gamma[k]$ and (b) $\gamma[n]$ which is the IFFT of $\Gamma[k]$.*

Note that this additional signal processing takes place in the transmitter, effectively representing the FSCM waveform in the frequency domain. As a result, the transmitted signal is the equivalent time-domain representation of digitised FSCM signal. This encoding technique typically spreads the FSCM symbol across multiple frequency tones, as opposed to the conventional FSK. This can be further illustrated by comparing the PSD of the transmitted waveform of the 4-FSCM and 4-FSK schemes. Figure 5.4 depicts the PSD of the transmitted wave-

form generated from 4-FSCM, while Figure 5.5 illustrates the PSD of 4-FSK. In the 4-FSCM scheme, a symbol is spread across all available frequency tones, with each tone separated by $\Delta f = F_{\mathrm{s}}/N_{\mathrm{IFFT}} = 0.1 \times F_{\mathrm{s}}$. Conversely, in 4-FSK, each symbol is allocated to a single frequency tone, with different frequency tones representing different symbols.

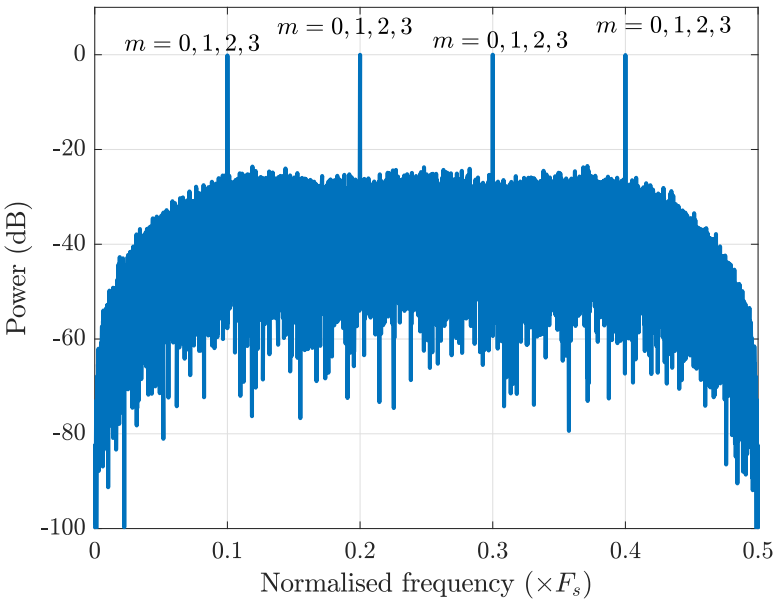

Figure 5.4: *A* PSD of 4-FSCM modulating signal (after the Hermitian symmetry and IFFT operation). A symbol is spread across four frequency tones.

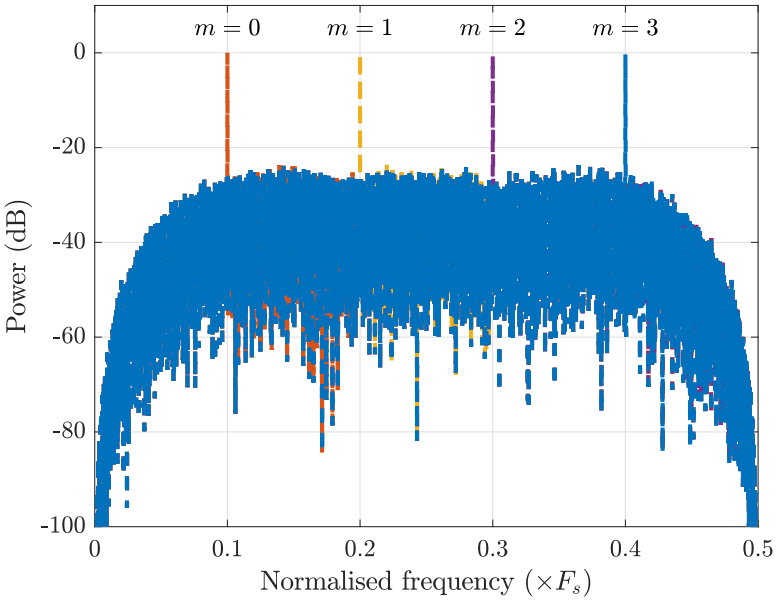

Figure 5.5: *A* PSD of an 4-FSK signal, each frequency tones representing a different symbol.

5.3 Detection of FSCM Signal in AWGN Channel

In this section, the detection process of FSCM signal is discussed. Consider an ideal noise-limited channel shown in Fig. 5.6 with FSCM signal generation and detection steps.

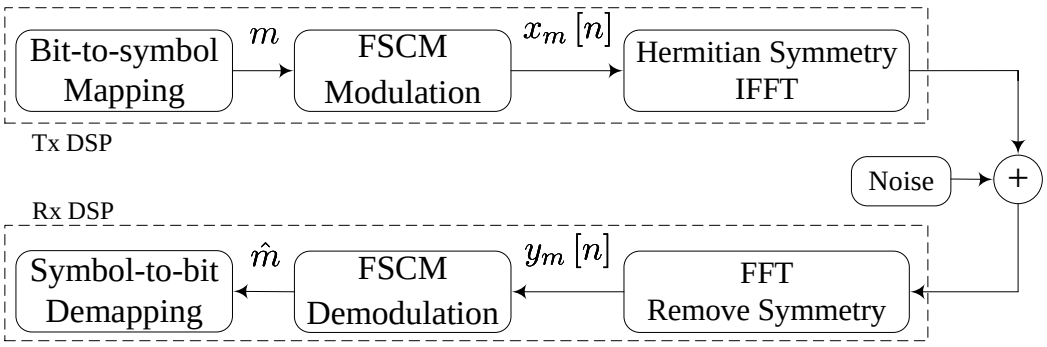

Figure 5.6: *Signal processing steps of FSCM-based VLC. The Hermitian symmetry operation provides* $\Gamma[k]$ *as shown in* (5.6)*. The IFFT of* $\Gamma[k]$ *results in* $\gamma[n]$.

After applying the FFT and removing the Hermitian symmetry, the received FSCM signal can be given by:

$$y_m[n] = x_m[n] + w[n], \tag{5.7}$$

where $w[n]$ is an AWGN sample. The recovery of symbols from $y_m[n]$ involves multiplying it with the complex conjugate of the basic chirp signal, $x_0^*[n]$, and taking the FFT to the product [145]. The product is evaluated as:

$$v_m[n] = y_m[n]\, x_o^*[n] \tag{5.8a}$$

$$= \exp\left(\mathrm{j}\pi\frac{(m+n)^2}{M}\right)\exp\left(-\mathrm{j}\pi\frac{n^2}{M}\right) + \hat{w}[n] \tag{5.8b}$$

$$= \exp\left(\mathrm{j}\pi\frac{(m^2+2nm)}{M}\right) + \hat{w}[n], \tag{5.8c}$$

where $\hat{w}[n] = w[n]\, x_o^*[n]$ is also an AWGN noise. The above process is known as dechirping and it unwraps the linear frequency shift into a constant frequency within the symbol duration.

Following dechirping, the FFT is applied to $v_m[n]$ to result in:

$$V_m[l] = \frac{1}{\sqrt{M}} \sum_{n=0}^{M-1} v_m[n] \exp\left(\frac{-\mathrm{j}2\pi nl}{M}\right) \tag{5.9a}$$

$$= \frac{1}{\sqrt{M}} \sum_{n=0}^{M-1} \left(\exp\left(\mathrm{j}\pi \frac{(m^2+2nm)}{M}\right) + \hat{w}[n]\right) \exp\left(\frac{-\mathrm{j}2\pi nl}{M}\right) \tag{5.9b}$$

$$= \frac{1}{\sqrt{M}} \sum_{n=0}^{M-1} \left(\exp\left(\mathrm{j}\pi \frac{(m^2+2nm-2nl)}{M}\right)\right) + W[l] \tag{5.9c}$$

$$= \frac{1}{\sqrt{M}} \exp\left(\frac{\mathrm{j}\pi m^2}{M}\right) \sum_{n=0}^{M-1} \left(\exp\left(\frac{\mathrm{j}2n\pi\,(m-l)}{M}\right)\right) + W[l] \tag{5.9d}$$

$$= \begin{cases} \sqrt{M} \exp\left(\frac{\mathrm{j}\pi m^2}{M}\right) + W[l], & \text{if } l = m \\ W[l], & \text{otherwise.} \end{cases} \tag{5.9e}$$

Here, $W[l]$ denotes the FFT of $\hat{w}[n]$. From (5.9e), it can be seen that $V_m[l]$ is an impulse located at the m^{th} bin while it is noise only in the other $M-1$ bin locations. Therefore, the received symbol can be detected easily by finding the index where the envelope of $V_m[l]$ is maximum. That is,

$$\hat{m} = \underset{0 \le l \le M-1}{\arg\max} \left|V_m[l]\right|. \tag{5.10}$$

5.4 Error Performance in AWGN Channel

In this analysis, M equiprobable, equal energy FSCM orthogonal signals transmitted over an AWGN channel is assumed. Moreover, symbols are demodulated based on the envelope detector of an orthogonal signal shown in (5.10). Let us define independent random variables $R_l = |V_m[l]|$, $0 \le l \le M-1$. It has been shown that R_0 has a Rician distribution with shape parameter $\kappa = s^2/2\sigma^2 = E_\mathrm{s}/N_0$ [155]. Here, $E_\mathrm{s} = \log_2 M \times E_\mathrm{b}$ is the average symbol energy, E_b is the bit energy, and $\sigma^2 = N_0/2$, is the single-sided noise PSD. The PDF of R_0 is then given by [155]:

$$p_{R_0}(r_0) = \frac{r_0}{\sigma^2} I_0\left(\frac{sr_0}{\sigma^2}\right) \exp\left(-\frac{r_0^2+s^2}{2\sigma^2}\right), \tag{5.11}$$

where $r_0 > 0$ and $I_0(\cdot)$ is the modified Bessel function of the first kind with order zero. Meanwhile R_l for $1 \le l \le M-1$, is a Rayleigh distributed random variable with a PDF [155]:

$$p_{R_l}(r_l) = \frac{r_l}{\sigma^2} \exp\left(-\frac{r_l^2}{2\sigma^2}\right), \tag{5.12}$$

and $r_l > 0$. If a symbol $m = 0$ is assumed to be transmitted, the symbol will be detected correctly if $R_l < R_0$ for $1 \leq l \leq M-1$. This probability of detecting the symbol correctly can be written as:

$$P_c = P\left[R_1 < R_0, R_2 < R_0, \cdots, R_{M-1} < R_0\right] \tag{5.13a}$$
$$= \int_0^\infty P\left[R_1 < r_0, R_2 < r_0, \cdots, R_{M-1} < r_0 | R_0 = r_0\right] p_{R_0}\left(r_0\right) \mathrm{d}r_0 \tag{5.13b}$$
$$= \int_0^\infty \left(P\left[R_1 < r_0\right]\right)^{M-1} p_{R_0}\left(r_0\right) \mathrm{d}r_0. \tag{5.13c}$$

In (5.13c), the symbol equiprobable condition is applied. And,

$$P\left[R_1 < r_0\right] = \int_0^{r_0} p_{R_1}\left(r_1\right) \mathrm{d}r_1 \tag{5.14a}$$
$$= 1 - \exp\left(-\frac{r_0^2}{2\sigma^2}\right), \tag{5.14b}$$

which can be expanded, using the binomial expansion, to:

$$\left(1 - \exp\left(-\frac{r_0^2}{2\sigma^2}\right)\right)^{M-1} = \sum_{n=0}^{M-1} (-1)^n \binom{M-1}{n} \exp\left(-\frac{n r_0^2}{2\sigma^2}\right). \tag{5.15}$$

Substituting (5.11) and (5.15) into (5.13c) gives:

$$P_c = \sum_{n=0}^{M-1} (-1)^n \binom{M-1}{n} \int_0^\infty \exp\left(-\frac{n r_0^2}{2\sigma^2}\right) \frac{r_0}{\sigma^2} I_0\left(\frac{s r_0}{\sigma^2}\right) \exp\left(-\frac{r_0^2 + s^2}{2\sigma^2}\right) \mathrm{d}r_0 \tag{5.16a}$$
$$= \sum_{n=0}^{M-1} (-1)^n \binom{M-1}{n} \int_0^\infty \frac{r_0}{\sigma^2} I_0\left(\frac{s r_0}{\sigma^2}\right) \exp\left(-\frac{(n+1) r_0^2 + s^2}{2\sigma^2}\right) \mathrm{d}r_0 \tag{5.16b}$$
$$= \sum_{n=0}^{M-1} (-1)^n \binom{M-1}{n} \exp\left(-\frac{n s^2}{2\left(n+1\right)\sigma^2}\right) \Theta\left(n\right), \tag{5.16c}$$

where,

$$\Theta\left(n\right) = \int_0^\infty \frac{r_0}{\sigma^2} I_0\left(\frac{s r_0}{\sigma^2}\right) \exp\left(-\frac{(n+1) r_0^2 + \frac{s^2}{n+1}}{2\sigma^2}\right) \mathrm{d}r_0 \tag{5.17a}$$
$$= \frac{1}{n+1} \int_0^\infty \frac{\grave{r}}{\sigma^2} I_0\left(\frac{\grave{r}\grave{s}}{\sigma^2}\right) \exp\left(-\frac{\grave{r}^2 + \grave{s}^2}{2\sigma^2}\right) \mathrm{d}\grave{r} \tag{5.17b}$$
$$= \frac{1}{n+1}. \tag{5.17c}$$

In (5.17b), a change of variable is introduced such that:

$$\begin{aligned} \grave{r} &= r_0\sqrt{n+1} \\ \grave{s} &= \frac{s}{\sqrt{n+1}}, \end{aligned} \tag{5.18}$$

and the integration reduces to 1 as it covers the full area of a Rician distribution. Therefore, using (5.17c) and noting that $\kappa = s^2/2\sigma^2 = E_\mathrm{s}/N_0 = \log_2 M \times E_\mathrm{b}/N_0$, correct error detection can be written as:

$$P_c = \sum_{n=0}^{M-1} \frac{(-1)^n}{n+1}\binom{M-1}{n} \exp\left(-\frac{n}{n+1}\log_2 M \frac{E_\mathrm{b}}{N_0}\right). \tag{5.19}$$

Then the probability of a symbol error becomes $P_e = 1 - P_c$ and can be given by:

$$P_e = \sum_{n=1}^{M-1} \frac{(-1)^{n+1}}{n+1}\binom{M-1}{n} \exp\left(-\frac{n}{n+1}\log_2 M \frac{E_\mathrm{b}}{N_0}\right). \tag{5.20}$$

The bit error probability (BER) can be evaluated by taking the relation $P_b = \frac{M}{2(M-1)}P_e$ as:

$$P_b = \frac{M}{2\,(M-1)} \sum_{n=1}^{M-1} \left[\frac{(-1)^{n+1}}{n+1}\binom{M-1}{n} \exp\left(-\frac{n}{n+1}\log_2 M \frac{E_\mathrm{b}}{N_0}\right)\right]. \tag{5.21}$$

It can be seen that the bit error probability of FSCM signal is the same as orthogonal and non-coherent FSK as both schemes employ orthogonal signalling with non-coherent envelope detection [155]. The BER of FSCM has also been reduced using further approximations to [147, 173]:

$$P_b \approx \frac{M}{2\,(M-1)} \times Q\left(\sqrt{2\log_2 M \frac{E_\mathrm{b}}{N_0}} - \sqrt{2\left(\ln(2)\log_2 M + \gamma_\mathrm{EM}\right)}\right), \tag{5.22}$$

where $\gamma_\mathrm{EM} \approx 0.57722$ is the Euler–Mascheroni constant. Figure 5.7 shows the BER of FSCM given in (5.21) for M = 4, 8, 16, 32, and 64, also validated by Monte Carlo simulations. It can be seen that for a given BER of FSCM signal, the amount of SNR required decreases as M increases. This allows the FSCM signal to achieve arbitrary small bit error at low SNR by increasing M which increase the energy efficiency, albeit at the cost of spectral efficiency.

In noise-limited channel scenarios the error performance of FSCM is the same as FSK. However, for channels with limited transmission bandwidth such as in VLC, FSCM outperforms

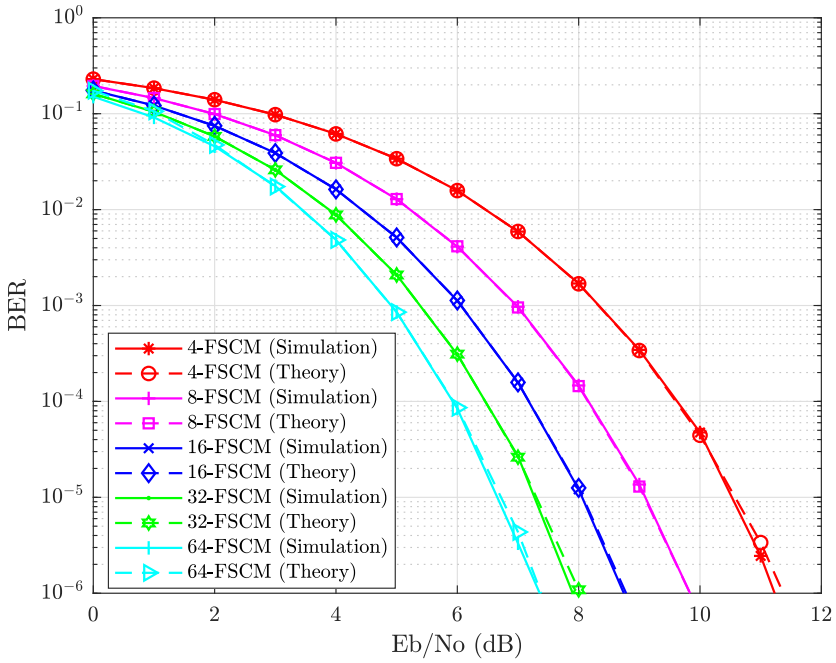

Figure 5.7: *BER of FSCM for different modulation orders under AWGN channel condition*

FSK. This is because, in FSCM, a symbol is represented by samples which are allocated through the entire bandwidth leading to an averaging of the effect of bandwidth limitation. On the contrary, an FSK symbol is mapped only onto a certain frequency and a symbol allocated in a frequency where the channel attenuation is larger will contribute to a higher error. To validate this, a simulation is carried out in a band-limited channel with noise using a first-order low pass filter (LPF). The LPF is designed in such a way that its cut-off frequency is the bandwidth of the FSCM and FSK signals. Moreover, the signal bandwidth is kept constant when the modulation order is increased by decreasing the separation frequency between consecutive symbols. Therefore, using the illustration shown in Fig. 5.4, the FSCM and FSK signal have a normalised modulation bandwidth of 0.5 Hz/sample/sec, making the normalised −3 dB bandwidth of the LPF 0.5 Hz/sample/sec. The amplitude response of this LPF is shown in Fig. 5.8. To illustrate the impact of the LPF, the PSD of 4-FSCM signal depicted in Fig. 5.4 is shown in Fig. 5.9 after the LPF. As expected, symbols in higher frequencies are attenuated more than the symbols in low frequencies. Note that for FSK this means $m = 3$ has a severe attenuation impact than $m = 0$, if the PSD of 4-FSK shown in Fig. 5.5 is considered. For FSCM, however, the same content of $m = 3$ is still available in other less attenuated frequencies.

The error performance simulation result is shown in Fig. 5.10. As expected, with increasing

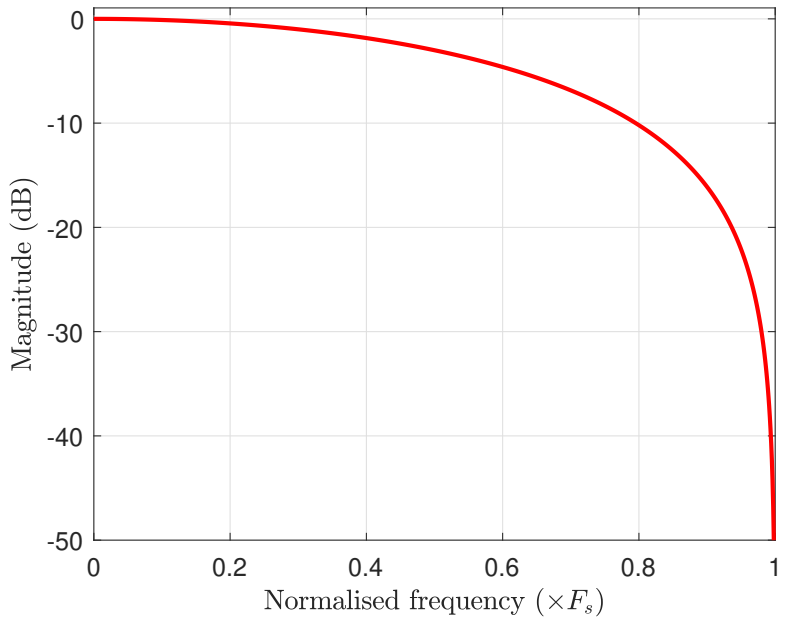

Figure 5.8: *The magnitude response of the LPF considered for band-limited channel simulation*

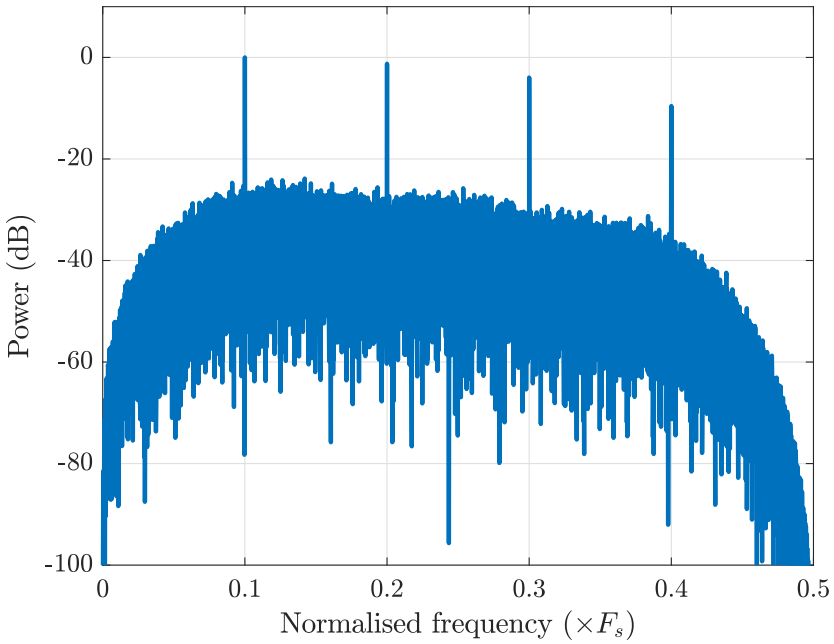

Figure 5.9: *A* PSD of 4-FSCM modulating signal (after the Hermitian symmetry and IFFT operation) after a LPF shown in Fig. 5.4

M, for all modulation orders, FSCM outperforms FSK. Moreover, the SNR required to achieve a given BER improves for FSCM but not for FSK.

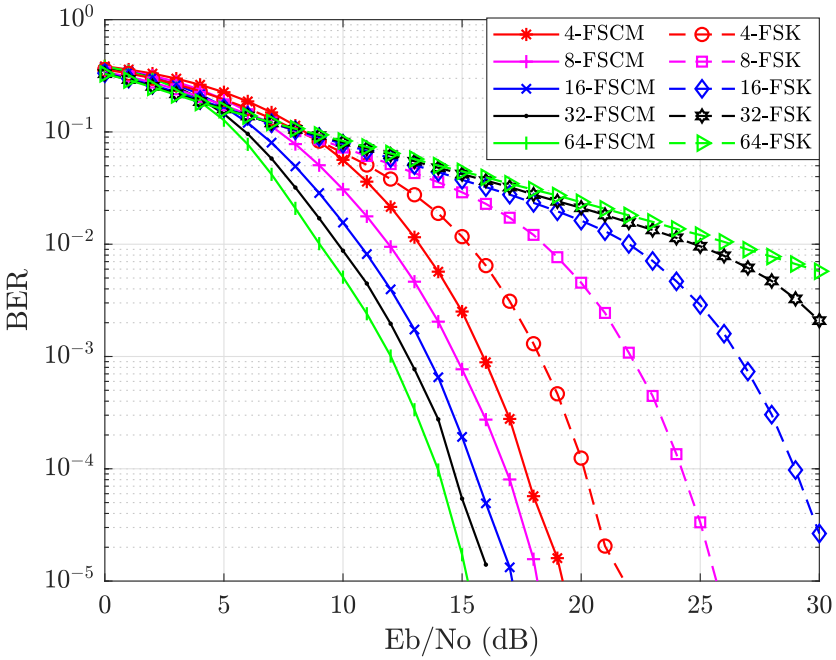

Figure 5.10: *Error performance of FSCM and FSK in a channel with limited bandwidth*

5.5 Energy and Spectral Efficiency Comparison

In FSCM, the number of bits that can be transmitted in a symbol duration T_s is $\log_2 M$. Therefore, the bit rate is $R_\mathrm{b} = \frac{\log_2 M}{T_\mathrm{s}} = \frac{\log_2 M}{M} B$. With that, the spectral efficiency in bits/s/Hz becomes:

$$\eta = \frac{\log_2 M}{M}. \tag{5.23}$$

This shows that increasing M does not lead to a linear increase in bit rate in FSCM. A high bandwidth is required for high data rate for a given M. Moreover, unlike QAM or PAM, the spectral efficiency decreases with higher modulation orders. However, this improves sensitivity (required SNR per bit) and with increasing M, the energy efficiency tends toward the lower bound of energy, *i.e.* −1.5917 dB. This makes FSCM a convenient scheme for low-power and low-rate applications.

An alternative way to compare energy and spectral efficiency of FSCM scheme with other modulation schemes is by using OOK as a reference. The amount of power required relative

to OOK to achieve a specific BER at a given bit rate, R_b can be used as a reference for other modulation schemes. This analysis of power efficiency is presented in the following subsection.

The BER of OOK is given as [155]:

$$\mathrm{BER}_\mathrm{OOK} = Q\left(\sqrt{\frac{E_\mathrm{b}}{N_0}}\right) = Q\left(\sqrt{\frac{P_{\mathrm{s,\ OOK}}}{N_0 R_\mathrm{b}}}\right). \tag{5.24}$$

And, solving for the signal power,

$$P_{\mathrm{s,\ OOK}} = N_0 R_\mathrm{b} \left(Q^{-1}\left(\mathrm{BER}_\mathrm{OOK}\right)\right)^2. \tag{5.25}$$

Similarly, the BER of M-PAM is given by [155]:

$$\mathrm{BER}_\mathrm{PAM} = 2\left(\frac{M-1}{M\log_2 M}\right) Q\left(\sqrt{\frac{6\log_2 M}{M^2-1}\frac{E_\mathrm{b}}{N_0}}\right). \tag{5.26}$$

In order to relate $\mathrm{BER}_\mathrm{PAM}$ to $\mathrm{BER}_\mathrm{OOK}$, (5.26) is further approximated to:

$$\mathrm{BER}_\mathrm{PAM} \approx Q\left(\sqrt{\frac{6\log_2 M}{M^2-1}\frac{E_\mathrm{b}}{N_0}}\right). \tag{5.27}$$

The approximation from (5.26) to (5.27) incurs relatively higher approximation error for larger M but decrease sharply when the SNR increases. Substituting $E_\mathrm{b} = P_{\mathrm{s,\ PAM}}/R_\mathrm{b}$, and solving for $P_{\mathrm{s,\ PAM}}$ gives:

$$P_{\mathrm{s,\ PAM}} = \left(\frac{M^2-1}{6\log_2 M}\right) N_0 R_\mathrm{b} \left(Q^{-1}\left(\mathrm{BER}_\mathrm{PAM}\right)\right)^2 \tag{5.28a}$$

$$= \left(\frac{M^2-1}{6\log_2 M}\right) P_{\mathrm{s,\ OOK}}. \tag{5.28b}$$

Equation (5.28b) gives the estimation of power required at a given bit rate for M-PAM relative to the OOK modulation scheme. The power requirement of 2-PAM is 3 dB lower than OOK but higher orders of PAM require more power than OOK.

For BPSK and quadrature phase shift keying (QPSK), the BER is given by [155]:

$$\mathrm{BER}_\mathrm{B|QPSK} = Q\left(\sqrt{\frac{2E_\mathrm{b}}{N_0}}\right) = Q\left(\sqrt{\frac{2P_{\mathrm{s,\ B|QPSK}}}{N_0 R_\mathrm{b}}}\right). \tag{5.29}$$

The amount of power requirement is thus:

$$P_{\mathrm{s,\ B|QPSK}} = \frac{1}{2} N_0 R_\mathrm{b} \left(Q^{-1}\left(\mathrm{BER}_{\mathrm{B|QPSK}}\right)\right)^2 \tag{5.30a}$$

$$= \frac{1}{2} P_{\mathrm{s,\ OOK}}. \tag{5.30b}$$

From (5.30b), BPSK and QPSK reduce the amount of power required by 3 dB relative to OOK.

For M-QAM, an approximation of its error probability can be estimated using (5.27) with the error probability of $\sqrt{M}$-PAM at half the total energy as:

$$\mathrm{BER}_{\mathrm{QAM}} \approx Q\left(\sqrt{\frac{3\log_2 M}{M-1}\frac{E_\mathrm{b}}{N_0}}\right). \tag{5.31}$$

The error due to the approximation is low for larger M and decrease sharply when the SNR increases. Similarly, the power requirement can be found as:

$$P_{\mathrm{s,\ QAM}} = \left(\frac{M-1}{3\log_2 M}\right) N_0 R_\mathrm{b} \left(Q^{-1}\left(\mathrm{BER}_{\mathrm{QAM}}\right)\right)^2 \tag{5.32a}$$

$$= \left(\frac{M-1}{3\log_2 M}\right) P_{\mathrm{s,\ OOK}}. \tag{5.32b}$$

While 4-QAM reduces the power by 3 dB relative to OOK, larger M-QAM come with more power requirement.

For FSCM, the exact BER is given by (5.21) which is approximated by (5.22). In order to compare the BER with OOK, (5.22) is approximated to the following expression:

$$\mathrm{BER}_{\mathrm{FSCM}} \approx Q\left(\sqrt{\log_2 M \frac{E_\mathrm{b}}{N_0}}\right) = Q\left(\sqrt{\log_2 M \frac{P_{\mathrm{s,\ FSCM}}}{N_0 R_\mathrm{b}}}\right). \tag{5.33}$$

The approximation error from using (5.33) instead of the exact (5.22) is relatively low for larger M and the error is infinitesimal at larger SNR. This is shown in Fig. 5.11 with very small errors for larger M which approaches to 0. Therefore, solving for $P_{\mathrm{s,\ FSCM}}$ from (5.33), the power requirement of FSCM compared to OOK can be determined by:

$$P_{\mathrm{s,\ FSCM}} = \frac{1}{\log_2 M} N_0 R_\mathrm{b} \left(Q^{-1}\left(\mathrm{BER}_{\mathrm{FSCM}}\right)\right)^2 \tag{5.34a}$$

$$= \frac{1}{\log_2 M} P_{\mathrm{s,\ OOK}}. \tag{5.34b}$$

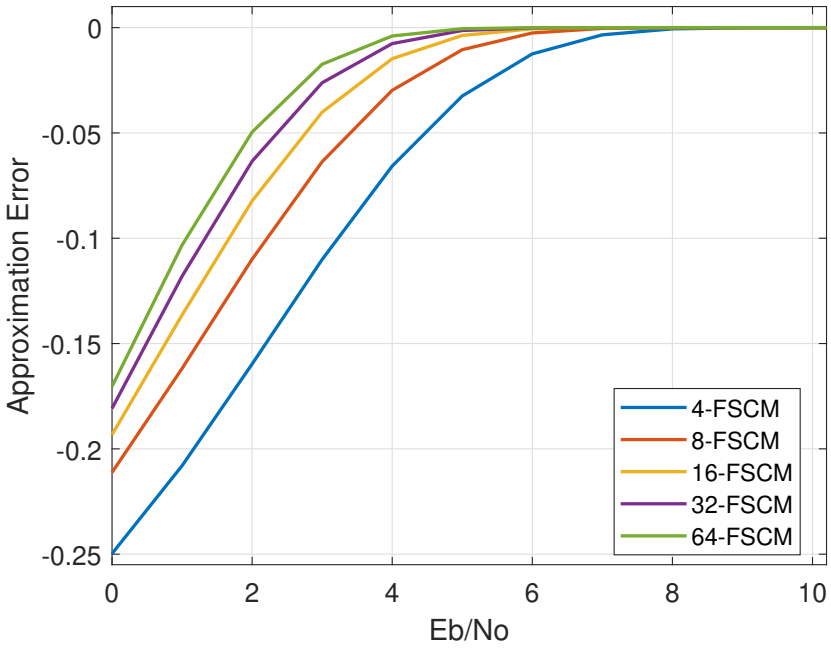

Figure 5.11: *BER approximation error of FSCM for* $M = [4, 8, 16, 32, 64]$ *due to using the approximated BER in* (5.33) *instead of the BER in* (5.22)

It is also possible to evaluate the the amount of power required to achieve the maximum bit rate given in (2.11) and use as a reference to other modulation schemes. The power to achieve the maximum possible bit rate is:

$$P_{\text{s, limit}} = N_0 B \left(2^{R_\text{b}/B} - 1\right). \tag{5.35}$$

Solving for N_0 from (5.25):

$$N_0 = \frac{P_{\text{s, OOK}}}{R_\text{b} \left(Q^{-1}\left(\text{BER}_\text{OOK}\right)\right)^2}, \tag{5.36}$$

and substituting in (5.35), the power requirement can be rewritten as:

$$P_{\text{s, limit}} = \frac{B/R_\text{b}}{\left(Q^{-1}\left(\text{BER}_\text{OOK}\right)\right)^2} \left(2^{R_\text{b}/B} - 1\right) P_{\text{s, OOK}}. \tag{5.37}$$

The summary of power (normalised to the power requirement of OOK) and the bandwidth efficiencies considering a given bit rate R_b at a specific BER is shown in Fig. 5.12. The FSCM

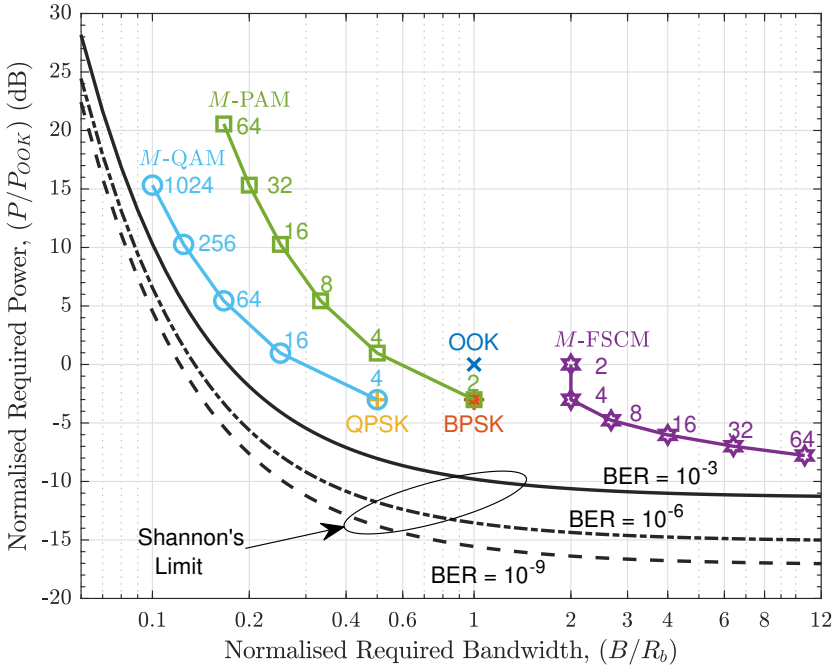

Figure 5.12: *Power and bandwidth efficiencies for various modulation schemes. The Shannon's limit is also shown at three different BER values.*

shows an improvement in terms of the amount of power required as the modulation order increases, relative to the power required in OOK. However, this is at the cost of larger bandwidth requirement. Therefore, sacrificing the spectral efficiency. The modulation schemes such as PAM and QAM, on the contrary, provide better spectral efficiency relative to the OOK, and improves as the modulation order increases. However, the amount of power required is higher than OOK and increases as the modulation order increases. The Shannon's limit relative to the OOK scheme is also shown at three different BER values $\left(10^{-3},\ 10^{-6},\ \text{and}\ 10^{-9}\right)$. The results indicate that at a specific relative power requirement, spectral efficiency increases as BER is reduced. Alternatively, at a specific spectral efficiency, power efficiency increases for lower BER values. Note that Fig. 5.12 relates to Fig. 2.10, but with one key difference. In Fig. 5.12, the power and bandwidth efficiencies for various modulation schemes are evaluated in relation to OOK, while Fig. 2.10 shows the spectral efficiency versus SNR per bit performance at a specific BER. The summary of this comparison is also provided Table 5.1.

Table 5.1: *Power and Bandwidth Efficiency Comparisons*

Modulation Scheme	Average Power	Relative Power (dB)	Bandwidth
OOK	$P_{\mathrm{s,\ OOK}}$	0	R_{b}
M-PAM	$\left(\frac{M^2-1}{6\log_2 M}\right) P_{\mathrm{s,\ OOK}}$	$10\log_{10}\left(\frac{M^2-1}{6\log_2 M}\right)$	$\frac{1}{\log_2 M} R_{\mathrm{b}}$
BPSK	$\frac{1}{2} P_{\mathrm{s,\ OOK}}$	-3.0103	R_{b}
QPSK	$\frac{1}{2} P_{\mathrm{s,\ OOK}}$	-3.0103	$\frac{1}{2} R_{\mathrm{b}}$
M-QAM	$\left(\frac{M-1}{3\log_2 M}\right) P_{\mathrm{s,\ OOK}}$	$10\log_{10}\left(\frac{M-1}{3\log_2 M}\right)$	$\frac{1}{\log_2 M} R_{\mathrm{b}}$
M-FSCM	$\frac{1}{\log_2 M} P_{\mathrm{s,\ OOK}}$	$-10\log_{10}\left(\log_2 M\right)$	$\frac{M}{\log_2 M} R_{\mathrm{b}}$

5.6 Experimental Demonstration

This section details the experimental setup and results that demonstrate FSCM-based VLC system and compare its performance with other conventional modulation schemes.

5.6.1 Experiment Setup

The system block diagram for the experiment demonstration with signal processing steps is shown in Fig. 5.13. In addition to the FSCM, FSK and BPSK schemes are tested and their performance is compared. For FSCM and FSK, a random stream of binary input is generated and mapped into FSCM and FSK symbols with modulation levels of $M = [4, 16, 64]$. A real-valued signal is generated by applying IFFT to the chirp waveform and its Hermitian symmetry. The minimum sample size of $N_{\mathrm{IFFT}} = 2(M+1)$ is used for FSCM and FSK while for BPSK $N_{\mathrm{IFFT}} = 64$ is used. The serial time-domain signal is then pulse-shaped using the RRC filter with an upsampling factor of 4 sample per symbol and loaded to an arbitrary waveform generator (AWG: Keysight 81180A). The output of the AWG superimposed with the DC bias current from the bias-tee (Bias-Tee: Mini-Circuits ZFBT-4R2GW+) modulates the LED (150505BS73300). Aspheric condenser lenses (Thorlabs ACL4532) are used to collimate the output light from the LED and focus it into the active area of the photodetector. On the receiver side, a photodetector receiver (PD: ThorLabs PDA10A) detects the intensity modulated signal

and is captured by an oscilloscope (OSC: Keysight MSO7104B). Then the received signal is demodulated to recover the transmitted information bits.

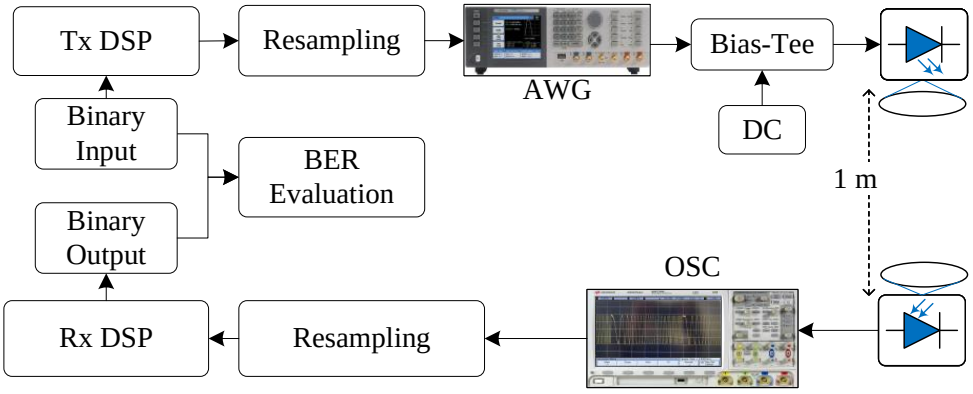

Figure 5.13: *Experimental setup with signal processing steps. Details of transmitter and receiver DSPs are shown in Fig. 5.6. Note that the chirp waveform displayed on the oscilloscope is captured in real-time when an analogue signal is transmitted.*

5.6.2 Results and Discussion

To investigate BER at different transmission rates, the sampling rate of the AWG is set to $[0.4, 0.8, 1.2, 1.6]$ GSa/s with the modulation signal depth, (peak-to-peak voltage, Vpp) ranging from 50 mV to 1 V. The DC bias is set to 20 mA at which the -3 dB modulation bandwidth is around 7 MHz while the optical power is 6 mW. When comparing the achievable data rate, the 7% HD-FEC threshold BER of 3.8×10^{-3} is considered.

The BER versus Vpp performance of BPSK at different bit rates is shown in Fig. 5.14. As expected, the BER improves as Vpp increases which is related to an increase in SNR. With BPSK, a 200 Mb/s bit rate can be achieved under the target BER at 400 mV. By increasing the order of PSK, a higher data rate can be obtained but at larger SNR per bit. Therefore, only BPSK results is shown in this work.

In Fig. 5.15, the BER performance of FSK at 300 MSa/s is shown. The BER performance improves as M is decreased from 64 to 4. This agrees with the simulation results in Fig. 5.10 for a channel with limited bandwidth. The reason is that when M increases under the same modulation bandwidth, the separation frequency between consecutive symbols, given by $\Delta f = F_{\text{sample}}/N_{\text{IFFT}} = [30, 8.82, 2.31]$ MHz, decreases with $M = [4, 16, 64]$, respectively. That

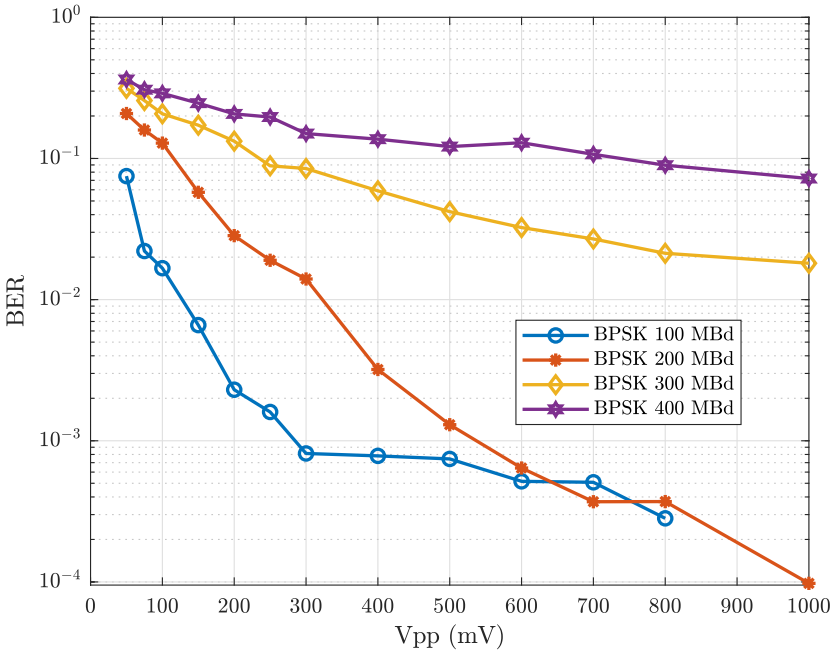

Figure 5.14: *BER performance of BPSK scheme at different transmission rates ranging from 100 MBd to 500 MBd*

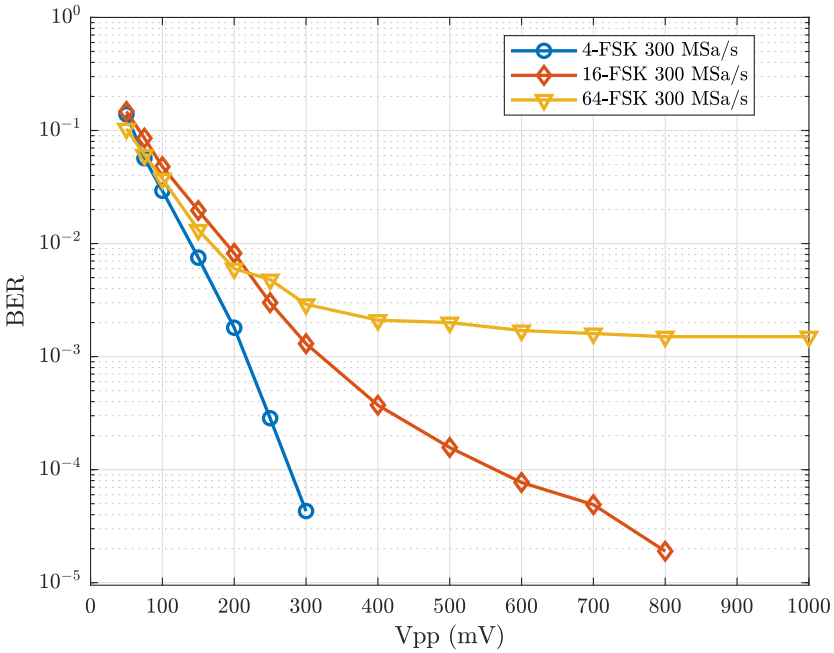

Figure 5.15: *BER performance of FSK scheme with* $M = [4, 16, 64]$ *at 300 MSa/s achieving* $R_\mathrm{b} = [150, 75, 28.125]$ *Mb/s for each modulation order, respectively*

leads to intersymbol interference and thus erroneous reception in 64-FSK than in 4-FSK. Overall, a bit rate of $R_\mathrm{b} = [150, 75, 28.125]$ Mb/s can be achieved under the target BER with a requirement of Vpp = $[200, 250, 300]$ mV for $M = [4, 16, 64]$ FSK, respectively.

The transmission at 300 MSa/s is repeated for FSCM and the result is shown in Fig. 5.16. Unlike the FSK, in FSCM the performance improves with increasing M, which consolidates the simulation result shown in Fig. 5.10. This is because in FSCM a symbol is represented by M samples allocated in all frequencies, and the reduction in separation frequency has relatively lower impact on its performance. This is an important characteristic to have for an energy-efficient system as increasing M improves the BER at lower SNR. To evaluate the achievable

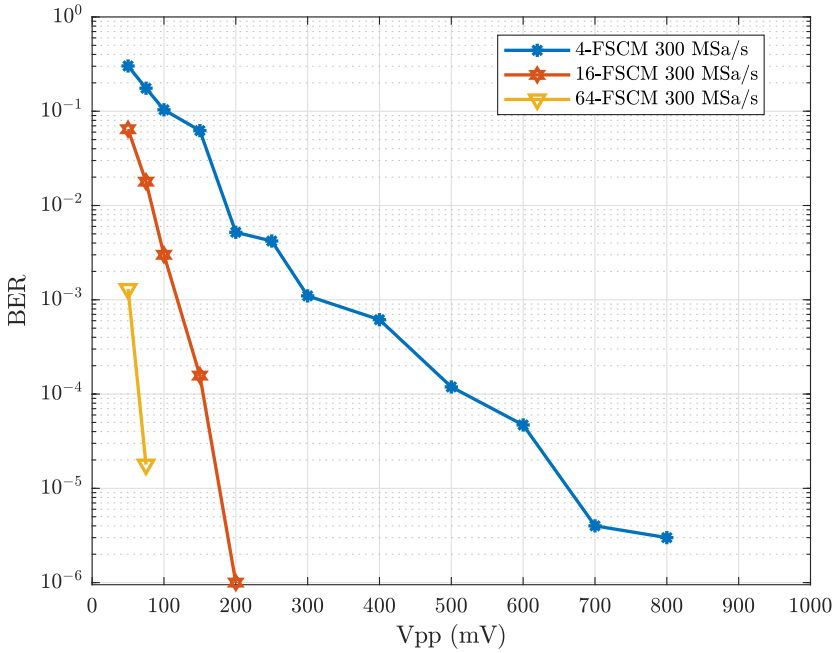

Figure 5.16: *BER performance of FSCM with* $M = [4, 16, 64]$ *at 300 MSa/s resulting* $R_\mathrm{b} = [150, 75, 28.125]$ *Mb/s for each modulation order, respectively*

data rate of the system with FSCM, the experiment is repeated at 400 MSa/s and the result is shown in Fig. 5.17. Using FSCM with $M = [4, 16, 64]$ a bit rate of $R_\mathrm{b} = [200, 100, 37.5]$ Mb/s can be achieved for each modulation order, respectively.

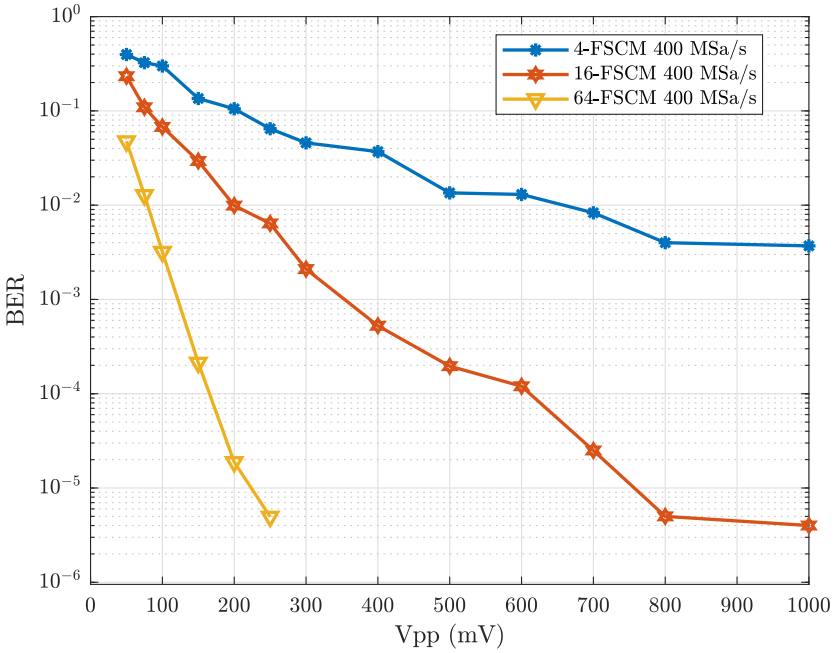

Figure 5.17: *BER performance of FSCM with* $M = [4, 16, 64]$ *at 400 MSa/s achieving* $R_{\mathrm{b}} = [200, 100, 37.5]$ *Mb/s for each modulation order, respectively*

The summary of the achieved data rate versus the required Vpp under the target BER is shown in Fig. 5.18. The BPSK and 4-FSCM achieve the highest data rate while BPSK comes with

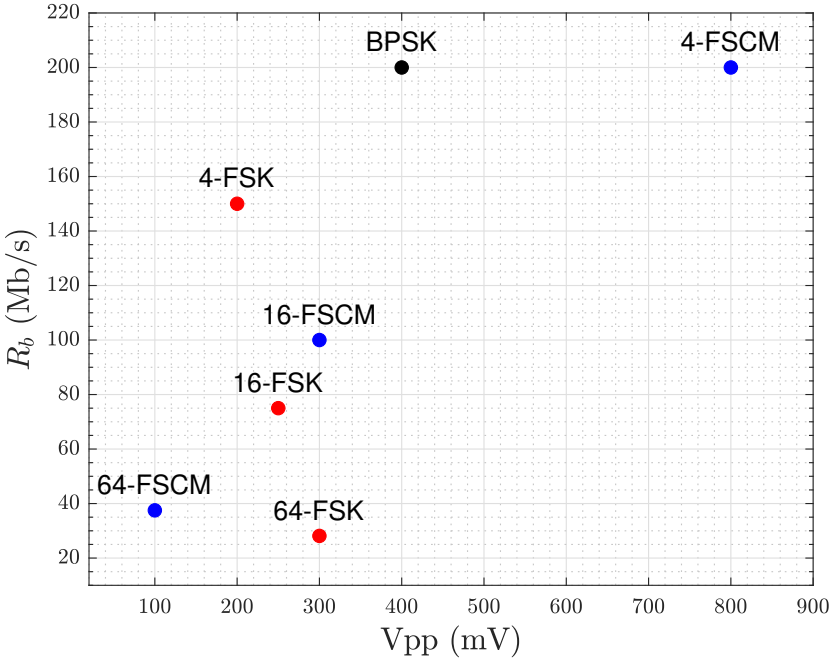

Figure 5.18: *Summary of experiment result showing the bit rate and Vpp trade-off*

the reduction of Vpp. However, in FSCM, the increasing M improves the energy efficiency (*i.e.* the amount of Vpp required to achieve the target BER) of the system and 64-FSCM is the most energy efficient of all schemes under test. In FSK, the Vpp requirement increases with increasing M. In terms of transmission rate, a higher bit rate under the target BER is demonstrated in FSCM which is 200 Mb/s while only 150 Mb/s is the highest in FSK.

5.7 Summary

In this chapter, an energy-efficient frequency shift chirp modulation technique compatible with VLC systems is presented. A theoretical framework of FSCM is provided, including the modulation and demodulation processes and the error performance, as well as a proof-of-concept experiment. It is shown to be a promising modulation technique for VLC systems to improve energy efficiency.

The error performance of FSCM in noise-limited and frequency-selective channels with limited modulation bandwidth is analysed, and the results are validated through simulations. FSCM is shown to be different from FSK, as symbols are mapped to a range of frequencies within the available bandwidth, allowing for a reduction in the impact of the frequency-selective channel and improving system performance.

A proof-of-concept experiment is also conducted to demonstrate the use of FSCM in a VLC system and compare its performance to other conventional modulation schemes. In the experiment, it is shown that FSCM can be used to realise an energy-efficient VLC system, with 64-FSCM being the most energy efficient of all the schemes tested. In terms of transmission rate, a higher bit rate of 200 Mb/s is demonstrated for FSCM, compared to the highest rate of 150 Mb/s in FSK.

FSCM is characterised by improved error performance with increasing the modulation order, which also represents the number of samples allocated in all frequencies for each symbol. Therefore, the increase of modulation order improves the energy efficiency of the system, as it results in a lower target BER at lower SNR. However, it also results in a lower data rate. The potential application of FSCM in low-power and low-rate networks makes it a promising option for the integration of VLC in various systems. Overall, the results presented in this chapter provide a strong case for the use of FSCM in VLC systems.

Chapter 6
Conclusion and Outlook

In this chapter, a summary of the research presented in this thesis is presented. The main findings of the research will be highlighted, along with relevant conclusions. In addition, an outline of the limitations of this research work will be provided. Based on these limitations, potential areas for future research will be recommended.

6.1 Summary of the Work

There has been a significant increase in data traffic recently, which has led to the exploration of using optical frequencies to supplement RF-based wireless communication systems. One promising technology in this area is VLC, which transmits data using LEDs over the visible light spectrum and utilises existing lighting infrastructure for communication. VLC is a popular choice for short-range wireless connectivity because it is energy efficient, low cost, and has a widespread availability of front-end devices. However, one of the main challenges in designing and optimising a VLC system is improving its energy and spectral efficiency. To address this challenge, the objective of this thesis is to explore techniques and identify the most effective approaches for enhancing the energy and spectral efficiency of VLC systems. To achieve this goal, new signal processing techniques are developed, and their effectiveness is evaluated through a combination of theoretical analysis, simulations, and experimental demonstrations.

A comprehensive overview of the VLC system relevant to the thesis is provided in Chapter 2. It highlights the many advantages of VLC for various communication applications, including a large, unlicensed spectrum in the optical domain, free from electromagnetic interference, inherent security and spatial reuse, ease of implementation, and low cost. The chapter describes some potential application areas for VLC, including indoor wireless communication, underwater communication, indoor localisation, and vehicular communication. However, several challenges must be addressed to fully realise the potential of VLC, including the limited modulation bandwidth of LEDs, which impacts the efficiency of VLC systems, and the nonlinear

response of LEDs. The chapter also provides background information on the system components of VLC, including the optical transmitters and receivers used to transmit and receive optical signals, as well as the VLC channel model. It covers various modulation techniques used in VLC, such as pulse modulation techniques (OOK, PAM, and PPM) and optical OFDM. The chapter emphasises the importance of energy and spectral efficiency in the design of VLC systems, as maximising the use of available bandwidth and minimising energy consumption can help achieve high data rates and long-distance communication. In this regard, the chapter introduces probabilistic shaping as a technique to improve the performance of high-speed VLC systems by optimising the signal distribution. PS allows for continuous and adaptive entropy transmission, which is particularly useful for optical OFDM-based VLC systems. The chapter also includes a comparative discussion of related literature on techniques to improve the limited modulation bandwidth of LEDs, utilise adaptive information loading with PS, and implement energy-efficient modulation schemes for low-power applications.

The characteristics of an LED are studied in relation to the DC bias point, including its optical power response and modulation bandwidth. Chapter 3 examines the optimisation of the bias point in order to increase capacity by enhancing the modulation bandwidth at higher driving currents while minimising signal distortion. Two methods are proposed: one allows the input signal to enter the saturation region of the LED, which leads to an increase in the modulation bandwidth but also causes nonlinear distortion that reduces the SNR. The other method constrains the input signal to the LED's linear operating range, avoiding nonlinear distortion but potentially limiting the increase in the modulation bandwidth. Simulation results and a PAM-based VLC experiment both demonstrate that the optimal bias point is found beyond the midpoint of the LED's dynamic range. These results suggest that the capacity of a VLC system can be optimised by properly selecting the DC bias point, taking into account the impact on the SNR and modulation bandwidth. These optimisation techniques, when combined with other approaches, have the potential to significantly improve the capabilities of a VLC system.

In Chapter 4, the use of probabilistic shaping in VLC systems is examined. This technique optimises the distribution of source symbols for the VLC channel and has the potential to significantly enhance the system's performance. The symbol error performance of PS is analysed using a maximum a posteriori detector and closed-form analytical expressions are provided and validated through Monte Carlo simulations. A framework is also presented that demonstrates how PS can be used to trade energy efficiency for spectral efficiency and how the design pa-

rameters can be chosen. The results show that PS outperforms the use of a uniform distribution and significantly reduces the required SNR to achieve a certain error probability. The practicality of this approach is demonstrated through two proof-of-concept experiments, in which the achievable rates of PS are compared to those of the conventional adaptive bit-power loading technique. Unlike the bit-power loading optimisation method, PS provides continuous entropy loading, allowing for efficient use of the available bandwidth beyond the −3 dB point and allowing for transmission rates close to channel capacity limits. In the first experiment, using a single low-power LED, PS resulted in an aggregate achievable information rate of 1.13 Gbps, which is 27.13% higher than the rate achieved with the bit-power loading technique. In the second experiment, using a WDM-based VLC system with three independently modulated LEDs, PS resulted in an aggregate achievable information rate of 10.81 Gbps, 25.7% higher than with the bit-power loading approach. Overall, VLC with PS has been shown to be a reliable way to increase spectral efficiency and data rates, and its symbol error performance outperforms that of a uniform distribution by requiring a lower SNR to achieve a certain error probability. This technique has also been demonstrated to significantly increase achievable information rates compared to adaptive bit-power loading. These findings suggest that PS has the potential to be utilised in VLC systems to maximise information rate and approach capacity limits.

An energy-efficient frequency shift chirp modulation technique that is compatible with VLC systems has been introduced in Chapter 5. The theoretical foundation of FSCM, including its modulation and demodulation processes, is presented. The error performance of this technique is also analysed in noise-limited and frequency-selective channels, demonstrating better energy efficiency compared to other equivalent modulation techniques. A proof-of-concept experiment is conducted to demonstrate that FSCM can be used to create an energy-efficient VLC system. This technique is characterised by improved error performance as the modulation order increases, as it is an orthogonal modulation scheme like FSK. However, unlike FSK, symbols in FSCM are mapped to a range of frequencies within the available bandwidth, which allows for resilience in band-limited frequency-selective channels. The potential application of FSCM in low-power and low-rate networks makes it a promising option for VLC system integration.

Overall, this thesis has focused on the development and evaluation of techniques to optimise the spectral and energy efficiency of VLC systems. Through the introduction of a framework identifying optimal operating conditions and the use of signal shaping and energy-efficient modulation techniques, it is possible to significantly improve the capacity and performance

of VLC systems. The approaches described in this thesis provide a promising direction for enhancing the efficiency of VLC systems and can potentially lead to more widespread adoption of this technology.

6.2 Limitations and Recommendations for Future Work

This study has contributed to the understanding and enhancement of energy and spectrum efficiency in VLC. However, there are several factors that may have limited the scope and extent of the findings. In this section, the limitations of the study will be discussed. In addition, suggestions for future research to build upon and address the remaining questions will be made.

The results reported in this thesis are subject to variability in the devices and link environment, which may lead to different values if the experiments were to be repeated. To ensure the reproducibility of this thesis, it is essential to consider the impact of device variability and the implementation of signal processing techniques. To facilitate replication of the work and comparison of results, the part numbers of all devices used in the experiments have been provided. Moreover, all measurements have been taken with as many data sample points as possible, using the maximum memory depth of the devices, to ensure statistically representative data transmission for robust characterisation of the communication link. It is also crucial to emphasise the need for calibration of the setup to ensure an accurate alignment between an LED and a PD of a VLC system, which is essential to optimise the system performance.

One limitation of this study is that it only focused on the communication aspect of LED-based VLC systems and did not consider the impact of communication techniques on lighting performance. To address this limitation, future research could explore the optimisation of both communication and lighting performance in LED-based systems. This could involve investigating different modulation techniques and the DC bias optimisation that could balance the requirements of both applications. By considering both aspects of LED-based systems, a more comprehensive understanding of their potential benefits and limitations can be gained.

A framework for optimising the capacity of a VLC system through bias point optimisation is presented in Chapter 3. In the simulation results presented, realistic parameters of the LED and photodetector, which are measured in experiments, are used. However, an ideal channel DC gain is assumed in the analysis. The channel gain value has a significant impact on the SNR and therefore the capacity of the system. Other sources of distortion that could affect

the modulated signal and its proper detection are not considered. As a result, it is assumed that the modulating signal bandwidth is less than the LED bandwidth. In addition, only the line-of-sight link is considered in the analysis, as it is typically the dominant link in a LiFi system and the signal power from non-line-of-sight paths is much smaller in comparison. The optimal bias point will depend on various factors such as the distance and orientation between the transmitter and receiver, as well as any obstacles in the path between them. To accurately estimate these optimal bias points, knowledge of the channel state information, including the LoS and NLoS channel gains, is needed. However, it should be noted that the channel gain is simply a scaling factor in the SNR expression and does not affect the validity of the optimisation process. This means that while the absolute optimal operating points may differ for different users, the process for obtaining these optimal points remains the same.

One possible research area for future research is the combination of bias point optimisation techniques with pre/post equalisation and precoding/pre-distortion. By combining the bias point optimisation methods discussed in this thesis with pre/post equalisation and precoding/pre-distortion, the performance of the VLC system can be further enhanced. Pre/post equalisation can be used to mitigate intersymbol interference in the system, while precoding/pre-distortion can compensate for nonlinearities. By exploring the use of these techniques in combination with bias point optimisation, future research can significantly improve the capabilities and performance of VLC systems.

The research presented in Chapter 4 explores the use of PS in VLC. PS is a relatively new technique that is being actively researched and developed in various communication fields and has the potential to significantly improve the performance of VLC system, making it more competitive with other forms of communication. However, the effectiveness of this process depends on the distribution matcher. In this thesis, a constant composition distribution matcher (CCDM) is used in all studies. CCDM generates amplitude sequences with a fixed composition based on the Maxwell-Boltzmann distribution. Therefore, the distribution matcher determines the optimal distribution of symbols based on the desired rate parameter and channel conditions. Despite ongoing efforts to develop distribution matchers with low storage and computational complexity, current state-of-the-art distributions are still far from achieving this goal. The CCDM, in particular, uses arithmetic coding and has high computational complexity. This is particularly impactful in multicarrier modulation techniques such as OFDM. For optical OFDM employed in this work, each subcarrier is assigned different entropy values, and as a result, each

subcarrier has a unique symbol distribution that requires an independent distribution matcher and dematcher, greatly increasing complexity. Therefore, further research in the development of distribution matchers with low storage and computational complexity could be beneficial. This may require interdisciplinary study in the fields of information theory and digital signal processing. Such research could potentially result in more efficient and effective distribution matchers that could be applied to various communication technologies, including VLC systems.

The theoretical error performance analysis of probabilistically shaped symbols presented in this work is based on the symbol error rate (SER). Therefore, it is independent of the choice of bits-to-symbol distribution matcher. However, if the bit error rate (BER) of probabilistically shaped symbols is to be evaluated, the implementation of the chosen distribution matcher should be taken into account, as it depends on the specific matcher used. Furthermore, the distribution dematcher is sensitive to errors and typically requires a forward error correction (FEC). This involves the use of FEC encoding in conjunction with the PS distribution matcher at the transmitter and FEC decoding with the distribution dematcher at the receiver. The order in which shaping and coding are applied in the transmitter and receiver is an open research question that could be explored in the future. Therefore, it would be valuable to investigate the BER performance of probabilistically shaped symbols. This could involve exploring the impact of different distribution matchers and FEC schemes, as well as determining the optimal combination of shaping and coding rates to maximise SNR gain.

The frequency shift chirp modulation (FSCM) introduced in Chapter 5 is designed to provide an energy-efficient modulation technique for use in low-power, low-rate VLC networks, particularly in the IoT. The theoretical basis of FSCM has been established and the concept has been demonstrated in an experiment. However, the experimental demonstration was carried out using discrete lab components, such as a signal generator and an oscilloscope, and the signal generation/detection is carried out in offline signal processing. While this can serve as a proof-of-concept demonstration, one potential area of future research could be a real-time implementation of FSCM-based VLC using a FPGA. This approach could potentially offer benefits for low-power, low-rate applications and could be a valuable addition to the field of VLC. In this implementation, it will be important to consider issues such as power consumption and cost, as well as potential applications for this technology. Overall, the development and implementation of FSCM-based VLC systems using FPGA could lead to significant advances in the field and could have a wide range of practical applications.

References

[1] H. Haas, "LiFi is a paradigm-shifting 5G technology," *Reviews in Physics*, vol. 3, pp. 26–31, 2018.

[2] K. David and H. Berndt, "6G vision and requirements: Is there any need for beyond 5G?," *IEEE vehicular technology magazine*, vol. 13, no. 3, pp. 72–80, 2018.

[3] A. Dogra, R. K. Jha, and S. Jain, "A survey on beyond 5G network with the advent of 6G: Architecture and emerging technologies," *IEEE Access*, vol. 9, pp. 67512–67547, 2020.

[4] T. Barnett Jr, S. Director, S. Jain, U. Andra, and T. Khurana, "Cisco Visual Networking Index (VNI) Complete Forecast Update, 2017–2022," (White Paper), Cisco, 2018.

[5] Ericsson, "Ericsson Mobility Report, November. 2022." [Online]. Available: `https://www.ericsson.com/en/reports-and-papers/mobility-report`. [Accessed 04-Jan-2023].

[6] L. E. M. Matheus, A. B. Vieira, L. F. Vieira, M. A. Vieira, and O. Gnawali, "Visible light communication: concepts, applications and challenges," *IEEE Communications Surveys & Tutorials*, vol. 21, no. 4, pp. 3204–3237, 2019.

[7] M. Kavehrad, "Optical wireless applications: A solution to ease the wireless airwaves spectrum crunch," in *Broadband Access Communication Technologies Vii*, vol. 8645, pp. 109–115, SPIE, 2013.

[8] Z. Ghassemlooy, W. Popoola, and S. Rajbhandari, *Optical wireless communications: system and channel modelling with MATLAB®*. CRC press, 2019.

[9] H. Haas, L. Yin, Y. Wang, and C. Chen, "What is LiFi?," *Journal of lightwave technology*, vol. 34, no. 6, pp. 1533–1544, 2015.

[10] S. Dimitrov and H. Haas, *Principles of LED light communications: towards networked Li-Fi*. Cambridge University Press, 2015.

[11] C. E. Shannon, "A mathematical theory of communication," *Bell system technical journal*, vol. 27, no. 3, pp. 379–423, 1948.

[12] F. Buchali, F. Steiner, G. Böcherer, L. Schmalen, P. Schulte, and W. Idler, "Rate adaptation and reach increase by probabilistically shaped 64-QAM: An experimental demonstration," *Journal of Lightwave Technology*, vol. 34, no. 7, pp. 1599–1609, 2016.

[13] Y. Du, W. Chen, K. Cui, Z. Guo, G. Wu, and X. Ren, "An exploration of the military defense system of the Ming Great Wall in Qinghai Province from the perspective of castle-based military settlements," *Archaeological and Anthropological Sciences*, vol. 13, no. 3, pp. 1–18, 2021.

[14] G. J. Holzmann and W. S. Lieberman, *Design and validation of computer protocols*, vol. 512. Prentice hall Englewood Cliffs, 1991.

[15] J.-M. Dilhac, "The telegraph of claude chappe-an optical telecommunication network for the xviiith century," *Institut National des Sciences Appliquées de Toulouse*, pp. 1–8, 2001.

[16] F. R. Gfeller and U. Bapst, "Wireless in-house data communication via diffuse infrared radiation," *Proceedings of the IEEE*, vol. 67, no. 11, pp. 1474–1486, 1979.

[17] IrDA, "Infrared Data Association (IrDA)," 2022. https://www.irda.org/.

[18] Y. Tanaka, T. Komine, S. Haruyama, and M. Nakagawa, "Indoor visible light data transmission system utilizing white LED lights," *IEICE transactions on communications*, vol. 86, no. 8, pp. 2440–2454, 2003.

[19] Y. Tanaka, S. Haruyama, and M. Nakagawa, "Wireless optical transmissions with white colored LED for wireless home links," in *11th IEEE International Symposium on Personal Indoor and Mobile Radio Communications. PIMRC 2000. Proceedings (Cat. No. 00TH8525)*, vol. 2, pp. 1325–1329, IEEE, 2000.

[20] *IEEE Standard for Local and Metropolitan Area Networks–Part 15.7: Short-Range Wireless Optical Communication Using Visible Light*, 2011.

[21] *IEEE Standard for Local and metropolitan area networks–Part 15.7: Short-Range Optical Wireless Communications*, 2019.

[22] T. Koonen, "Indoor Optical Wireless Systems: Technology, Trends, and Applications," *Journal of Lightwave Technology*, vol. 36, no. 8, pp. 1459–1467, 2018.

[23] D. Karunatilaka, F. Zafar, V. Kalavally, and R. Parthiban, "LED based indoor visible light communications: State of the art," *IEEE Communications Surveys & Tutorials*, vol. 17, no. 3, pp. 1649–1678, 2015.

[24] T. Cogalan and H. Haas, "Why would 5G need optical wireless communications?," in *2017 IEEE 28th Annual International Symposium on Personal, Indoor, and Mobile Radio Communications (PIMRC)*, pp. 1–6, IEEE, 2017.

[25] C.-W. Chow, C. Yeh, Y. Liu, and Y. Liu, "Improved modulation speed of LED visible light communication system integrated to main electricity network," *Electronics letters*, vol. 47, no. 15, pp. 867–868, 2011.

[26] J. Hecht, "Changing the lights: Are LEDs ready to become the market standard?," *Optics and Photonics News*, vol. 23, no. 3, pp. 44–50, 2012.

[27] R. Haitz, "Haitz's law," *Nature Photon*, vol. 1, no. 23, pp. 1–309, 2007.

[28] R. Haitz, F. Kish, J. Tsao, and J. Nelson, "The case for a national research program on semiconductor lighting," *Optoelectronics Industry Development Association*, pp. 1–24, 1999.

[29] I. T. U. (ITU), "Nomenclature of the frequency and wavelength bands used in telecommunications," *Recommendation ITU/RV*, pp. 431–438, 2015.

[30] H. Haas, "High-speed wireless networking using visible light," *Spie Newsroom*, vol. 1, no. 1, pp. 1–3, 2013.

[31] H. Burchardt, N. Serafimovski, D. Tsonev, S. Videv, and H. Haas, "VLC: Beyond point-to-point communication," *IEEE Communications Magazine*, vol. 52, no. 7, pp. 98–105, 2014.

[32] S. U. Rehman, S. Ullah, P. H. J. Chong, S. Yongchareon, and D. Komosny, "Visible light communication: a system perspective — overview and challenges," *Sensors*, vol. 19, no. 5, p. 1153, 2019.

[33] J. Classen, D. Steinmetzer, and M. Hollick, "Opportunities and pitfalls in securing visible light communication on the physical layer," in *Proceedings of the 3rd workshop on visible light communication systems*, pp. 19–24, 2016.

[34] A. Jovicic, J. Li, and T. Richardson, "Visible light communication: opportunities, challenges and the path to market," *IEEE communications magazine*, vol. 51, no. 12, pp. 26–32, 2013.

[35] J. M. Kahn and J. R. Barry, "Wireless infrared communications," *Proceedings of the IEEE*, vol. 85, no. 2, pp. 265–298, 1997.

[36] M. Kavehrad, "Sustainable energy-efficient wireless applications using light," *IEEE Communications Magazine*, vol. 48, no. 12, pp. 66–73, 2010.

[37] O. Ergul, E. Dinc, and O. B. Akan, "Communicate to illuminate: State-of-the-art and research challenges for visible light communications," *Physical Communication*, vol. 17, pp. 72–85, 2015.

[38] D. Tsonev, S. Videv, and H. Haas, "Towards a 100 Gb/s visible light wireless access network," *Optics express*, vol. 23, no. 2, pp. 1627–1637, 2015.

[39] G. Li, F. Hu, P. Zou, C. Wang, G.-R. Lin, and N. Chi, "Beyond 10 Gbps 450-nm GaN laser diode based visible light communication system utilizing probabilistic shaping bit loading scheme," in *2020 12th International Symposium on Communication Systems, Networks and Digital Signal Processing (CSNDSP)*, pp. 1–4, IEEE, 2020.

[40] M. S. Islim, R. X. Ferreira, X. He, E. Xie, S. Videv, S. Viola, S. Watson, N. Bamiedakis, R. V. Penty, I. H. White, *et al.*, "Towards 10 Gb/s orthogonal frequency division multiplexing-based visible light communication using a GaN violet micro-LED," *Photonics Research*, vol. 5, no. 2, pp. A35–A43, 2017.

[41] D. Tsonev, H. Chun, S. Rajbhandari, J. J. McKendry, S. Videv, E. Gu, M. Haji, S. Watson, A. E. Kelly, G. Faulkner, *et al.*, "A 3-Gb/s Single-LED OFDM-Based Wireless VLC Link Using a Gallium Nitride μLED," *IEEE Photonics Technology Letters*, vol. 26, no. 7, pp. 637–640, 2014.

[42] X. Huang, S. Chen, Z. Wang, J. Shi, Y. Wang, J. Xiao, and N. Chi, "2.0-Gb/s visible light link based on adaptive bit allocation OFDM of a single phosphorescent white LED," *IEEE Photonics Journal*, vol. 7, no. 5, pp. 1–8, 2015.

[43] M.-A. Khalighi, C. Gabriel, T. Hamza, S. Bourennane, P. Leon, and V. Rigaud, "Underwater wireless optical communication; recent advances and remaining challenges," in *2014 16th International Conference on Transparent Optical Networks (ICTON)*, pp. 1–4, IEEE, 2014.

[44] W. Popoola, E. Guler, J. Wang, and C. Geldard, "Gbps underwater optical wireless communication in turbulence and random sea surface," in *Proceedings of the Workshop on Internet of Lights*, pp. 21–26, 2021.

[45] H. M. Oubei, J. R. Duran, B. Janjua, H.-Y. Wang, C.-T. Tsai, Y.-C. Chi, T. K. Ng, H.-C. Kuo, J.-H. He, M.-S. Alouini, *et al.*, "4.8 Gbit/s 16-QAM-OFDM transmission based on compact 450-nm laser for underwater wireless optical communication," *Optics express*, vol. 23, no. 18, pp. 23302–23309, 2015.

[46] T.-C. Wu, Y.-C. Chi, H.-Y. Wang, C.-T. Tsai, and G.-R. Lin, "Blue laser diode enables underwater communication at 12.4 Gbps," *Scientific reports*, vol. 7, no. 1, pp. 1–10, 2017.

[47] J. Du, Y. Wang, C. Fei, R. Chen, G. Zhang, X. Hong, and S. He, "Experimental demonstration of 50-m/5-Gbps underwater optical wireless communication with low-complexity chaotic encryption," *Optics Express*, vol. 29, no. 2, pp. 783–796, 2021.

[48] J. Chen, C. T. Geldard, E. Guler, A. Hamilton, and W. O. Popoola, "An Experimental Demonstration of FSK-SIM-PDM Underwater Optical Wireless Communications," in *2022 Sixth Underwater Communications and Networking Conference (UComms)*, pp. 1–4, IEEE, 2022.

[49] C. T. Geldard, E. Guler, A. Hamilton, and W. O. Popoola, "An Empirical Comparison of Modulation Schemes in Turbulent Underwater Optical Wireless Communications," *Journal of Lightwave Technology*, vol. 40, no. 7, pp. 2000–2007, 2021.

[50] J. Armstrong, Y. A. Sekercioglu, and A. Neild, "Visible light positioning: A roadmap for international standardization," *IEEE Communications Magazine*, vol. 51, no. 12, pp. 68–73, 2013.

[51] Y.-S. Kuo, P. Pannuto, K.-J. Hsiao, and P. Dutta, "Luxapose: Indoor positioning with mobile phones and visible light," in *Proceedings of the 20th annual international conference on Mobile computing and networking*, pp. 447–458, 2014.

[52] J. Luo, L. Fan, and H. Li, "Indoor positioning systems based on visible light communication: State of the art," *IEEE Communications Surveys & Tutorials*, vol. 19, no. 4, pp. 2871–2893, 2017.

[53] Y. Zhuang, L. Hua, L. Qi, J. Yang, P. Cao, Y. Cao, Y. Wu, J. Thompson, and H. Haas, "A survey of positioning systems using visible LED lights," *IEEE Communications Surveys & Tutorials*, vol. 20, no. 3, pp. 1963–1988, 2018.

[54] C. Bergenhem, E. Hedin, and D. Skarin, "Vehicle-to-vehicle communication for a platooning system," *Procedia-Social and Behavioral Sciences*, vol. 48, pp. 1222–1233, 2012.

[55] T. Yamazato, A. Ohmura, H. Okada, T. Fujii, T. Yendo, S. Arai, and K. Kamakura, "Range estimation scheme for integrated I2V-VLC using a high-speed image sensor," in *2016 IEEE International Conference on Communications Workshops (ICC)*, pp. 326–330, IEEE, 2016.

[56] P. Papadimitratos, A. De La Fortelle, K. Evenssen, R. Brignolo, and S. Cosenza, "Vehicular communication systems: Enabling technologies, applications, and future outlook on intelligent transportation," *IEEE communications magazine*, vol. 47, no. 11, pp. 84–95, 2009.

[57] T. Cogalan, S. Videv, and H. Haas, "Inflight connectivity: Deploying different communication networks inside an aircraft," in *2018 IEEE 87th Vehicular Technology Conference (VTC Spring)*, pp. 1–6, IEEE, 2018.

[58] H. Ma, L. Lampe, and S. Hranilovic, "Integration of indoor visible light and power line communication systems," in *2013 IEEE 17th International Symposium on Power Line Communications and Its Applications*, pp. 291–296, IEEE, 2013.

[59] A. Khalid, G. Cossu, R. Corsini, P. Choudhury, and E. Ciaramella, "1-Gb/s transmission over a phosphorescent white LED by using rate-adaptive discrete multitone modulation," *IEEE Photonics Journal*, vol. 4, no. 5, pp. 1465–1473, 2012.

[60] J. Grubor, S. Randel, K.-D. Langer, and J. W. Walewski, "Broadband information broadcasting using LED-based interior lighting," *Journal of Lightwave technology*, vol. 26, no. 24, pp. 3883–3892, 2008.

[61] M. Biagi, T. Borogovac, and T. D. Little, "Adaptive receiver for indoor visible light communications," *Journal of Lightwave Technology*, vol. 31, no. 23, pp. 3676–3686, 2013.

[62] N. Anous, T. Ramadan, M. Abdallah, K. Qaraqe, and D. Khalil, "Impact of blue filtering on effective modulation bandwidth and wide-angle operation in white LED-based VLC systems," *OSA Continuum*, vol. 1, no. 3, pp. 910–929, 2018.

[63] G. Egecan, K. Akande, P. A. Haighy, and W. Popoola, "Frequency response modelling of cool and warm white LEDs in VLC systems," in *Proceedings of the First Western Conference on Wireless Telecommunications Western Asia, Isfahan, Iran*, pp. 63–66, 2017.

[64] M. M. Mohammed, C. He, and J. Armstrong, "Performance analysis of ACO-OFDM and DCO-OFDM using bit and power loading in frequency selective optical wireless channels," in *2017 IEEE 85th Vehicular Technology Conference (VTC Spring)*, pp. 1–5, IEEE, 2017.

[65] H. Ma, L. Lampe, and S. Hranilovic, "Robust MMSE linear precoding for visible light communication broadcasting systems," in *2013 IEEE Globecom Workshops (GC Wkshps)*, pp. 1081–1086, IEEE, 2013.

[66] D. Tsonev, S. Videv, and H. Haas, "Unlocking spectral efficiency in intensity modulation and direct detection systems," *IEEE Journal on Selected Areas in Communications*, vol. 33, no. 9, pp. 1758–1770, 2015.

[67] S. Dimitrov and H. Haas, "Information rate of OFDM-based optical wireless communication systems with nonlinear distortion," *Journal of Lightwave Technology*, vol. 31, no. 6, pp. 918–929, 2012.

[68] B. Inan, S. J. Lee, S. Randel, I. Neokosmidis, A. M. Koonen, and J. W. Walewski, "Impact of LED nonlinearity on discrete multitone modulation," *Journal of Optical Communications and Networking*, vol. 1, no. 5, pp. 439–451, 2009.

[69] H. Elgala, R. Mesleh, and H. Haas, "Non-linearity effects and predistortion in optical OFDM wireless transmission using LEDs," *International Journal of Ultra Wideband Communications and Systems*, vol. 1, no. 2, pp. 143–150, 2009.

[70] S. Dimitrov and H. Haas, "Optimum signal shaping in OFDM-based optical wireless communication systems," in *2012 IEEE Vehicular Technology Conference (VTC Fall)*, pp. 1–5, IEEE, 2012.

[71] L. Chen, B. Krongold, and J. Evans, "Performance evaluation of optical OFDM systems with nonlinear clipping distortion," in *2009 IEEE International Conference on Communications*, pp. 1–5, IEEE, 2009.

[72] M. Zhang and Z. Zhang, "An optimum DC-biasing for DCO-OFDM system," *IEEE Communications Letters*, vol. 18, no. 8, pp. 1351–1354, 2014.

[73] A. Burton, Z. Ghassemlooy, S. Rajbhandari, and S.-K. Liaw, "Design and analysis of an angular-segmented full-mobility visible light communications receiver," *Transactions on Emerging Telecommunications Technologies*, vol. 25, no. 6, pp. 591–599, 2014.

[74] G. Stepniak, J. Siuzdak, and P. Zwierko, "Compensation of a VLC phosphorescent white LED nonlinearity by means of Volterra DFE," *IEEE Photonics Technology Letters*, vol. 25, no. 16, pp. 1597–1600, 2013.

[75] P. Deng, M. Kavehrad, and M. A. Kashani, "Nonlinear modulation characteristics of white LEDs in visible light communications," in *Optical Fiber Communication Conference*, pp. W2A–64, Optical Society of America, 2015.

[76] C. T. Geldard, J. Thompson, and W. O. Popoola, "Empirical study of the underwater turbulence effect on non-coherent light," *IEEE Photonics Technology Letters*, vol. 32, no. 20, pp. 1307–1310, 2020.

[77] N. Chi, *LED-based visible light Communications*. Springer, 2018.

[78] Thorlabs, *PDA10A(-EC) Si Amplified Fixed Gain Detector*, Sept. 2017.

[79] F. Xu, M.-A. Khalighi, and S. Bourennane, "Impact of different noise sources on the performance of PIN-and APD-based FSO receivers," in *Proceedings of the 11th International Conference on Telecommunications*, pp. 211–218, IEEE, 2011.

[80] L. Zeng, D. C. O'Brien, H. Le Minh, G. E. Faulkner, K. Lee, D. Jung, Y. Oh, and E. T. Won, "High data rate multiple input multiple output (MIMO) optical wireless communications using white LED lighting," *IEEE Journal on Selected Areas in Communications*, vol. 27, no. 9, pp. 1654–1662, 2009.

[81] C. Chen, M. Ijaz, D. Tsonev, and H. Haas, "Analysis of downlink transmission in DCO-OFDM-based optical attocell networks," in *2014 IEEE global communications conference*, pp. 2072–2077, IEEE, 2014.

[82] J. G. Proakis, *Digital communications*. McGraw-Hill Companies, Inc., New York, NY, 1998.

[83] S. H. Lee, K.-I. Ahn, and J. K. Kwon, "Multilevel transmission in dimmable visible light communication systems," *Journal of Lightwave Technology*, vol. 31, no. 20, pp. 3267–3276, 2013.

[84] M. S. Islim and H. Haas, "Modulation techniques for LiFi," *ZTE communications*, vol. 14, no. 2, pp. 29–40, 2019.

[85] S. Arnon, "The effect of clock jitter in visible light communication applications," *journal of Lightwave Technology*, vol. 30, no. 21, pp. 3434–3439, 2012.

[86] H.-J. Jang, J.-H. Choi, Z. Ghassemlooy, and C. G. Lee, "PWM-based PPM format for dimming control in visible light communication system," in *2012 8th International Symposium on Communication Systems, Networks & Digital Signal Processing (CSNDSP)*, pp. 1–5, IEEE, 2012.

[87] S. He, G. Ren, Z. Zhong, and Y. Zhao, "M-ary variable period modulation for indoor visible light communication system," *IEEE communications letters*, vol. 17, no. 7, pp. 1325–1328, 2013.

[88] H. Elgala, R. Mesleh, H. Haas, and B. Pricope, "OFDM visible light wireless communication based on white LEDs," in *2007 IEEE 65th Vehicular Technology Conference-VTC2007-Spring*, pp. 2185–2189, IEEE, 2007.

[89] O. González, R. Pérez-Jiménez, S. Rodriguez, J. Rabadán, and A. Ayala, "OFDM over indoor wireless optical channel," *IEE Proceedings-Optoelectronics*, vol. 152, no. 4, pp. 199–204, 2005.

[90] J. B. Carruthers and J. M. Kahn, "Multiple-subcarrier modulation for nondirected wireless infrared communication," *IEEE journal on selected areas in communications*, vol. 14, no. 3, pp. 538–546, 1996.

[91] R. Mesleh, H. Elgala, and H. Haas, "On the performance of different OFDM based optical wireless communication systems," *Journal of Optical Communications and Networking*, vol. 3, no. 8, pp. 620–628, 2011.

[92] J. Armstrong and A. J. Lowery, "Power efficient optical OFDM," *Electronics letters*, vol. 42, no. 6, p. 1, 2006.

[93] S. C. J. Lee, S. Randel, F. Breyer, and A. M. Koonen, "PAM-DMT for intensity-modulated and direct-detection optical communication systems," *IEEE Photonics Technology Letters*, vol. 21, no. 23, pp. 1749–1751, 2009.

[94] N. Fernando, Y. Hong, and E. Viterbo, "Flip-OFDM for unipolar communication systems," *IEEE Transactions on Communications*, vol. 60, no. 12, pp. 3726–3733, 2012.

[95] D. Tsonev, S. Sinanovic, and H. Haas, "Novel unipolar orthogonal frequency division multiplexing (U-OFDM) for optical wireless," in *2012 IEEE 75th Vehicular Technology Conference (VTC Spring)*, pp. 1–5, IEEE, 2012.

[96] J. Armstrong, "OFDM for optical communications," *Journal of lightwave technology*, vol. 27, no. 3, pp. 189–204, 2009.

[97] C. E. Shannon, "Communication in the presence of noise," *Proceedings of the IRE*, vol. 37, no. 1, pp. 10–21, 1949.

[98] Z. Qu and I. B. Djordjevic, "On the probabilistic shaping and geometric shaping in optical communication systems," *IEEE Access*, vol. 7, pp. 21454–21464, 2019.

[99] F.-W. Sun and H. C. Van Tilborg, "Approaching capacity by equiprobable signaling on the Gaussian channel," *IEEE transactions on information theory*, vol. 39, no. 5, pp. 1714–1716, 1993.

[100] Z. Qu and I. B. Djordjevic, "Geometrically shaped 16QAM outperforming probabilistically shaped 16QAM," in *2017 European Conference on Optical Communication (ECOC)*, pp. 1–3, IEEE, 2017.

[101] J. J. Boutros, U. Erez, J. Van Wonterghem, G. I. Shamir, and G. Zémor, "Geometric shaping: low-density coding of Gaussian-like constellations," in *2018 IEEE Information Theory Workshop (ITW)*, pp. 1–5, IEEE, 2018.

[102] B. Chen, C. Okonkwo, D. Lavery, and A. Alvarado, "Geometrically-shaped 64-point constellations via achievable information rates," in *2018 20th International Conference on Transparent Optical Networks (ICTON)*, pp. 1–4, IEEE, 2018.

[103] T. Fehenberger, D. Lavery, R. Maher, A. Alvarado, P. Bayvel, and N. Hanik, "Sensitivity gains by mismatched probabilistic shaping for optical communication systems," *IEEE Photonics Technology Letters*, vol. 28, no. 7, pp. 786–789, 2016.

[104] J. Cho and P. J. Winzer, "Probabilistic constellation shaping for optical fiber communications," *Journal of Lightwave Technology*, vol. 37, no. 6, pp. 1590–1607, 2019.

[105] A. R. Calderbank and L. H. Ozarow, "Nonequiprobable signaling on the Gaussian channel," *IEEE Transactions on Information Theory*, vol. 36, no. 4, pp. 726–740, 1990.

[106] F. R. Kschischang and S. Pasupathy, "Optimal nonuniform signaling for Gaussian channels," *IEEE Transactions on Information Theory*, vol. 39, no. 3, pp. 913–929, 1993.

[107] R. Laroia, N. Farvardin, and S. A. Tretter, "On optimal shaping of multidimensional constellations," *IEEE Transactions on Information Theory*, vol. 40, no. 4, pp. 1044–1056, 1994.

[108] T. A. Eriksson, M. Chagnon, F. Buchali, K. Schuh, S. ten Brink, and L. Schmalen, "56 Gbaud probabilistically shaped PAM8 for data center interconnects," in *2017 European Conference on Optical Communication (ECOC)*, pp. 1–3, IEEE, 2017.

[109] D. N. Anwar and A. Srivastava, "Design and Analysis of Probabilistic Shaping in Color Shift Keying Modulation Schemes," *IEEE Systems Journal*, vol. 15, no. 1, pp. 1433–1444, 2021.

[110] U. Wachsmann, R. F. Fischer, and J. B. Huber, "Multilevel codes: Theoretical concepts and practical design rules," *IEEE Transactions on Information Theory*, vol. 45, no. 5, pp. 1361–1391, 1999.

[111] T. Fehenberger, A. Alvarado, G. Böcherer, and N. Hanik, "On probabilistic shaping of quadrature amplitude modulation for the nonlinear fiber channel," *Journal of Lightwave Technology*, vol. 34, no. 21, pp. 5063–5073, 2016.

[112] G. Böcherer, F. Steiner, and P. Schulte, "Bandwidth efficient and rate-matched low-density parity-check coded modulation," *IEEE Transactions on communications*, vol. 63, no. 12, pp. 4651–4665, 2015.

[113] J. Ma, J. He, M. Chen, and K. Wu, "Performance enhancement of probabilistically shaped OFDM enabled by precoding technique in an IM-DD system," *Journal of Lightwave Technology*, vol. 37, no. 24, pp. 6063–6071, 2019.

[114] D. Che, J. Cho, and X. Chen, "Does probabilistic constellation shaping benefit IM-DD systems without optical amplifiers?," *Journal of Lightwave Technology*, vol. 39, no. 15, pp. 4997–5007, 2021.

[115] P. Schulte and G. Böcherer, "Constant composition distribution matching," *IEEE Transactions on Information Theory*, vol. 62, no. 1, pp. 430–434, 2015.

[116] F. Buchali, G. Böcherer, W. Idler, L. Schmalen, P. Schulte, and F. Steiner, "Experimental demonstration of capacity increase and rate-adaptation by probabilistically shaped 64-QAM," in *2015 European Conference on Optical Communication (ECOC)*, pp. 1–3, IEEE, 2015.

[117] R. F. Fischer, *Precoding and signal shaping for digital transmission*. John Wiley & Sons, 2005.

[118] G. Forney and L.-F. Wei, "Multidimensional constellations. I. Introduction, figures of merit, and generalized cross constellations," *IEEE Journal on Selected Areas in Communications*, vol. 7, no. 6, pp. 877–892, 1989.

[119] C. Xie, Z. Chen, S. Fu, W. Liu, Z. He, L. Deng, M. Tang, and D. Liu, "Achievable information rate enhancement of visible light communication using probabilistically shaped OFDM modulation," *Optics express*, vol. 26, no. 1, pp. 367–375, 2018.

[120] X. Hong, C. Fei, G. Zhang, and S. He, "Probabilistically shaped 256-QAM-OFDM transmission in underwater wireless optical communication system," in *2019 Optical Fiber Communications Conference and Exhibition (OFC)*, pp. 1–3, IEEE, 2019.

[121] S. Xing, F. Hu, G. Li, J. Zhang, N. Chi, Z. He, and S. Yu, "Demonstration of flexible access in a rate-adaptive visible light communication system with constellation probabilistic shaping," *Optics Express*, vol. 29, no. 21, pp. 34441–34451, 2021.

[122] M. P. Yankov, D. Zibar, K. J. Larsen, L. P. Christensen, and S. Forchhammer, "Constellation shaping for fiber-optic channels with QAM and high spectral efficiency," *IEEE Photonics Technology Letters*, vol. 26, no. 23, pp. 2407–2410, 2014.

[123] M. P. Yankov, F. Da Ros, E. P. da Silva, S. Forchhammer, K. J. Larsen, L. K. Oxenløwe, M. Galili, and D. Zibar, "Constellation shaping for WDM systems using 256QAM/1024QAM with probabilistic optimization," *Journal of Lightwave Technology*, vol. 34, no. 22, pp. 5146–5156, 2016.

[124] G. Li, F. Hu, P. Zou, C. Wang, G.-R. Lin, and N. Chi, "Advanced Modulation Format of Probabilistic Shaping Bit Loading for 450-nm GaN Laser Diode based Visible Light Communication," *Sensors*, vol. 20, no. 21, p. 6143, 2020.

[125] X. Hong, C. Fei, G. Zhang, J. Du, and S. He, "Discrete multitone transmission for underwater optical wireless communication system using probabilistic constellation shaping to approach channel capacity limit," *Optics Letters*, vol. 44, no. 3, pp. 558–561, 2019.

[126] X. Deng, S. Mardanikorani, Y. Wu, K. Arulandu, B. Chen, A. M. Khalid, and J.-P. M. Linnartz, "Mitigating LED nonlinearity to enhance visible light communications," *IEEE Transactions on Communications*, vol. 66, no. 11, pp. 5593–5607, 2018.

[127] H. Lu, J. Jin, and J. Wang, "Alleviation of LED nonlinearity impact in visible light communication using companding and predistortion," *IET Communications*, vol. 13, no. 7, pp. 818–821, 2019.

[128] M. Laakso, A. A. Dowhuszko, and R. Wichman, "Predistortion of OFDM signals for VLC systems using phosphor-converted LEDs," in *2022 IEEE 23rd International Workshop on Signal Processing Advances in Wireless Communication (SPAWC)*, pp. 1–5, IEEE, 2022.

[129] X. Ling, X. Zhang, J. Sun, P. Ge, J. Wang, C. Zhao, and X. Gao, "When Hammerstein meets Wiener: Nonlinearity Modeling for End-to-End Visible Light Communication Links," *IEEE Transactions on Communications*, 2022.

[130] R. Bian, I. Tavakkolnia, and H. Haas, "15.73 Gb/s visible light communication with off-the-shelf LEDs," *Journal of Lightwave Technology*, vol. 37, no. 10, pp. 2418–2424, 2019.

[131] H. Chun, S. Rajbhandari, G. Faulkner, D. Tsonev, E. Xie, J. J. D. McKendry, E. Gu, M. D. Dawson, D. C. O'Brien, and H. Haas, "LED based wavelength division multiplexed 10 Gb/s visible light communications," *Journal of lightwave technology*, vol. 34, no. 13, pp. 3047–3052, 2016.

[132] F. Wu, C.-T. Lin, C. Wei, C. Chen, Z. Chen, H. Huang, and S. Chi, "Performance comparison of OFDM signal and CAP signal over high capacity RGB-LED-based WDM visible light communication," *IEEE Photonics Journal*, vol. 5, no. 4, pp. 7901507–7901507, 2013.

[133] A. Kafizov, A. Elzanaty, and M.-S. Alouini, "Probabilistic Shaping Based Spatial Modulation for Spectral-Efficient VLC," *IEEE Transactions on Wireless Communications*, 2022.

[134] IEEE, "IEEE Standard for Low-Rate Wireless Networks," *IEEE Std 802.15.4-2020 (Revision of IEEE Std 802.15.4-2015)*, pp. 1–800, 2020.

[135] M. A. Matin and M. Islam, "Overview of wireless sensor network," *Wireless sensor networks-technology and protocols*, vol. 1, no. 3, 2012.

[136] A. Makvandi, Y. S. Kavian, and E. Namjoo, "VLCIoT: design and implementation of a visible light communication system for indoor Internet of Things applications," *Applied Optics*, vol. 60, no. 36, pp. 11094–11103, 2021.

[137] A. Pradana, N. Ahmadi, T. Adiono, W. A. Cahyadi, and Y.-H. Chung, "VLC physical layer design based on pulse position modulation (PPM) for stable illumination," in *2015 international symposium on intelligent signal processing and communication systems (ISPACS)*, pp. 368–373, IEEE, 2015.

[138] D.-S. Shiu and J. M. Kahn, "Differential pulse-position modulation for power-efficient optical communication," *IEEE transactions on communications*, vol. 47, no. 8, pp. 1201–1210, 1999.

[139] W. O. Popoola, E. Poves, and H. Haas, "Spatial pulse position modulation for optical communications," *Journal of Lightwave Technology*, vol. 30, no. 18, pp. 2948–2954, 2012.

[140] H. Park and J. R. Barry, "Trellis-coded multiple-pulse-position modulation for wireless infrared communications," *IEEE transactions on communications*, vol. 52, no. 4, pp. 643–651, 2004.

[141] M. Jani, P. Garg, and A. Gupta, "Performance analysis of a mixed cooperative PLC–VLC system for indoor communication systems," *IEEE Systems Journal*, vol. 14, no. 1, pp. 469–476, 2019.

[142] Y. Roth, J.-B. Doré, L. Ros, and V. Berg, "Turbo-FSK, a physical layer for low-power wide-area networks: Analysis and optimization," *Comptes Rendus Physique*, vol. 18, no. 2, pp. 178–188, 2017.

[143] A. W. Azim, A. Rullier, Y. Le Guennec, L. Ros, and G. Maury, "Energy Efficient M-ary Frequency-Shift Keying-Based Modulation Techniques for Visible Light Communication," *IEEE Transactions on Cognitive Communications and Networking*, vol. 5, no. 4, pp. 1244–1256, 2019.

[144] G. M. Yamga, A. Ndjiongue, and K. Ouahada, "Low complexity clipped frequency shift keying (FSK) for visible light communications," in *2018 IEEE 7th International Conference on Adaptive Science & Technology (ICAST)*, pp. 1–6, IEEE, 2018.

[145] L. Vangelista, "Frequency shift chirp modulation: The LoRa modulation," *IEEE Signal Processing Letters*, vol. 24, no. 12, pp. 1818–1821, 2017.

[146] A. Springer, W. Gugler, M. Huemer, L. Reindl, C. Ruppel, and R. Weigel, "Spread spectrum communications using chirp signals," in *IEEE/AFCEA EUROCOMM 2000. Information Systems for Enhanced Public Safety and Security (Cat. No. 00EX405)*, pp. 166–170, IEEE, 2000.

[147] T. Elshabrawy and J. Robert, "Closed-form approximation of LoRa modulation BER performance," *IEEE Communications Letters*, vol. 22, no. 9, pp. 1778–1781, 2018.

[148] T. T. Nguyen, H. H. Nguyen, R. Barton, and P. Grossetete, "Efficient design of chirp spread spectrum modulation for low-power wide-area networks," *IEEE Internet of Things Journal*, vol. 6, no. 6, pp. 9503–9515, 2019.

[149] I. Demirkol, D. Camps-Mur, J. Paradells, M. Combalia, W. Popoola, and H. Haas, "Powering the Internet of Things through light communication," *IEEE Communications Magazine*, vol. 57, no. 6, pp. 107–113, 2019.

[150] W. O. Popoola, E. Poves, and H. Haas, "Error performance of generalised space shift keying for indoor visible light communications," *IEEE Transactions on Communications*, vol. 61, no. 5, pp. 1968–1976, 2013.

[151] K. Ying, Z. Yu, R. J. Baxley, H. Qian, G.-K. Chang, and G. T. Zhou, "Nonlinear distortion mitigation in visible light communications," *IEEE Wireless Communications*, vol. 22, no. 2, pp. 36–45, 2015.

[152] Y. Hei, Y. Kou, G. Shi, W. Li, and H. Gu, "Energy-Spectral Efficiency Tradeoff in DCO-OFDM Visible Light Communication System," *IEEE Transactions on Vehicular Technology*, vol. 68, no. 10, pp. 9872–9882, 2019.

[153] Vishay, *Ultrabright 0402 ChipLED*, Feb. 2017.

[154] G. D. Forney and G. Ungerboeck, "Modulation and coding for linear Gaussian channels," *IEEE Transactions on Information Theory*, vol. 44, no. 6, pp. 2384–2415, 1998.

[155] J. G. Proakis and M. Salehi, *Digital communications*, vol. 5. McGraw-hill New York, 2008.

[156] J. G. Proakis and M. Salehi, *Digital communications*, vol. 4. McGraw-hill New York, 2001.

[157] C. M. Grinstead and J. L. Snell, *Introduction to probability*. American Mathematical Soc., 1997.

[158] M. K. Simon and M.-S. Alouini, *Digital communication over fading channels*, vol. 95. John Wiley & Sons, 2005.

[159] M. Safari and M. Uysal, "Relay-assisted free-space optical communication," *IEEE Transactions on Wireless Communications*, vol. 7, no. 12, pp. 5441–5449, 2008.

[160] M. Abramowitz, I. A. Stegun, and R. H. Romer, "Handbook of mathematical functions with formulas, graphs, and mathematical tables," 1988.

[161] T. M. Cover and J. A. Thomas, *Entropy, Relative Entropy, and Mutual Information*. John Wiley & Sons, Ltd, 2005.

[162] G. Böcherer, "Achievable rates for shaped bit-metric decoding," *arXiv preprint arXiv:1410.8075*, 2014.

[163] J. Cho, L. Schmalen, and P. J. Winzer, "Normalized generalized mutual information as a forward error correction threshold for probabilistically shaped QAM," in *2017 European Conference on Optical Communication (ECOC)*, pp. 1–3, IEEE, 2017.

[164] A. Alvarado, E. Agrell, D. Lavery, R. Maher, and P. Bayvel, "Replacing the soft-decision FEC limit paradigm in the design of optical communication systems," *Journal of Lightwave Technology*, vol. 33, no. 20, pp. 4338–4352, 2015.

[165] H. E. Levin, "A complete and optimal data allocation method for practical discrete multitone systems," in *GLOBECOM'01. IEEE Global Telecommunications Conference (Cat. No. 01CH37270)*, vol. 1, pp. 369–374, IEEE, 2001.

[166] F. Xiong, *Digital modulation techniques*. Artech House Publishers, 2nd ed. ed., 2000.

[167] D. Che and W. Shieh, "Squeezing out the last few bits from band-limited channels with entropy loading," *Optics express*, vol. 27, no. 7, pp. 9321–9329, 2019.

[168] D. Tsonev, S. Sinanovic, and H. Haas, "Complete modeling of nonlinear distortion in OFDM-based optical wireless communication," *Journal of Lightwave Technology*, vol. 31, no. 18, pp. 3064–3076, 2013.

[169] R. A. Shafik, M. S. Rahman, and A. R. Islam, "On the extended relationships among EVM, BER and SNR as performance metrics," in *2006 International Conference on Electrical and Computer Engineering*, pp. 408–411, IEEE, 2006.

[170] J. Lian, M. Noshad, and M. Brandt-Pearce, "Comparison of optical OFDM and M-PAM for LED-based communication systems," *IEEE Communications Letters*, vol. 23, no. 3, pp. 430–433, 2019.

[171] J. Ma, J. He, J. Shi, Z. Zhou, and R. Deng, "Nonlinear compensation based on k-means clustering algorithm for Nyquist PAM-4 VLC system," *IEEE Photonics Technology Letters*, vol. 31, no. 12, pp. 935–938, 2019.

[172] E. Guler, C. Geldard, A. Baldwin, and W. Popoola, "A Demonstration of Frequency-Shift Keying in Underwater Optical Wireless Communications," in *CLEO: QELS_Fundamental Science*, pp. JW3B–104, Optica Publishing Group, 2022.

[173] O. Afisiadis, M. Cotting, A. Burg, and A. Balatsoukas-Stimming, "On the error rate of the LoRa modulation with interference," *IEEE Transactions on Wireless Communications*, vol. 19, no. 2, pp. 1292–1304, 2019.